Engineering Journal

American Institute of Steel Construction

Third Quarter 2008 ume 45, No. 3

www.aisc.org

ENGINEERING JOURNAL

AMERICAN INSTITUTE OF STEEL CONSTRUCTION

Dedicated to the development and improvement of steel construction, through the interchange of ideas, experiences and data.

ENGINEERING JOURNAL (ISSN 0013-8029) is published quarterly. Subscriptions: Members: one subscription, $20 per year, included in dues; Additional Member Subscriptions: $15 per year. Non-Members U.S., Canada, and Mexico: $40 per year, $110 for three years, single copy $15. International Members and Non-Members: $90 per year; $250 for three years; single copy $25. Published by the American Institute of Steel Construction at One East Wacker Drive, Suite 700, Chicago, IL 60601.

Periodicals postage paid at Chicago, IL and additional mailing offices. **Postmaster:** Send address changes to ENGINEERING JOURNAL in care of the American Institute of Steel Construction, One East Wacker Drive, Suite 700, Chicago, IL 60601.

A Comparison of Frame Stability Analysis Methods in ANSI/AISC 360-05

CHARLES J. CARTER and LOUIS F. GESCHWINDNER

ANSI/AISC 360-05 *Specification for Structural Steel Buildings* (AISC, 2005a), hereafter referred to as the AISC *Specification*, includes three prescriptive approaches for stability analysis and design. Table 2-1 in the 13th Edition AISC *Steel Construction Manual* (AISC, 2005b), hereafter referred to as the AISC *Manual*, provides a comparison of the methods and design options associated with each. A fourth approach, referred to as the Simplified Method, is also presented in the AISC *Manual* (see page 2-12) and on the AISC *Basic Design Values* cards. These four methods are illustrated in this paper in order to give the reader a general understanding of the differences between them:

1. The Second-Order Analysis Method (Section C2.2a)
2. The First-Order Analysis Method (Section C2.2b)
3. The Direct Analysis Method (Appendix 7)
4. The Simplified Method (Manual page 2-12; AISC *Basic Design Values* cards)

Two simple unbraced frames are used in this paper. The one-bay frame shown in Figure 1 has a rigid roof element spanning between a flagpole column (Column A) and leaning column (Column B). Drift is not limited for this frame, which results in a higher ratio of second-order drift to first-order drift, and allows illustration of the detailed requirements in each method for the calculation of *K*-factors, notional loads, and required and available strengths. The three-bay frame shown in Figure 2 has rigid roof elements spanning between two flagpole columns (Columns D and E) and two leaning columns (Columns C and F). This frame is used with a drift limit of *L*/400 to illustrate the simplifying effect a drift limit can have on the analysis requirements in each method.

Although these example frames are not realistic frames, the results obtained are representative of the impact of second-order elastic and inelastic effects on strength requirements in real frames, particularly when the number of moment connections is reduced. The loads shown in Figures 1 and 2 are from the controlling load and resistance factor design (LRFD) load combination and the corresponding designs are performed using LRFD. The process is essentially identical for allowable strength design (ASD), where ASD load combinations are used with $\alpha = 1.6$ as a multiplier, when required in each method, to account for the second-order effects at the ultimate load level.

When it is required to include second-order effects, the B_1-B_2 amplification is used with a first-order analysis throughout this paper. A direct second-order analysis is straightforward and could have been used instead of the B_1-B_2 amplification.

THE ONE-BAY FRAME

A trial shape is selected using a first-order analysis without consideration of drift limits or second-order effects. Thereafter, that trial shape is used as the basis for comparison of the four methods discussed earlier.

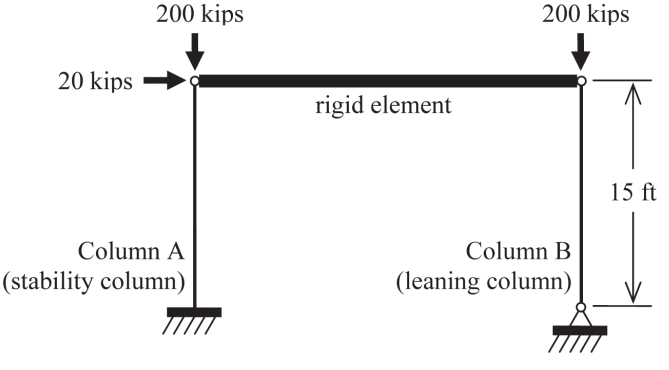

Fig. 1. One-bay unbraced frame used in examples.

Charles J. Carter is vice president and chief structural engineer, American Institute of Steel Construction, Chicago, IL.

Louis F. Geschwindner is vice president of special projects, American Institute of Steel Construction, and professor emeritus of architectural engineering at Pennsylvania State University, University Park, PA.

Selection of Trial Shape Based Upon Strength Consideration Only

Based upon the loading shown in Figure 1, the first-order axial force, strong-axis moment, and design parameters for Column A are:

P_u = 200 kips M_{ux} = (20 kips) (15 ft)
K_x = 2.0 = 300 kip-ft
K_y = 1.0 C_b = 1.67
$L_x = L_y$ = 15 ft L_b = 15 ft

Note that K_x = 2.0, the theoretical value for a column with a fixed base and top that is free to rotate and translate, is used rather than the value of 2.1 recommended for design in the AISC *Specification* Commentary Table C-C2.2. The value of 2.0 is used because it is consistent with the formulation of the lateral stiffness calculation below. Note also that the impact of the leaning column on K_x is ignored in selecting the trial size, although it will be considered in subsequent sections when K_x cannot be taken equal to 1 for Column A. Out of the plane of the frame, K_y is taken as 1.0.

A simple rule of thumb for trial beam-column selection is to use an equivalent axial force equal to P_u plus 24/d times M_u, where d is the nominal depth of the column (Geschwindner, Disque and Bjorhovde, 1994). Using d = 14 in. for a W14, the equivalent axial force is 714 kips and an ASTM A992 W14×90 is selected as the trial shape.

The lateral stiffness of the frame depends on Column A only and is:

$$k = 3EI/L^3$$
$$= 3(29{,}000 \text{ ksi})(999 \text{ in.}^4)/(15 \text{ ft} \times 12 \text{ in./ft})^3$$
$$= 14.9 \text{ kips/in.}$$

The corresponding first-order drift of the frame is:

$$\Delta_{1st} = (20 \text{ kips})/(14.9 \text{ kips/in.})$$
$$= 1.34 \text{ in.}$$

Note that this is a very flexible frame with Δ_{1st}/L = 1.34/(15 ft × 12 in./ft) = 1/134.

Design by Second-Order Analysis (Section C2.2a)

Design by second-order analysis is essentially the traditional effective length method with an additional requirement for a minimum lateral load. It is permitted when the ratio of second-order drift, Δ_{2nd}, to first-order drift, Δ_{1st}, is equal to or less than 1.5, and requires the use of:

1. A direct second-order analysis or a first-order analysis with B_1-B_2 amplification.
2. The nominal frame geometry with a minimum lateral load (a "notional load") $N_i = 0.002Y_i$, where Y_i is the total gravity load on level i from LRFD load combinations (or 1.6 times ASD load combinations). This notional load is specified to capture the effects of initial out-of-plumbness up to the AISC *Code of Standard Practice* maximum value of 1:500. In this method, N_i is not applied when the actual lateral load is larger than the calculated notional load.
3. The nominal stiffnesses EA and EI.
4. LRFD load combinations, or ASD load combinations multiplied by 1.6. This multiplier on ASD load combinations ensures that the drift level is consistent for LRFD and ASD when determining second-order effects. The forces and moments obtained in this analysis are then divided by 1.6 for ASD member design.

When the ratio of second-order drift to first-order drift, which is given by B_2, is equal to or less than 1.1, K = 1.0 can be used in the design of moment frames. Otherwise, for moment frames, K is determined from a sidesway buckling analysis. Section C2.2a(4) indicates that for braced frames, K = 1.0.

For the example frame given in Figure 1, the minimum lateral load based upon the total gravity load, Y_i, is:

$$Y_i = 200 \text{ kips} + 200 \text{ kips}$$
$$= 400 \text{ kips}$$

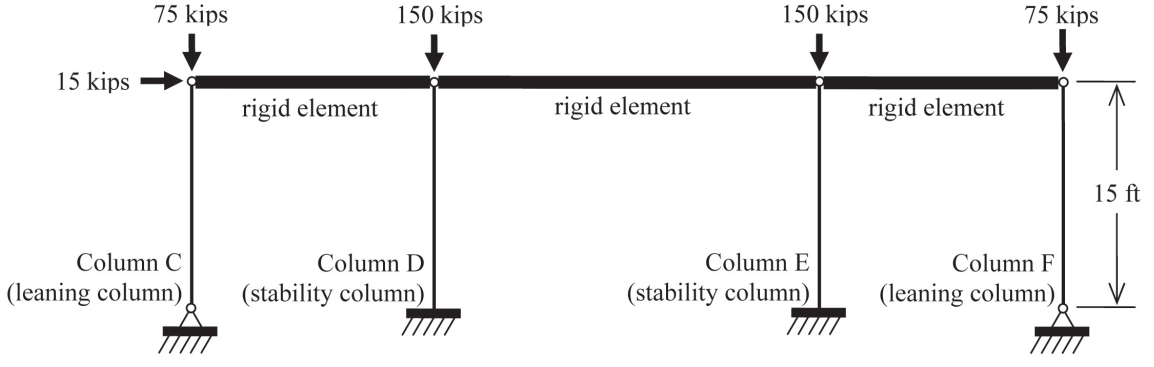

Fig. 2. Three-bay unbraced frame used in examples.

$$N_i = 0.002\,Y_i$$
$$= 0.002\,(400 \text{ kips})$$
$$= 0.8 \text{ kips}$$

Because this notional load is less than the actual lateral load, it need not be applied. For a load combination that did not include a lateral load, the notional load would need to be included in the analysis.

For Column A, using first-order analysis and B_1-B_2 amplification:

$P_{nt} = 200$ kips, $P_{lt} = 0$ kips
$M_{nt} = 0$ kip-ft, $M_{lt} = 300$ kip-ft

For P-δ amplification, since there are no moments associated with the no-translation case, there is no need to calculate B_1. For P-Δ amplification, the first-order drift ratio is determined from the calculated drift of 1.34 in. Thus,

$$\Delta_{1st}/L = (1.34 \text{ in.})/(15 \text{ ft} \times 12 \text{ in./ft})$$
$$= 0.00744$$

For moment frames, $R_m = 0.85$ and from Equation C2-6b with $\Delta_H = \Delta_{1st}$ and $\Sigma H = 20$ kips,

$$\Sigma P_{e2} = R_m \Sigma H/(\Delta_{1st}/L)$$
$$= 0.85\,(20 \text{ kips})/(0.00744)$$
$$= 2{,}280 \text{ kips}$$

For design by LRFD, $\alpha = 1.0$ and ΣP_{nt} is the sum of the gravity loads. Thus,

$$\alpha\Sigma P_{nt}/\Sigma P_{e2} = 1.0\,(200 \text{ kips} + 200 \text{ kips})/2{,}280 \text{ kips}$$
$$= 0.175$$

From Equation C2-3, the amplification is:

$$B_2 = \frac{1}{1 - \dfrac{\alpha \Sigma P_{nt}}{\Sigma P_{e2}}} \geq 1$$
$$= \frac{1}{1 - 0.175} \geq 1$$
$$= 1.21 \geq 1.0$$
$$= 1.21$$

Because $B_2 = 1.21$, the second-order drift is less than 1.5 times the first-order drift. Thus, the use of this method is permitted. Because $B_2 > 1.1$, K cannot be taken as 1.0 for column design in the moment frame with this method. Thus, K must be calculated, including the leaning-column effect. Several approaches are available in the AISC *Specification* Commentary to include this effect. A simple approach that uses the ratio of the load on the leaning columns to the load on the stabilizing columns had been provided in previous Commentaries and is used here (Lim and McNamara, 1972):

$$\Sigma P_{leaning}/\Sigma P_{stability} = (200 \text{ kips})/(200 \text{ kips})$$
$$= 1$$

$$K_x^* = K_x(1 + \Sigma P_{leaning} / \Sigma P_{stability})^{1/2}$$
$$= 2.0(1 + 1)^{1/2}$$
$$= 2.83$$

The amplified axial force (Equation C2-1b) and associated design parameters for this method are:

$$P_r = P_{nt} + B_2 P_{lt}$$
$$= 200 \text{ kips} + 1.21(0 \text{ kips})$$
$$= 200 \text{ kips}$$

$K_x^* = 2.83$, $K_y = 1.0$

$L_x = L_y = 15$ ft

The amplified moment (Equation C2-1a) and associated design parameters for this method are:

$$M_{rx} = B_1 M_{nt} + B_2 M_{lt}$$
$$= (0 \text{ kip-ft}) + 1.21\,(300 \text{ kip-ft})$$
$$= 363 \text{ kip-ft}$$

$C_b = 1.67$

$L_b = 15$ ft

Based upon these design parameters, the axial and strong-axis available flexural strengths of the ASTM A992 W14×90 are:

$$P_c = \phi_c P_n$$
$$= 721 \text{ kips}$$

$$M_{cx} = \phi_b M_{nx}$$
$$= 573 \text{ kip-ft}$$

To determine which interaction equation is applicable, the ratio of the required axial compressive strength to available axial compressive strength must be determined.

$$\frac{P_r}{P_c} = \frac{200 \text{ kips}}{721 \text{ kips}}$$
$$= 0.277$$

Thus, because $P_r/P_c \geq 0.2$, Equation H1-1a is applicable.

$$\frac{P_r}{P_c} + \frac{8}{9}\left(\frac{M_{rx}}{M_{cx}}\right) = 0.277 + \frac{8}{9}\left(\frac{363 \text{ kip-ft}}{573 \text{ kip-ft}}\right)$$
$$= 0.840$$

The W14×90 is adequate because $0.840 \leq 1.0$.

Design by First-Order Analysis (Section C2.2b)

The first-order analysis method is permitted when:

1. The ratio of second-order drift, Δ_{2nd}, to first-order drift, Δ_{1st}, is equal to or less than 1.5.

2. The column axial force $\alpha P_r \leq 0.5 P_y$, where $\alpha = 1.0$ for LRFD, 1.6 for ASD.

This method requires the use of:

1. A first-order analysis.
2. The nominal frame geometry with an additional lateral load $N_i = 2.1(\Delta/L)Y_i \geq 0.0042Y_i$, applied in all load cases.
3. The nominal stiffnesses EA and EI.
4. B_1 as a multiplier on the total moment in beam-columns.
5. LRFD load combinations, or ASD load combinations multiplied by 1.6. This multiplier on ASD load combinations ensures that the drift level is consistent for LRFD and ASD when determining the notional loads. The forces and moments obtained in this analysis are then divided by 1.6 for ASD member design.

For all frames designed with this method, $K = 1.0$.

For the example frame given in Figure 1, the additional lateral load is based on the first-order drift ratio, Δ/L, and the total gravity load, Y_i. Thus, with $\Delta = \Delta_{1st}$,

$$\Delta_{1st}/L = (1.34 \text{ in.})/(15 \text{ ft} \times 12 \text{ in./ft}) = 0.00744$$

$$Y_i = 200 \text{ kips} + 200 \text{ kips} = 400 \text{ kips}$$

$$N_i = 2.1(\Delta_{1st}/L)Y_i \geq 0.0042Y_i$$
$$= 2.1(0.00744)(400 \text{ kips}) \geq 0.0042(400 \text{ kips})$$
$$= 6.25 \text{ kips} \geq 1.68 \text{ kips}$$
$$= 6.25 \text{ kips}$$

It was previously determined in the illustration of design by second-order analysis example that the second-order drift is less than 1.5 times the first-order drift. Additionally,

$$\alpha P_r = 1.0(200 \text{ kips}) = 200 \text{ kips}$$

And for a W14×90,

$$0.5P_y = 0.5F_yA_g = 0.5(50 \text{ ksi})(26.5 \text{ in.}^2) = 663 \text{ kips}$$

Because $\Delta_{2nd} < 1.5\Delta_{1st}$ and $\alpha P_r < 0.5P_y$, the use of this method is permitted.

The loading for this method is the same as that shown in Figure 1, except for the addition of a notional load of 6.25 kips coincident with the lateral load of 20 kips shown, resulting in a column moment, M_u, of 394 kip-ft.

This moment must be amplified by B_1 as determined from Equation C2-2. The Euler buckling load is calculated with $K_1 = 1.0$. Thus,

$$P_{e1} = \pi^2EI/(K_1L)^2$$
$$= \pi^2(29{,}000 \text{ ksi})(999 \text{ in.}^4)/(1.0 \times 15 \text{ ft} \times 12 \text{ in./ft})^2$$
$$= 8{,}830 \text{ kips}$$

The moment on one end of the column is zero, so the moment gradient term is:

$$C_m = 0.6 - 0.4(M_1/M_2)$$
$$= 0.6 - 0.4(0/394 \text{ kip-ft})$$
$$= 0.6$$

From Equation C2-2,

$$\alpha P_r/P_{e1} = 1.0(200 \text{ kips})/(8{,}830 \text{ kips}) = 0.0227$$

$$B_1 = \frac{C_m}{1 - \frac{\alpha P_r}{P_{e1}}} \geq 1$$

$$= \frac{0.6}{1 - 0.0227} \geq 1.0$$
$$= 0.614 \geq 1.0$$
$$= 1.0$$

The axial force and associated design parameters for this method are:

$$P_r = 200 \text{ kips}$$
$$K_x = K_y = 1.0$$
$$L_x = L_y = 15 \text{ ft}$$

The amplified moment and associated design parameters for this method are:

$$M_{rx} = B_1M_u = 1.0 \text{ (394 kip-ft)} = 394 \text{ kip-ft}$$

$$C_b = 1.67$$

$$L_b = 15 \text{ ft}$$

Based on these design parameters, the axial and strong-axis available flexural strengths of the ASTM A992 W14×90 are:

$$P_c = \phi_cP_n = 1{,}000 \text{ kips}$$
$$M_{cx} = \phi_bM_{nx} = 573 \text{ kip-ft}$$

To determine which interaction equation is applicable, the ratio of the required axial compressive strength to available axial compressive strength must be determined.

$$\frac{P_r}{P_c} = \frac{200 \text{ kips}}{1{,}000 \text{ kips}} = 0.200$$

Thus, because $P_r/P_c \geq 0.2$, Equation H1-1a is applicable.

$$\frac{P_r}{P_c}+\frac{8}{9}\left(\frac{M_{rx}}{M_{cx}}\right)=0.200+\frac{8}{9}\left(\frac{394 \text{ kip-ft}}{573 \text{ kip-ft}}\right)$$
$$=0.811$$

The W14×90 is adequate since $0.811 \leq 1.0$.

Design by Direct Analysis (Appendix 7)

The Direct Analysis Method is permitted for any ratio of second-order drift, Δ_{2nd}, to first-order drift, Δ_{1st}, and required when this ratio exceeds 1.5. It requires the use of:

1. A direct second-order analysis or a first-order analysis with B_1-B_2 amplification.

2. The nominal frame geometry with an additional lateral load of $N_i = 0.002Y_i$, where Y_i is the total gravity load on level i from LRFD load combinations, or 1.6 times ASD load combinations.

3. The reduced stiffnesses EA^* and EI^* (including in B_1-B_2 amplification, if used).

4. LRFD load combinations, or ASD load combinations multiplied by 1.6. This multiplier ensures that the drift level is consistent for LRFD and ASD when determining second-order effects. The forces and moments obtained in this analysis are then divided by 1.6 for ASD member design.

The following exceptions apply as alternatives in item 2:

a. If the out-of-plumb geometry of the structures is used, the notional loads can be omitted.

b. When the ratio of second-order drift to first-order drift is equal to or less than 1.5, the notional load can be applied as a minimum lateral load, not an additional lateral load. Note that the unreduced stiffnesses, EA and EI, are used in this comparison.

c. When the actual out-of-plumbness is known, it is permitted to adjust the notional loads proportionally.

For all frames designed with this method, $K = 1.0$.

It was previously determined in the illustration of design by second-order analysis example that the second-order drift is less than 1.5 times the first-order drift (note that this check is properly made using the unreduced stiffnesses, EA and EI).

Thus, the notional load can be applied as a minimum lateral load, and that minimum is:

$$Y_i = 200 \text{ kips} + 200 \text{ kips}$$
$$= 400 \text{ kips}$$

$$N_i = 0.002Y_i$$
$$= 0.002(400 \text{ kips})$$
$$= 0.8 \text{ kips}$$

Because this notional load is less than the actual lateral load, it need not be applied. For a load combination that does not include a lateral load, the notional load would need to be included in the analysis.

For Column A, using first-order analysis and B_1-B_2 amplification:

$P_{nt} = 200$ kips, $P_{lt} = 0$ kips
$M_{nt} = 0$ kip-ft, $M_{lt} = 300$ kip-ft

To determine the second-order amplification, the reduced stiffness, EI^*, must be calculated.

$$\alpha P_r = 1.0(200 \text{ kips})$$
$$= 200 \text{ kips}$$

and

$$0.5P_y = 0.5F_yA_g$$
$$= 0.5(50 \text{ ksi})(26.5 \text{ in.}^2)$$
$$= 663 \text{ kips}$$

Thus, because $\alpha P_r < 0.5P_y$, $\tau_b = 1.0$ and

$$EI^* = 0.8\tau_b EI$$
$$= 0.8EI$$

For P-δ amplification, since there are no moments associated with the no-translation case, there is no need to calculate B_1. For P-Δ amplification, the reduced stiffness EI^* must be used to determine the first-order drift. Because $EI^* = 0.8EI$, the first-order drift based upon EI^* is 25% larger than that calculated previously. Thus,

$$\Delta_{1st} = 1.25(1.34 \text{ in.})$$
$$= 1.68 \text{ in.}$$

The first-order drift ratio is determined from the amplified drift of 1.68 in.

$$\Delta_{1st}/L = (1.68 \text{ in.})/(15 \text{ ft} \times 12 \text{ in./ft})$$
$$= 0.00933$$

For moment frames, $R_M = 0.85$ and from Equation C2-6b with $\Delta_H = \Delta_{1st}$ and $\Sigma H = 20$ kips,

$$\Sigma P_{e2} = R_M \frac{\Sigma H}{\left(\Delta_{1st}/L\right)}$$
$$= 0.85\frac{20 \text{ kips}}{(0.00933)}$$
$$= 1{,}820 \text{ kips}$$

For design by LRFD, $\alpha = 1.0$ and ΣP_{nt} is the sum of the gravity loads. Thus,

$$\alpha\Sigma P_{nt}/\Sigma P_{e2} = 1.0(200 \text{ kips} + 200 \text{ kips})/1{,}820 \text{ kips} = 0.220$$

From Equation C2-3, the amplification is:

$$B_2 = \frac{1}{1 - \frac{\alpha \Sigma P_{nt}}{\Sigma P_{e2}}} \geq 1$$
$$= \frac{1}{(1 - 0.220)} \geq 1.0$$
$$= 1.28 \geq 1.0$$
$$= 1.28$$

It is worth noting that use of the reduced axial stiffness, $EA^* = 0.8EA$, in members that contribute to lateral stability is also required in this method. However, due to the characteristics of the structures chosen for this example, there are no axial deformations that impact the stability of the structure.

The amplified axial force (Equation C2-1b) and associated design parameters for this method are:

$$P_r = P_{nt} + B_2 P_{lt}$$
$$= 200 \text{ kips} + 1.28(0 \text{ kips})$$
$$= 200 \text{ kips}$$

$$K_x = K_y = 1.0$$

$$L_x = L_y = 15 \text{ ft}$$

The amplified moment (Equation C2-1a) and associated design parameters for this method are:

$$M_{rx} = B_1 M_{nt} + B_2 M_{lt}$$
$$= (0 \text{ kip-ft}) + 1.28(300 \text{ kip-ft})$$
$$= 384 \text{ kip-ft}$$

$$C_b = 1.67$$

$$L_b = 15 \text{ ft}$$

Based upon these design parameters, the axial and strong-axis available flexural strengths of the ASTM A992 W14×90 are:

$$P_c = \phi_c P_n = 1{,}000 \text{ kips}$$
$$M_{cx} = \phi_b M_{nx} = 573 \text{ kip-ft}$$

To determine which interaction equation is applicable, the ratio of the required axial compressive strength to available axial compressive strength must be determined.

$$\frac{P_r}{P_c} = \frac{200 \text{ kips}}{1{,}000 \text{ kips}}$$
$$= 0.200$$

Thus, because $P_r/P_c \geq 0.2$, Equation H1-1a is applicable.

$$\frac{P_r}{P_c} + \frac{8}{9}\left(\frac{M_{rx}}{M_{cx}}\right) = 0.200 + \frac{8}{9}\left(\frac{384 \text{ kip-ft}}{573 \text{ kip-ft}}\right)$$
$$= 0.796$$

The W14×90 is adequate since $0.796 \leq 1.0$.

The Simplified Method

This method is provided in the AISC *Basic Design Values* Cards and the 13th Edition *Steel Construction Manual* (AISC, 2005b), and excerpted as shown in Figure 3. This simplified method is derived from the effective length method (Design by Second-Order Analysis; Section C2.2a) using B_1-B_2 amplification with B_1 taken equal to B_2. Note that the user note in Section C2.1b says that B_1 may be taken equal to B_2 as long as B_1 is less than 1.05. However, it is also conservative to take B_1 equal to B_2 any time B_1 is less than B_2. Although it cannot universally be stated that B_1 is always equal to or less than B_2, this is the case for typical framing. It is left to engineering judgment to confirm that this criterion is satisfied when applying the simplified method.

This method is permitted when the ratio of second-order drift, Δ_{2nd}, to first-order drift, Δ_{1st}, is equal to or less than 1.5 as with the Design by Second-Order Analysis method. It allows the use of a first-order analysis based on nominal stiffnesses, EA and EI, with a minimum lateral load $N_i = 0.002Y_i$, where Y_i is the total gravity load on level i from LRFD load combinations or ASD load combinations. The 1.6 multiplier on ASD load combinations is not used at this point but its effect is included in the determination of the amplification multiplier upon entering the table.

The ratio of total story gravity load (times 1.0 in LRFD, 1.6 in ASD) to the story lateral load is used to enter the table in Figure 3. The second-order amplification multiplier is determined from the value in the table corresponding to the calculated load ratio and design story drift limit. While linear interpolation between tabular values is permitted, it is important to note that the tabular values have, in essence, only two significant digits. Accordingly, the value determined should not be calculated to more than one decimal place. The tabular value is used to amplify all forces and moments in the analysis.

When the ratio of second-order drift to first-order drift is equal to or less than 1.1, $K = 1.0$ can be used in the design of moment frames. Otherwise, for moment frames, K is determined from a sidesway buckling analysis. For braced frames, $K = 1.0$.

For the example frame given in Figure 1, the minimum lateral load is:

$$Y_i = 200 \text{ kips} + 200 \text{ kips} = 400 \text{ kips}$$

$$N_i = 0.002Y_i = 0.002(400 \text{ kips}) = 0.8 \text{ kips}$$

Because this notional load is less than the actual lateral load, it need not be applied. For a load combination that does not include a lateral load, the notional load would need to be included in the analysis.

The actual first-order drift of the trial frame corresponds to a drift ratio of $L/134$ and the load ratio is:

$$1.0 \times (200 \text{ kips} + 200 \text{ kips})/(20 \text{ kips}) = 20$$

Entering the table in the column for a load ratio of 20, the corresponding multiplier for a drift ratio of $H/134$ is 1.3 (determined by interpolation to one decimal place). This multiplier is less than 1.5; thus, $\Delta_{2nd} < 1.5\Delta_{1st}$ and the use of this method is permitted. However, because the multiplier is greater than 1.1, K cannot be taken as 1.0 for column design in the moment frame with this method. Thus, K must be calculated, including the leaning column effect. Using the same approach as previously discussed (Lim and McNamara, 1972):

$$\Sigma P_{leaning}/\Sigma P_{stability} = (200 \text{ kips})/(200 \text{ kips}) = 1$$

$$K_x^* = K_x(1 + \Sigma P_{leaning}/\Sigma P_{stability})^{1/2} = 2.0(1 + 1)^{1/2} = 2.83$$

The amplified axial force (with the full axial force amplified by B_2) and associated design parameters for this method are:

$$P_r = 1.3P_u = 1.3 (200 \text{ kips}) = 260 \text{ kips}$$

$$K_x^* = 2.83, K_y = 1.0$$

$$L_x = L_y = 15 \text{ ft}$$

The amplified moment (with the full moment amplified by B_2) and associated design parameters for this method are:

$$M_{rx} = 1.3M_u = 1.3(300 \text{ kip-ft}) = 390 \text{ kip-ft}$$

$$C_b = 1.67$$

$$L_b = 15 \text{ ft}$$

Based on these design parameters, the available axial compressive strength and strong-axis available flexural strength of the ASTM A992 W14×90 are:

$$P_c = \phi_c P_n = 721 \text{ kips}$$
$$M_{cx} = \phi_b M_{nx} = 573 \text{ kip-ft}$$

To determine which interaction equation is applicable, the ratio of the required axial compressive strength to available axial compressive strength must be determined.

$$\frac{P_r}{P_c} = \frac{260 \text{ kips}}{721 \text{ kips}} = 0.361$$

Simplified Method

Step 1. Perform first-order analysis. Use 0.2% of total story gravity load as minimum lateral load in all load combinations.
Step 2. Establish the design story drift limit and determine the lateral load required to produce it.
Step 3. Determine the ratio of the total story gravity load to the lateral load determined in Step 2. For ASD, multiply by 1.6.
Step 4. Multiply first-order results by the tabular value. K=1, except for moment frames when the tabular value is greater than 1.1.

Design Story Drift Limit	Ratio from Step 3 (times 1.6 for ASD, 1.0 for LRFD)										
	0	5	10	20	30	40	50	60	80	100	120
H/100	1	1.1	1.1	1.3	1.4	When ratio exceeds 1.5, simplified method requires a stiffer structure.					
H/200	1	1	1.1	1.1	1.2	1.3	1.3	1.4			
H/300	1	1	1	1.1	1.1	1.2	1.2	1.3	1.4	1.5	
H/400	1	1	1	1.1	1.1	1.1	1.2	1.2	1.3	1.3	1.4
H/500	1	1	1	1	1.1	1.1	1.1	1.2	1.2	1.3	1.3

Fig. 3. Simplified method from AISC basic design values cards.

Thus, because $P_r/P_c \geq 0.2$, Equation H1-1a is applicable.

$$\frac{P_r}{P_c}+\frac{8}{9}\left(\frac{M_{rx}}{M_{cx}}\right)=0.361+\frac{8}{9}\left(\frac{390 \text{ kip-ft}}{573 \text{ kip-ft}}\right)$$
$$=0.966$$

The W14×90 is adequate since $0.966 \leq 1.0$.

Summary for the One-Bay Frame

All methods illustrated in the foregoing sections produce similar designs. The results are tabulated here for comparison, where the result of the beam-column interaction equation is given for each method. A lower interaction equation result for the same column shape signifies a prediction of higher strength.

Method	Interaction Equation
Second-Order	0.840
First-Order	0.811
Direct Analysis	0.796
Simplified	0.966

In this example, the direct analysis method predicts the highest strength, while the simplified method predicts the lowest strength. This would be expected because the Direct Analysis Method was developed as the most accurate approach while the simplified method was developed to produce a quick yet conservative solution.

The designs compared here are based on strength with no consideration of drift limitation, except to the extent that the actual drift impacts the magnitude of the second-order effects. The usual drift limits of approximately $L/400$ will necessitate framing members and configurations with more lateral stiffness than this frame provides. Hence, the designer may find that a frame configured for drift first will often require no increase in member size for strength, including second-order effects. This will be explored further with the three-bay frame.

THE THREE-BAY FRAME

For the frame shown in Figure 2, a trial shape is selected using a first-order drift limit of $L/600$ under a service level lateral load of 10 kips. Thereafter, that trial shape is used as the basis for comparison of the four methods used previously for the one-bay frame.

Selection of Trial Shape Based on the Drift Limit Only

For the dimensions shown in Figure 2:

$$L/600 = (15 \text{ ft} \times 12 \text{ in./ft})/600$$
$$= 0.300 \text{ in.}$$

The lateral stiffness of the frame depends on Columns D and E only, and based on a classical stiffness derivation with the given end conditions, it is calculated as follows:

$$k = 2 \times 3EI/L^3$$
$$= 2 \times 3(29{,}000 \text{ ksi})(I)/(15 \text{ ft} \times 12 \text{ in./ft})^3$$
$$= 0.0298(I)$$

With the service level lateral load on the frame of 10 kips:

$$0.0298(I) \geq (10 \text{ kips})/(0.300 \text{ in.})$$

Thus, I_{req} = 1,120 in.^{4} and an ASTM A992 W14×109 is selected as the trial shape with I_x = 1,240 in.^{4}

The actual lateral stiffness of the frame is:

$$k = 2 \times 3EI/L^3$$
$$= 2 \times 3(29{,}000 \text{ ksi})(1{,}240 \text{ in.}^4)/(15 \text{ ft} \times 12 \text{ in./ft})^3$$
$$= 37.0 \text{ kips/in.}$$

The corresponding first-order drift of the frame under the LRFD lateral load of 15 kips is:

$$\Delta_{1st} = (15 \text{ kips})/(37.0 \text{ kips/in.})$$
$$= 0.405 \text{ in.}$$

The first-order axial force, strong-axis moment, and design parameters for Columns D and E are:

P_u = 150 kips M_{ux} = (15 kips)(15 ft)/2
K_x = 2.0 = 113 kip-ft
K_y = 1.0 C_b = 1.67
$L_x = L_y$ = 15 ft L_b = 15 ft

Note that K_x = 2.0, the theoretical value for a column with a fixed base and pinned top, is used rather than the value of 2.1 recommended for design in the AISC *Specification* Commentary Table C-C2.2. The value of 2.0 is used because it is consistent with the formulation of the lateral stiffness calculation that follows. Note also that the impact of the leaning column on K_x is ignored in selecting the trial size, although it will be considered in subsequent sections when K_x cannot be taken equal to 1.0 for Column A. Out of the plane of the frame, K_y is taken as 1.0.

Design by Second-Order Analysis (Section C2.2a)

For the example frame given in Figure 2, the minimum lateral load is:

$$Y_i = 75 \text{ kips} + 150 \text{ kips} + 150 \text{ kips} + 75 \text{ kips}$$
$$= 450 \text{ kips}$$

$$N_i = 0.002\ Y_i$$
$$= 0.002(450 \text{ kips})$$
$$= 0.90 \text{ kips}$$

Because this notional load is less than the actual lateral load, it need not be applied.

For Columns D and E, using first-order analysis and B_1-B_2 amplification:

P_{nt} = 150 kips, P_{lt} = 0 kips
M_{nt} = 0 kip-ft, M_{lt} = 113 kip-ft

For P-δ amplification, because there are no moments associated with the no-translation case, there is no need to calculate B_1. For P-Δ amplification, the first-order drift ratio is determined from the calculated drift of 0.405 in. Thus,

$$\Delta_{1st}/L = (0.405 \text{ in.})/(15 \text{ ft} \times 12 \text{ in./ft}) = 0.00225$$

For moment frames, R_m = 0.85 and from Equation C2-6b with $\Delta_H = \Delta_{1st}$ and ΣH = 15 kips,

$$\Sigma P_{e2} = R_M \frac{\Sigma H}{\left(\Delta_{1st}/L\right)} = 0.85\frac{15 \text{ kips}}{(0.00225)} = 5{,}670 \text{ kips}$$

For design by LRFD, α = 1.0 and ΣP_{nt} is the sum of the gravity loads. Thus,

$$\alpha\Sigma P_{nt}/\Sigma P_{e2} = 1.0(75 \text{ kips} + 150 \text{ kips} + 150 \text{ kips} + 75 \text{ kips})/5{,}670 \text{ kips} = 0.0794$$

From Equation C2-3, the amplification is:

$$B_2 = \frac{1}{\left(1 - \frac{\alpha \Sigma P_{nt}}{\Sigma P_{e2}}\right)} \geq 1 = \frac{1}{(1 - 0.0794)} \geq 1.0 = 1.09 \geq 1.0 = 1.09$$

Because B_2 = 1.09, the second-order drift is less than 1.5 times the first-order drift. Thus, the use of this method is permitted. Because B_2 < 1.1, K can be taken as 1.0 for column design in the moment frame with this method.

The amplified axial force (Equation C2-1b) and associated design parameters for this method are:

$P_r = P_{nt} + B_2P_{lt}$
= 150 kips + 1.09(0 kips)
= 150 kips

$K_x = K_y$ = 1.0

$L_x = L_y$ = 15 ft

The amplified moment (Equation C2-1a) and associated design parameters for this method are:

$M_{rx} = B_1M_{nt} + B_2M_{lt}$
= (0 kip-ft) + 1.09 (113 kip-ft)
= 123 kip-ft

C_b = 1.67

L_b = 15 ft

Based on these design parameters, the available axial compressive strength and strong-axis available flexural strength of the ASTM A992 W14×109 are:

$P_c = \phi_c P_n$ = 1,220 kips
$M_{cx} = \phi_b M_{nx}$ = 720 kip-ft

To determine which interaction equation is applicable, the ratio of the required axial compressive strength to available axial compressive strength must be determined.

$$\frac{P_r}{P_c} = \frac{150 \text{ kips}}{1{,}220 \text{ kips}} = 0.123$$

Thus, because P_r/P_c < 0.2, Equation H1-1b is applicable.

$$\frac{P_r}{2P_c} + \frac{M_{rx}}{M_{cx}} = \frac{0.123}{2} + \frac{123 \text{ kip-ft}}{720 \text{ kip-ft}} = 0.232$$

The W14×109 is adequate because 0.232 ≤ 1.0.

Design by First-Order Analysis (Section C2.2b)

For the example frame given in Figure 2, the additional lateral load (with $\Delta = \Delta_{1st}$) is:

$\Delta_{1st}/L = (0.405 \text{ in.})/(15 \text{ ft} \times 12 \text{ in./ft}) = 0.00225$

Y_i = 75 kips + 150 kips + 150 kips + 75 kips
= 450 kips

$N_i = 2.1(\Delta_{1st}/L)Y_i \geq 0.0042Y_i$
= 2.1(0.00225)(450 kips) ≥ 0.0042(450 kips)
= 2.13 kips ≥ 1.89 kips
= 2.13 kips

It was previously determined in the illustration of design by second-order analysis example that the second-order drift is less than 1.5 times the first-order drift. Additionally,

αP_r = 1.0(150 kips) = 150 kips

and for the ASTM A992 W14×109,

$0.5P_y = 0.5F_yA_g$
= 0.5(50 ksi)(32.0 in.^{2})
= 800 kips

Because $\Delta_{2nd} < 1.5\Delta_{1st}$ and $\alpha P_r < 0.5P_y$, the use of this method is permitted.

The loading for this method is the same as shown in Figure 2, except for the addition of a notional load of 2.13 kips coincident with the lateral load of 15 kips shown, resulting in a moment M_u of 128 kip-ft in each column.

This moment must be amplified by B_1 as determined from Equation C2-2. The Euler buckling load is calculated with $K_1 = 1.0$. Thus,

$$\begin{aligned} P_{e1} &= \pi^2 EI / (K_1 L)^2 \\ &= \pi^2(29{,}000 \text{ ksi})(1{,}240 \text{ in.}^4)/(1.0 \times 15 \text{ ft} \times 12 \text{ in./ft})^2 \\ &= 11{,}000 \text{ kips} \end{aligned}$$

Because the moment on one end of the column is zero, the moment gradient term is:

$$\begin{aligned} C_m &= 0.6 - 0.4(M_1/M_2) \\ &= 0.6 - 0.4(0/128) \\ &= 0.6 \end{aligned}$$

From Equation C2-2,

$$\alpha P_r/P_{e1} = 1.0(150 \text{ kips})/(11{,}000 \text{ kips}) = 0.0136$$

$$B_1 = \frac{C_m}{1 - \dfrac{\alpha P_r}{P_{e1}}} \geq 1$$

$$= \frac{0.6}{1 - 0.0136} \geq 1.0$$

$$= 0.608 \geq 1.0$$

$$= 1.0$$

The axial force and associated design parameters for this method are:

$$P_r = 150 \text{ kips}$$
$$K_x = K_y = 1.0$$
$$L_x = L_y = 15 \text{ ft}$$

The amplified moment and associated design parameters for this method are:

$$M_{rx} = B_1 M_u = 1.0(128 \text{ kip-ft}) = 128 \text{ kip-ft}$$
$$C_b = 1.67$$
$$L_b = 15 \text{ ft}$$

Based on these design parameters, the available axial compressive strength and strong-axis available flexural strengths of the ASTM A992 W14×109 are:

$$P_c = \phi_c P_n = 1{,}220 \text{ kips}$$
$$M_{cx} = \phi_b M_{nx} = 720 \text{ kip-ft}$$

To determine which interaction equation is applicable, the ratio of the required axial compressive strength to available axial compressive strength must be determined.

$$\frac{P_r}{P_c} = \frac{150 \text{ kips}}{1{,}220 \text{ kips}} = 0.123$$

Thus, because $P_r/P_c < 0.2$, Equation H1-1b is applicable.

$$\frac{P_r}{2P_c} + \frac{M_{rx}}{M_{cx}} = \frac{0.123}{2} + \frac{128 \text{ kip-ft}}{720 \text{ kip-ft}} = 0.239$$

The W14×109 is adequate because $0.239 \leq 1.0$.

Direct Analysis Method (Appendix 7)

It was previously determined in the illustration of design by second-order analysis example that the second-order drift is less than 1.5 times the first-order drift (note that this check is properly made using the unreduced stiffness *EI*). Thus, the notional load can be applied as minimum lateral load, and that minimum is:

$$Y_i = 75 \text{ kips} + 150 \text{ kips} + 150 \text{ kips} + 75 \text{ kips} = 450 \text{ kips}$$

$$N_i = 0.002Y_i = 0.002(450 \text{ kips}) = 0.9 \text{ kip}$$

Because this notional load is less than the actual lateral load, it need not be applied.

For Columns D and E, using first-order analysis and B_1-B_2 amplification:

$$P_{nt} = 150 \text{ kips}, \; P_{lt} = 0 \text{ kips}$$
$$M_{nt} = 0 \text{ kip-ft}, \; M_{lt} = 113 \text{ kip-ft}$$

To determine the second-order amplification, the reduced stiffness, *EI**, must be calculated.

$$\alpha P_r = 1.0(150 \text{ kips}) = 150 \text{ kips}$$

and for the ASTM A992 W14×109,

$$0.5P_y = 0.5F_y A_g = 0.5(50 \text{ ksi})(32.0 \text{ in.}^2) = 800 \text{ kips}$$

Thus, because $\alpha P_r < 0.5P_y$, $\tau_b = 1.0$ and

$$EI^* = 0.8\tau_b EI = 0.8EI$$

For *P*-δ amplification, because there are no moments associated with the no-translation case, there is no need to calculate B_1. For *P*-Δ amplification, the reduced stiffness *EI** must be used to determine the first-order drift. Because

$EI^* = 0.8EI$, the first-order drift based on EI^* is 25% larger than that calculated previously. Thus,

$$\Delta_{1st} = 1.25(0.405 \text{ in.}) = 0.506 \text{ in.}$$

The first-order drift ratio is determined from the amplified drift of 0.506 in.

$$\Delta_{1st}/L = (0.506 \text{ in.})/(15 \text{ ft} \times 12 \text{ in./ft}) = 0.00281$$

For moment frames, $R_M = 0.85$ and from Equation C2-6b with $\Delta_H = \Delta_{1st}$ and $\Sigma H = 15$ kips,

$$\Sigma P_{e2} = R_M \frac{\Sigma H}{\left(\Delta_{1st}/L\right)} = 0.85\frac{15 \text{ kips}}{(0.00281)} = 4{,}540 \text{ kips}$$

For design by LRFD, $\alpha = 1.0$ and ΣP_{nt} is the sum of the gravity loads. Thus,

$$\alpha\Sigma P_{nt}/\Sigma P_{e2} = 1.0(75 \text{ kips} + 150 \text{ kips} + 150 \text{ kips} + 75 \text{ kips})/4{,}540 \text{ kips} = 0.0991$$

From Equation C2-3, the amplification is:

$$B_2 = \frac{1}{\left(1 - \frac{\alpha\Sigma P_{nt}}{\Sigma P_{e2}}\right)} \geq 1$$

$$= \frac{1}{(1 - 0.0991)} \geq 1.0$$

$$= 1.11 \geq 1.0$$

$$= 1.11$$

It is worth noting that use of the reduced axial stiffness, $EA^* = 0.8EA$, in members that contribute to lateral stability is also required in this method. However, due to the characteristics of the structures chosen for this example, there are no axial deformations that impact the stability of the structure.

The amplified axial force (Equation C2-1b) and associated design parameters for this method are:

$$P_r = P_{nt} + B_2P_{lt} = 150 \text{ kips} + 1.11(0 \text{ kips}) = 150 \text{ kips}$$

$$K_x = K_y = 1.0$$

$$L_x = L_y = 15 \text{ ft}$$

The amplified moment (Equation C2-1a) and associated design parameters for this method are:

$$M_{rx} = B_1M_{nt} + B_2M_{lt} = (0 \text{ kip-ft}) + 1.11(113 \text{ kip-ft}) = 125 \text{ kip-ft}$$

$$C_b = 1.67$$

$$L_b = 15 \text{ ft}$$

Based on these design parameters, the available axial compressive strength and strong-axis available flexural strengths of the ASTM A992 W14×109 are:

$$P_c = \phi_c P_n = 1{,}220 \text{ kips}$$

$$M_{cx} = \phi_b M_{nx} = 720 \text{ kip-ft}$$

To determine which interaction equation is applicable, the ratio of the required axial compressive strength to available axial compressive strength must be determined.

$$\frac{P_r}{P_c} = \frac{150 \text{ kips}}{1{,}220 \text{ kips}} = 0.123$$

Thus, because $P_r/P_c < 0.2$, Equation H1-1b is applicable.

$$\frac{P_r}{2P_c} + \frac{M_{rx}}{M_{cx}} = \frac{0.123}{2} + \frac{125 \text{ kip-ft}}{720 \text{ kip-ft}} = 0.235$$

The W14×109 is adequate because $0.235 \leq 1.0$.

The Simplified Method

For the example frame given in Figure 2, the minimum lateral load is:

$$Y_i = 75 \text{ kips} + 150 \text{ kips} + 150 \text{ kips} + 75 \text{ kips} = 450 \text{ kips}$$

$$N_i = 0.002Y_i = 0.002(450 \text{ kips}) = 0.9 \text{ kips}$$

Because this notional load is less than the actual lateral load, it need not be applied.

The 15-kip lateral load produces slightly less drift than that corresponding to the design story drift limit because the W14×109 has $I = 1{,}240$ in.^{4} (versus the 1,120 in.^{4} required to limit drift to $L/400$). The lateral load required to produce the design story drift limit is:

$$15 \text{ kips} \times (1{,}240 \text{ in.}^4)/(1{,}120 \text{ in.}^4) = 16.6 \text{ kips}$$

The load ratio is then:

$$1.0 \times (75 \text{ kips} + 150 \text{ kips} + 150 \text{ kips} + 75 \text{ kips})/(16.6 \text{ kips}) = 27.1$$

Entering the table in the row for $H/400$, the corresponding multiplier for a load ratio of 27.1 is 1.1 (determined by interpolation to one decimal place). Because this multiplier is less than 1.5, $\Delta_{2nd} < 1.5\Delta_{1st}$ and the use of this method is permitted. Additionally, because the multiplier is equal to 1.1, K can be taken as 1.0 for column design in the moment frame with this method.

The amplified axial force (with the full axial force amplified by B_2) and associated design parameters for this method are:

$$P_r = 1.1P_u$$
$$= 1.1(150 \text{ kips})$$
$$= 165 \text{ kips}$$

$$K_x = K_y = 1.0$$

$$L_x = L_y = 15 \text{ ft}$$

The amplified moment (with the full moment amplified by B_2) and associated design parameters for this method are:

$$M_{rx} = 1.1M_u$$
$$= 1.1(113 \text{ kip-ft})$$
$$= 124 \text{ kip-ft}$$

$$C_b = 1.67$$

$$L_b = 15 \text{ ft}$$

Based on these design parameters, the axial and strong-axis flexural available strengths of the ASTM A992 W14×109 are:

$$P_c = \phi_c P_n = 1{,}220 \text{ kips}$$
$$M_{cx} = \phi_b M_{nx} = 720 \text{ kip-ft}$$

To determine which interaction equation is applicable, the ratio of the required axial compressive strength to available axial compressive strength must be determined.

$$\frac{P_r}{P_c} = \frac{165 \text{ kips}}{1{,}220 \text{ kips}}$$
$$= 0.135$$

Thus, because $P_r/P_c < 0.2$, Equation H1-1b is applicable.

$$\frac{P_r}{2P_c} + \frac{M_{rx}}{M_{cx}} = \frac{0.135}{2} + \frac{124 \text{ kip-ft}}{720 \text{ kip-ft}}$$
$$= 0.240$$

The W14×109 is adequate because $0.240 \le 1.0$.

Summary for the Three-Bay Frame

As before, all methods produce similar designs. The result of the beam-column interaction equation for each method is:

Method	Interaction Equation
Second-Order	0.232
First-Order	0.239
Direct Analysis	0.235
Simplified	0.240

In this example, the interaction equations predict values that are so close to each other that there is no practical difference in the results.

CONCLUSIONS

The following conclusions can be drawn from the foregoing examples:

1. If conservative assumptions are acceptable, the easiest method to apply is the Simplified Method, particularly when the drift limit is such that K can be taken equal to 1.

2. None of the analysis methods in the AISC *Specification* are particularly difficult to use. The First-Order Analysis Method and Direct Analysis Method both eliminate the need to calculate K, which can be a tedious process based upon assumptions that are rarely satisfied in real structures. Nonetheless, those who prefer to continue to use the approach of past specifications, the Effective Length Method, can do so, provided they incorporate the new requirement of a minimum lateral load in all load combinations.

3. Second-order effects and leaning columns have a significant impact on strength requirements, but usual drift limits such as $L/400$ sometimes can result in framing that requires no increase in member size for strength. For frames with little or no lateral load and/or heavy floor loading, it is more likely that stability will control, regardless of the drift limits. This should not be taken as a blanket indication that the use of a drift limit eliminates the need to consider stability effects. Rather, it simply means that drift-controlled designs may be less sensitive to second-order effects because the framing is naturally stiffer and provides reserve strength. Drift limits also result in significant simplification of the analysis requirements when the increased framing stiffness allows more frequent use of the simplifications allowed in the various methods, such as the use of $K = 1$.

REFERENCES

AISC (2005a), *Specification for Structural Steel Buildings*, ANSI/AISC 360-05, American Institute of Steel Construction, Chicago, IL.

AISC (2005b), *Steel Construction Manual*, 13th ed., American Institute of Steel Construction, Chicago, IL.

Geschwindner, L.F., Disque, R.O. and Bjorhovde, R. (1994), *Load and Resistance Factor Design of Steel Structures*, Prentice Hall, Englewood Cliffs, NJ.

Lim, L.C. and McNamara, R.J. (1972), "Stability of Novel Building System," Structural Design of Tall Buildings, Vol. II-16, *Proceedings*, ASCE-IABSE International Conference on the Planning and Design of Tall Buildings, Bethlehem, PA, pp. 499–524.

Fracture Modeling of Rectangular Hollow Section Steel Braces

XIANG DING, DOUGLAS FOUTCH and SANG-WHAN HAN

Steel-braced frames are widely used in all regions of the United States including those with high levels of seismicity. Rectangular hollow sections (RHSs) are popular because of good section properties and ease of construction. A refined beam model has been developed which is efficient for use in finite element models of buildings. It accounts for local buckling and fracture in the brace and is shown to have good accuracy for nonlinear seismic analyses.

Braced frames possess sufficient lateral stiffness to inhibit large deformation under small to moderate earthquake motions. When the number of bays in one direction of a structure is limited, moment frames may not provide enough stiffness or be designed economically. Concentrically braced frames (CBFs) are more economical than eccentrically braced frames (EBFs), though the latter are highly recommended for earthquake resistance due to their good ductility (AISC, 2005b). Typical CBFs may use X-bracing, diagonal bracing, K-bracing, V-bracing, and inverted V-bracing. Architects prefer inverted V-bracing or diagonal bracing to X-bracing as the former provides for the convenience of door openings within the braced bays. The connections of the braces to gusset plates are much easier to fabricate than moment connections in moment frames so they are more economical to use.

Nonlinear behavior of braces and braced frames has been investigated by scientists since the 1970s. Numerous experimental studies have been performed on the inelastic cyclic response of bracing members for steel concentrically braced frames (Kahn and Hanson, 1976; Jain, Goel and Hanson, 1978; Popov and Black, 1981; Goel and El-Tayem, 1986). These investigations showed that bracing members typically exhibit nonsymmetrical hysteresis behavior, with strength degradation in compression and deformation accumulation of permanent elongation in tension. There are several principal factors affecting the behavior of braces.

Xiang Ding is principal structural engineer, Plant Engineering Services (Fluor), Baton Rouge, LA.

Douglas Foutch is professor of civil and environmental engineering, University of Illinois, Urbana, IL.

Sang-Whan Han is professor of architectural engineering, Hanyang University, Seoul, South Korea.

Slenderness Ratio, *KL/r*

K is the effective length factor, *L* is the unbraced length, and *r* is the radius of gyration. The energy dissipation capacity generally increases when the brace slenderness ratio is reduced (Remennikov and Walpole, 1997). The maximum brace slenderness ratio is specified in the code in order to provide a minimum level of energy dissipation. Tests performed on various brace specimens with different end conditions indicated that the effective length concept developed from the elastic theory is also applicable in the inelastic range to assess the ability of braces to dissipate seismic input energy.

Width-Thickness Ratio, *b/t*

Local buckling of the web or flanges of brace members due to large width-thickness ratios sometimes occurs before overall buckling and triggers overall buckling. Severe local buckling causes significant reductions in compressive capacity of the brace and leads to fracture in tension, which not only deprives the system of energy dissipation but also may result in collapse of the building. Local buckling issues are more difficult to simulate than overall buckling. For rectangular hollow sections (RHSs), the width of flanges or webs is the clear distance between webs or flanges less the inside corner radius on each side. If the corner radius is not known, the width shall be taken as the corresponding outside dimension minus three times the thickness. The thickness, *t*, shall be taken as the design wall thickness, per Section B3.12 of the AISC *Specification for Structural Steel Buildings* (AISC, 2005a).

Connection Restraint and Brace Configuration

Connection restraint at brace ends not only affects brace stiffness and strength but also affects fracture. Restraints at the ends of bracing members reduce their effective unbraced length, participate in energy-dissipation and, thereby, improve their seismic behavior. Brace slenderness can also be reduced by adopting an X-bracing configuration.

Ikeda and Mahin (1986) presented a model by assuming a deflected shape function for the brace and solving each of the axial displacement components. The analytic and experimental hysteresis loops were compared and found to be acceptable. Lee and Goel (1987) developed hysteresis models of a brace after studying the merits and demerits of Ikeda's model, Jain's model (Jain et al., 1978) and Liu and Goel's model (Liu, 1987). The analysis results were reported in good agreement with the corresponding experimental results.

Essentially, a brace carries axial force and bending moment. Remennikov and Walpole (1997) proposed a P-M interaction yield surface function based on stepwise regression analysis. Assuming the plastic hinge occurs at the brace midspan, the right half was taken out to decompose its axial deformation into elastic axial deformation, geometric shortening deformation, plastic hinge deformation, and tensile yield deformation. It was suggested that more stringent regulations should be imposed on the use of V or inverted V-braced frames in high seismicity areas. There are some requirements for those braced frames (AISC, 2005b): beams intersected by the V or inverted V-braces should not fail under the axial force of one brace when the other brace has buckled; those beams should also be laterally braced to prevent lateral buckling.

EXPERIMENTAL STUDIES ON RHS BRACES

Rectangular hollow sections are very effective in compression and their use for braces forms an efficient means of resisting lateral seismic loads and satisfying code limits on maximum brace slenderness ratio. Moreover, RHSs have large flexural and torsional stiffness due to their hollow and closed shape. Studies by Gugerli and Goel (1984) and Lee and Goel (1987) showed that bracing members made of RHSs experienced premature fractures soon after severe local buckling even though those sections satisfied the AISC requirements for compact sections. Lee and Goel (1987) reported the experiments on seismic behavior of hollow and concrete-filled square tubular bracing members. The test results showed that when the width-thickness ratio of hollow specimens was reduced from 30 to 14, the initial and the severe local buckling were much delayed and consequently, the fracture life increased. In the test, another veiled fact is that semi-fixed braces can dissipate more energy than fixed braces. Although the loading history emphasized compression, the test results of some specimens can be utilized for regression analysis of fracture life in this study.

Recently, an experimental study on buckling and fracture of single RHS steel brace specimens with nominal yielding strength of 345 MPa (50 ksi) has been conducted in Korea (Han, Wook and Foutch, 2006). The slenderness ratio, KL/r, ranges from 70 to 90 for the specimens. A typical test scheme and the load history are shown in Figures 1 and 2, respectively (1 mm = 0.0394 in.). Although the story displacement is set up to reach 5% drift, the ultimate story drifts before brace fracture were between 2% and 4%.

The experimental results showed that the occurrence and severity of the local buckling, and the fracture mode and life, depend strongly on b/t ratios of the specimens. Based on the observation of local and overall buckling in the test, the sequence of buckling was classified into three buckling modes: local buckling mode, overall-local buckling mode, and overall buckling mode (Han et al., 2006).

Local Buckling Mode (L Mode)

The specimens in the L mode experienced local buckling prior to overall buckling when the compression force reached a buckling load, P_{cr}. In a few cycles after local buckling occurred, the specimens fractured at the midspan section under

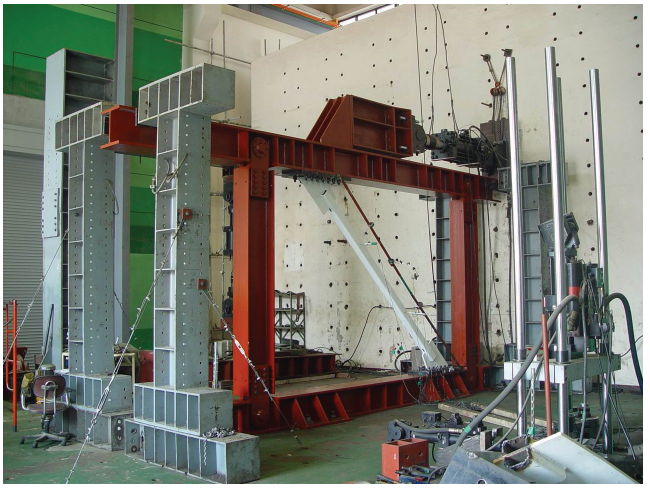

Fig. 1. A typical test specimen and the loading scheme.

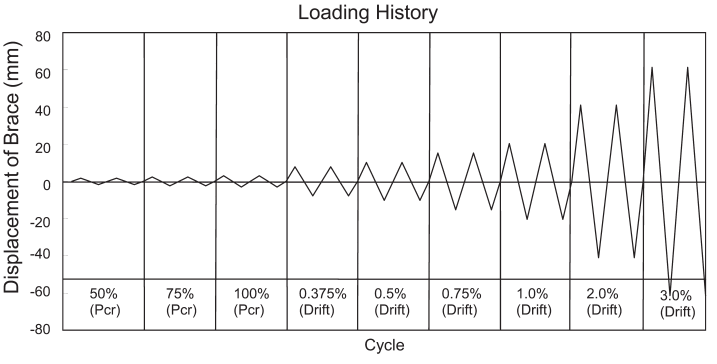

Fig. 2. Loading history of the test braces.

tension due to large plastic deformation caused by severe local buckling. Specimens with a noncompact width-thickness ratio (>18) failed in this sequence (L mode).

Overall-Local Buckling Mode (O-L Mode)

In this mode, bracing members experienced overall buckling (Figure 3) and the compression force reached a buckling load, P_{cr}, prior to the occurrence of local buckling. On the seventh cycle of compression, with a drift ratio of 0.375%, overall buckling occurred. On cycles 13 to 16, compression local buckling occurred. With an increase in the loading cycle, local buckling became more severe (Figure 4). In the following two cycles, fine wrinkles appeared where local buckling was present. Cracks were observed at the two corners near the flange opposite to the overall buckling direction ("inner flange") at the midspan. On the following cycles of tension, the cracks were propagated across the section and led to fracture at the midspan (see Figure 3d).

In this study, specimens with moderate *b/t* ratios of 13 to 18 fractured in this mode. The brace hysteresis curve under cyclic load is shown in Figure 5. Compared with specimens in the L mode, O-L mode specimens had better hysteresis behavior. This is attributed to a smaller *b/t* ratio that delayed the occurrence of local buckling and reduced the severity of local buckling in a given loading cycle.

(a) Overall buckling (–0.375%).

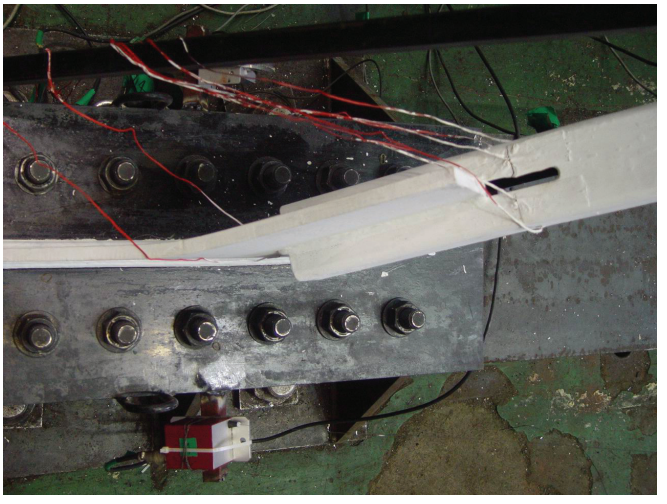

(b) Gusset plate buckling (–2%).

(c) Local buckling (–2%).

(d) Detail of fracture.

Fig. 3. Setup, buckling and fracture of specimen 100×100×6 #1 (O-L mode).

Overall Buckling Mode (O Mode)

Specimens with *b/t* ratios less than 13 fell into this category. Early in the loading stage, these specimens fractured under tension at the slotted end of the specimen, with appreciable distortion at the fracture section. No local buckling occurred, but overall buckling in these specimens was observed. It is important to note that the details of slots and connections between bracing member and gusset plates in the specimens followed the AISC *Steel Construction Manual* (AISC, 2005c). If the net section at the slot had the strength required by the AISC *Seismic Provisions* (AISC, 2005b), the overall buckling may successfully bring secondary bending moment to the gusset plate, and potentially a plastic hinge could be developed there.

Fracture can always be attributed to cracks in the wall of the brace due to severe plasticity caused by local buckling or excessive elongation. The local buckling mode and the overall-local buckling mode accompany relatively ductile failure in which fracture occurs at midspan due to large cyclic plastic deformation. The overall buckling mode will lead to brittle and unfavorable failure in which fracture occurs due to high concentrated stress at the sections with least net area or with initial fabrication defects such as a sharp cut at slots and embedded-cracks in or adjacent to welds, etc. However, reinforcement at weak net sections at slots and good fabrication practices can prevent braces from fracturing there. Therefore, brace fracture in the local buckling mode and the overall-local buckling mode will be discussed later.

When a single brace is subjected to displacement-controlled cyclic loads, the main failure mode is fracture in tension cycles. Local buckling eventually develops in the plastic hinge that forms in the brace. Fracture can be always attributed to the cracks that develop in the wall of the brace due to severe plasticity caused by local buckling. Fracture of the brace then rapidly occurs when it is subsequently pulled in tension. The tensile stiffness of the braces will decrease under cyclic loads because overall buckling results in the secondary bending moment and local buckling reduces the effective cross-section area at the midspan, which lead to premature tensile yielding. The brace slackness due to the tensile elongation brings a "free play" before the brace recovers the compressive stiffness in the subsequent compression cycles (Figure 5). Therefore, the post-buckling stiffness of those bracing systems declines very rapidly.

FINITE ELEMENT MODELING OF BRACES AND BRACE CONNECTIONS

Modeling of Brace Connections

Bracing connections act quite differently from the postulated ideal pin-joints. Gusset plates provide braces with stronger in-plane restraint than out-of-plane restraint, so V- or inverted-V-braces made of square hollow tubes are more likely to buckle out of plane due to longer effective unbraced length out of plane. This is also true for X braces due to the intersecting joint. There should be enough space left between these braces and partitions or cladding within the bay of braced frames to allow this deformation to occur without impacting walls or claddings. Out-of-plane plastic deformation capacity at a gusset plate is recommended for design of the joints (AISC, 2005b), as shown in Figure 6.

In the brace tests in Korea (Han et al., 2006), the plastic zone in the gusset plates caused by out-of-plane bending moment, as shown in Figure 7, is about 3*t* wide and 1*t* away

Fig. 4. Local buckling of brace 100×100×6.

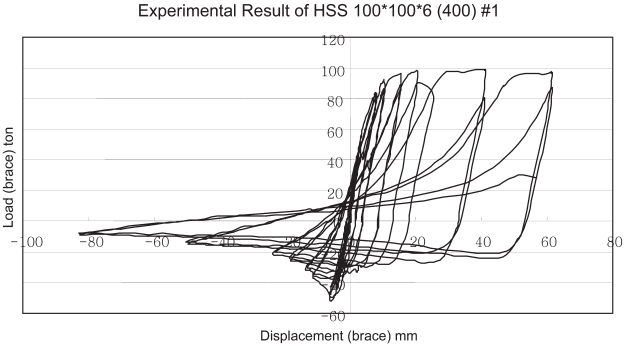

Fig. 5. Experimental hysteresis loops of specimen #1.

from the brace end, where t is thickness of the gusset plate. The gusset plates remain almost elastic elsewhere. Thus, gusset plates can be modeled as two beam segments (B33 in Abaqus). Considering the restraint from welds, twice the thickness of the gusset plate is used as the breadth of the beam element for the rest of the gusset plate other than the segment for plastic hinge. The modeling scheme of the brace connections is as shown in Figure 6. Each brace is modeled by 20 beam elements, and brace fracture is modeled by a special Abaqus user element discussed later.

Refined Beam Element Model

A refined beam element model has been widely used to simulate bracing members and struts. By dividing a brace into many segments, geometrical nonlinearity of the brace is easily included. The effect of overall buckling as well as slenderness ratio can be taken into account by the refined beam element model in the Abaqus program. A single beam cannot adequately detect the plasticity along the whole length. More accurate material and geometrical nonlinearity is reflected in the refined beam modeling.

A numerical simulation for specimen #1 of the brace tests in Korea (Han et al. 2006) has been selected to examine the refined modeling for Abaqus. The single brace with a length 3250 mm (10 ft 4 in.) is divided into about 20 elements to ensure good accuracy of geometrical nonlinearity. The gusset plates are 16 mm (⅝ in.) thick. The out-of-plane imperfection ratio of the strut is assumed as 0.1% (Gu and Chan, 2004). The out-of-plane imperfection curvature is assumed parabolic. Steel strain hardening ratio is set as 1%. Figures 5 and 8 are, respectively, the experimental and computed hysteresis loops of Specimen HSS100×100×6 #1 (HSS4×4×¼ in US units, 1 ton = 2.205 kips). Local buckling of the brace flange before fracture does not affect the hysteresis loop of the brace to a large degree. Accordingly, the refined beam element model can be applied to nonlinear analysis of braces.

Partial Shell Element Model

To study fracture of braces of a structural system at grain size level is not feasible for building structures. Fracture of structural metals under tensile loading usually occurs by a damage accumulation process involving void nucleation, void growth, and void coalescence (Venson and Voyiadjis, 2001). Material failure is controlled primarily by void growth and void coalescence, so most fatigue and fracture studies of metal are done in the field of continuum mechanics. Unless fine element types such as shell elements or solid elements are used for brace analyses, we cannot determine the actual concentrative and excessive strain and stress at the fracture location of the brace. One hinge region needs about 3,000 shell elements to simulate the phenomena (Figure 9). Due to very large computational work involved, shell element model simulation for crack development is not realistic for nonlinear dynamic analyses of building structural systems.

However, shell element modeling can be used to investigate local buckling of braces because beam element analysis cannot address that solely. In order to save computational time, the shell mesh only applies to the region near the local buckling and beam elements are used elsewhere. A rigid pad connects the beam element and shell elements at each transition, which was proven not to induce stress concentration (Figures 12 and 13). This model is called a partial shell element model, as shown in Figure 10. The computed hysteresis loops of the test braces in Korea using a partial shell

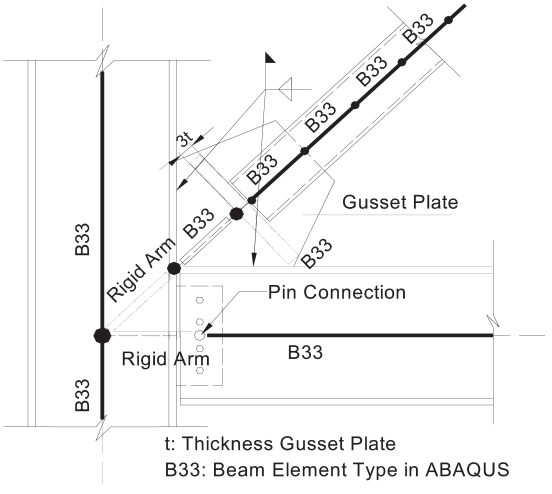

Fig. 6. Modeling scheme of the connection.

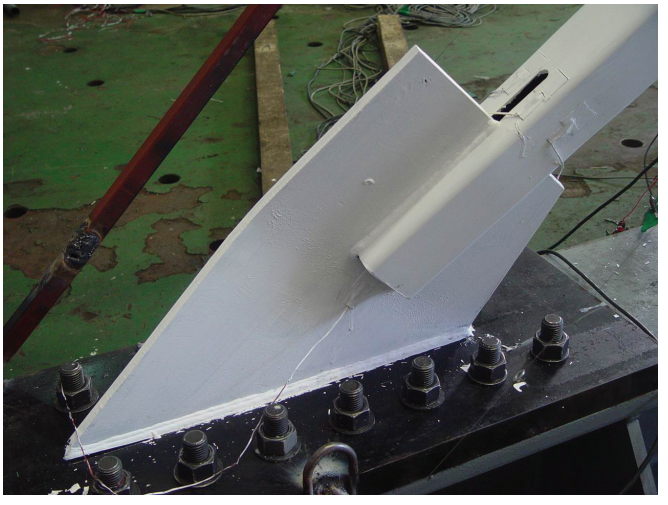

Fig. 7. Plastic zone of gusset plate.

element model and a full shell element model are identical. The buckling load and load time of the test braces computed by this model match the test results very well. Figures 4 and 11 show the local buckling deformation of the test specimen HSS100×100×6 and the simulation of the partial shell model. Figures 12 and 13 display the high stress of more than 0.1 ton/mm^2 (142 ksi) due to excessive plastic deformation where local buckling occurs. The partial shell element model also predicts the local buckling load of RHS braces under monotonic compression load very accurately (Figures 4, 11 and 14).

Although local buckling dominates the fracture as discussed later, by comparing the hysteresis curves of a brace specimen by the refined beam element model and the partial shell element model (Figure 15), it is obvious that local buckling does not affect the overall stiffness of braces to a large degree. The results of the two modelings match the experimental one very well (Figures 5, 8 and 15). For braced frames, the refined beam element model is good for brace simulations if local buckling and fracture can be detected in the model.

Local Buckling and Fracture Modeling

Inelastic local buckling in braces also accompanies plastic hinge development. In order to detect the concentrated deformation at local buckling, we can put appropriately finer beam elements at the places where the hinge could occur, most likely the midspan. By comparing the strains of these beam elements and those of the corresponding shell elements and the test results, we can find a way to determine local buckling and fracture just by using beam elements. From the

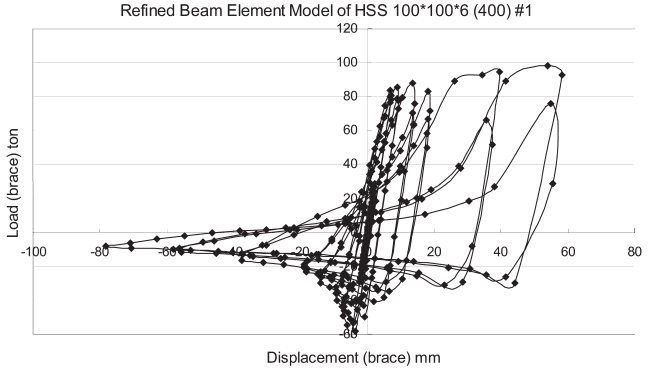

Fig. 8. Computed hysteresis loops of specimen #1.

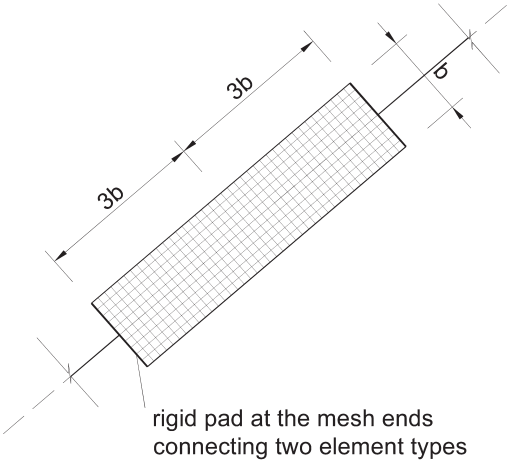

Fig. 9. Shell mesh for detecting local buckling.

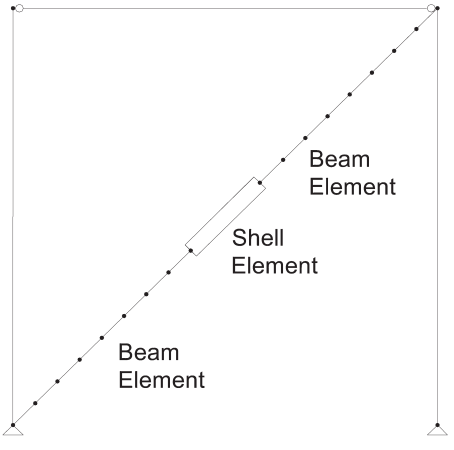

Fig. 10. Finite element scheme for the test.

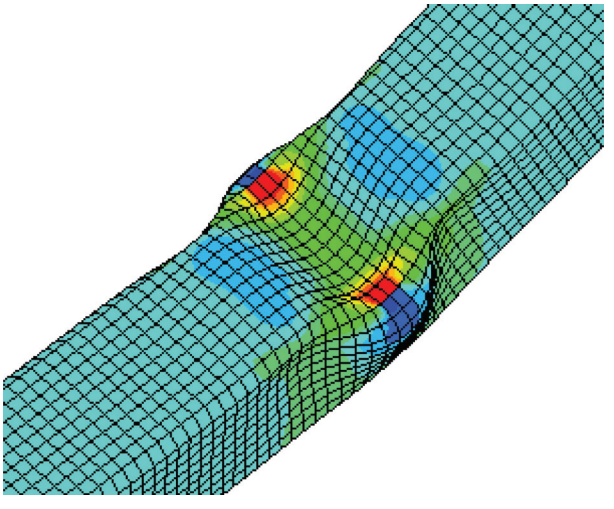

Fig. 11. Shell mesh simulation of brace 100×100×6.

photos of the test specimens and the finite element analysis results (Figures 4, 12 and 14), we can see that half of the cross-section size is a very good value as the length of those finer beam elements. Actually, the local buckling range of an RHS brace along its length is about equal to the flange width.

Therefore, a beam-connector-beam (BCB) element model is proposed. The two beam elements are used to predict local buckling and fracture while the connector element is used as a switch to simulate the discontinuity of beam after fracture because the beam elements cannot be disconnected by themselves. As shown in Figure 16, and as defined in the user element BCB element subroutine for Abaqus (2004), node I and node J are the nodes of element 1; node K and node L are the nodes of element 2. Between the two elements, a connector element with six degrees of freedom is set to connect node J and node K. The stiffness matrix of this connector element can be composed of the stiffness of the six springs in the three translational directions and the three rotational directions, which are extremely large before fracture and extremely small after fracture. The real-time nodal displacements can be monitored in Abaqus so as to determine the status of the two beam elements. Both of them are modeled as fiber beam elements in the Abaqus subroutine. Eight fibers (using brace material) for each beam element are employed to carry out the real-time detection of nominal stress and strain. One fiber is placed at each corner of the brace and one at the centerline of each face. Therefore, nominal stress and strain at the four corners and the four face centers of the assumed fracture section can be obtained at each load step to judge local buckling and fracture of the brace.

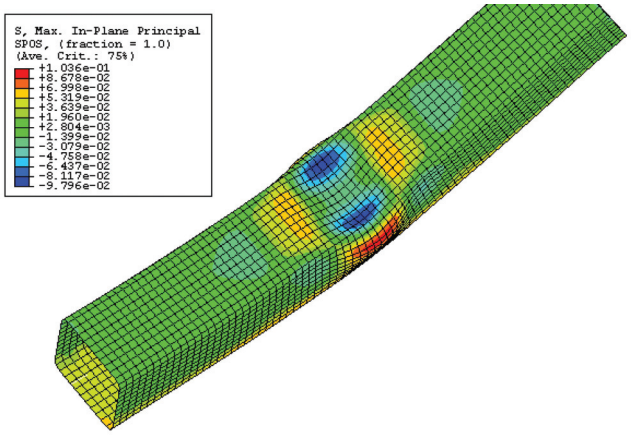

Fig. 12. Outside stress of brace 100×100×6.

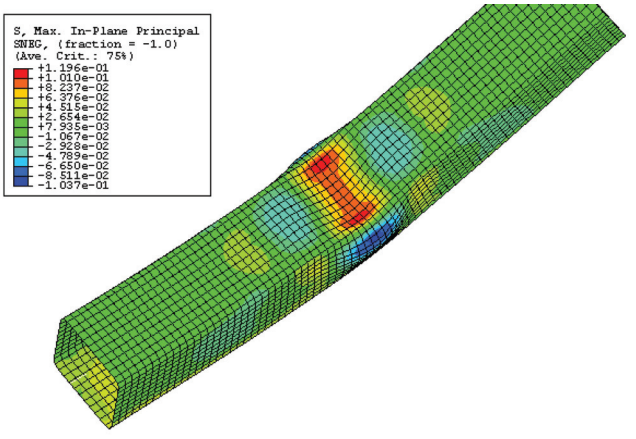

Fig. 13. Inside stress of brace 100×100×6.

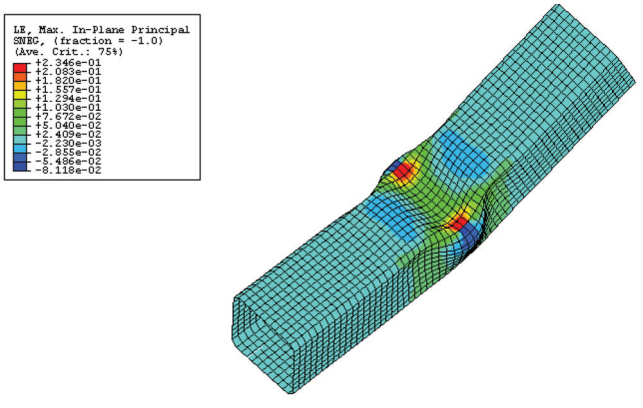

Fig. 14. The deformation upon local buckling.

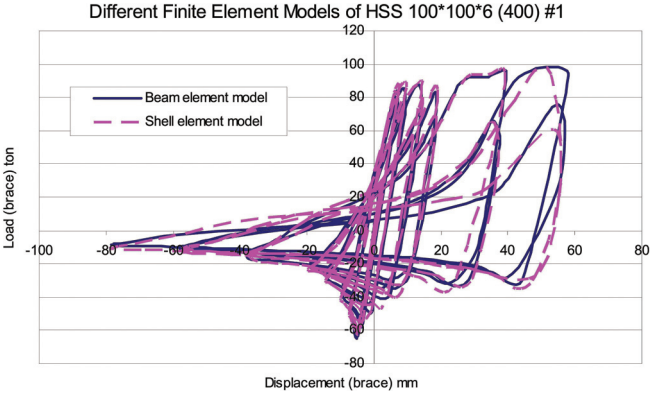

Fig. 15. Hysteresis curves of refined beam element model and partial shell element model.

Table 1. Test and Computed Results of Local Buckling and Fracture of Tube Braces Under Cyclic Loads						
Test No.	RHS Specimen, mm	Local Buckling Time, s	Fracture Time, s	Fracture Strain	Boundaries and Reversal Loads	Reference
1	100×100×6	29.9 [29.7]	36.7 [36.2]	0.32	Semi-fixed, load 3	Han et al. (2006)
2	125×125×6	26.0 [25.7]	32.7 [32.7]	0.32	Semi-fixed, load 3	Han et al. (2006)
3	125×125×4.76	1.46 [1.68]	9.0 [8.99]	0.22	Semi-fixed, load 1	Lee et al. (1987)
4	125×125×4.76	1.56 [1.68]	10.8 [10.4]	0.22	Fixed, load 1	Lee et al. (1987)
5	100×100×6.35	13.8 [15.9]	21.0 [20.9]	0.14	Fixed, load 1	Lee et al. (1987)
6	100×100×6.35	10.0 [12.0]	16.7 [16.3]	0.14	Fixed, load 2	Lee et al. (1987)

LOCAL BUCKLING AND FRACTURE CRITERIA FOR BRACES

Nominal Strain of Local Buckling

Although fracture spreads across the entire section at complete failure, it starts at the flange opposite to the overall buckling direction (the "inner flange"), as shown in Figure 17. For convenience, the other flange of the RHS brace is called the "outer flange." Figures 17 and 18, respectively, illustrate the nominal strains at the inner side and outer side of the midspan cross section of a brace 100×100×6 of the test in Korea (test no. 1 in Table 1), which were calculated by the BCB element.

As plastic hinging due to bending moment was obviously experienced at the midspan of the brace, the second-order bending moment played a very important role due to *P-M* interaction and *P*-Δ effect. For the outer flange at the midspan, the compressive axial strain is overshadowed by the tensile strain caused by the bending moment when the brace is in compression. For the inner flange at the midspan, the compressive strain is deteriorated by the compressive axial strain caused by the bending moment. Consequently, the nominal deformation at the inner flange was more severe than that at the outer flange, as observed in the Korean test. Therefore, local buckling always starts with the inner flange.

Nominal strain of local buckling, ε_B, is defined as the strain of the inner flange fiber calculated by the BCB element through using the refined beam element model when local buckling occurs there. Local buckling can be detected in physical tests or numerical simulation using the partial shell element model, as shown in Figure 14. The greater the width-thickness ratio, the smaller the nominal strain of local

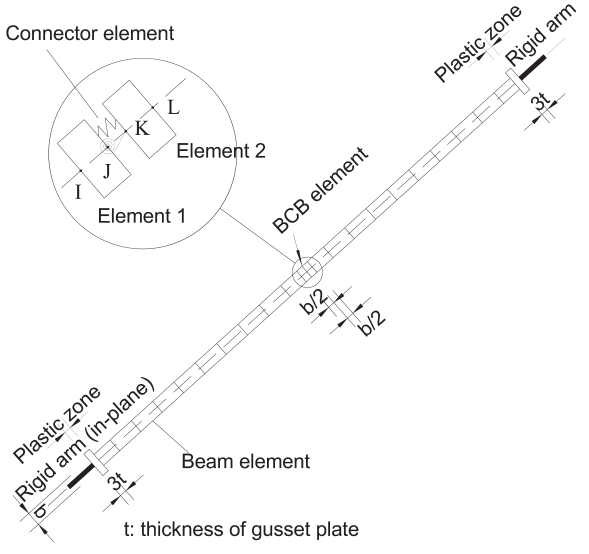

Fig. 16. Element dividing in refined beam element model of a brace.

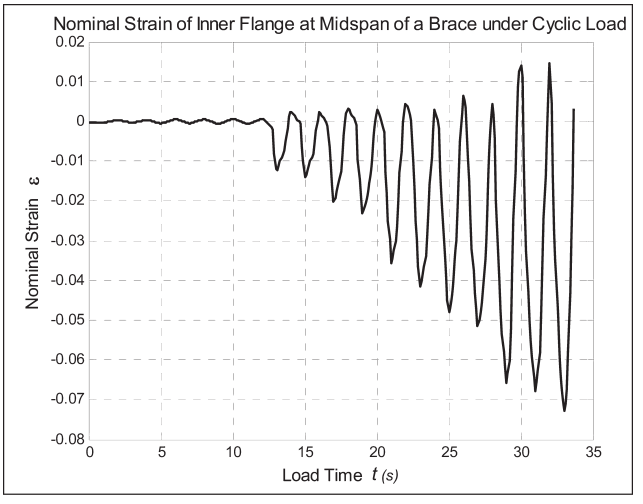

Fig. 17. Nominal strain of brace inner flange.

buckling would be (Figure 19). The local buckling criterion for a tube section can be obtained by regression analysis of the eight experimental results:

$$\varepsilon_B = 0.909/\lambda^{0.147} - 0.542 \quad (1)$$

where $\lambda = b/t$ and $5 \le \lambda \le 30$. The influence of overall buckling, which mainly depends on the slenderness ratio, *KL/r*, can be interpreted through the nominal strain at the midspan. Figure 20 shows that the slenderness ratio, *KL/r*, does not affect nominal strain criterion of local buckling at the midspan. Although the slenderness ratio affects *P-M* interaction at the midspan, which is already reflected in the (compressive) strain of the inner flange fiber at the midspan, how the strain/stress comes from the far ends to there does not influence the nominal strain criterion of local buckling according to Saint Venant's Principle.

In this way, local buckling of a brace can be easily discerned without using a fine mesh of shell elements.

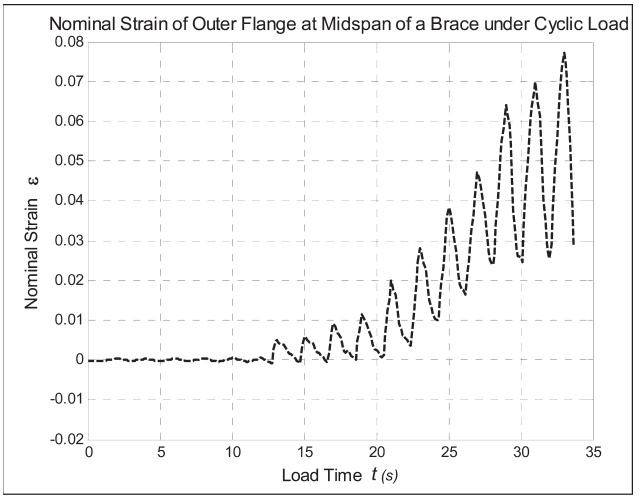

Fig. 18. Nominal strain of brace outer flange.

Strain-Based Fracture Criterion

Local buckling usually contributes to large concentrated deformation leading to fracture. Local buckling deformation causes the local bending moment at the inner flange and the webs, otherwise the stress and strain at the flanges and the webs should be nearly uniformly distributed along the thickness direction. In fact, upon local buckling, the excessive out-of-plane tube wall deformation and the corresponding stress are so dominant that the strain at the bulb increases very quickly and may reach 0.23 or greater (Figure 14) while local buckling becomes severe. Because the stiffness of the post-buckling inner flange is small, the axial stress has to be redistributed to the two nearby corners. Therefore, the fine transverse plastic wrinkles will form at the two corners, as shown in Figure 4. This is also the location where residual stress lies due to the forming process of the RHS section.

Mini cracks usually accompany the fine wrinkles. If the axial force changes to tension in the subsequent cyclic loading, the corners near the inner flange carry major tension even though the buckled inner flange beside the two corners may be pulled straight. As the axial force increases, those cracks develop and propagate. Finally, at the two corners, the cracks develop rapidly so that fracture inevitably occurs from the two corners to the whole cross section, as shown in Figure 3(d).

Low-cycle fatigue is a serious problem for braced structures subjected to earthquakes because seismic vibration of

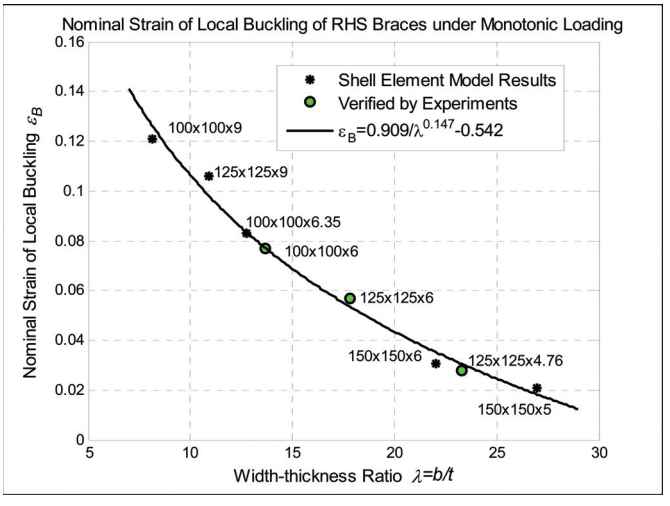

Fig. 19. Nominal strain of local buckling of tube braces with different width-thickness ratios.

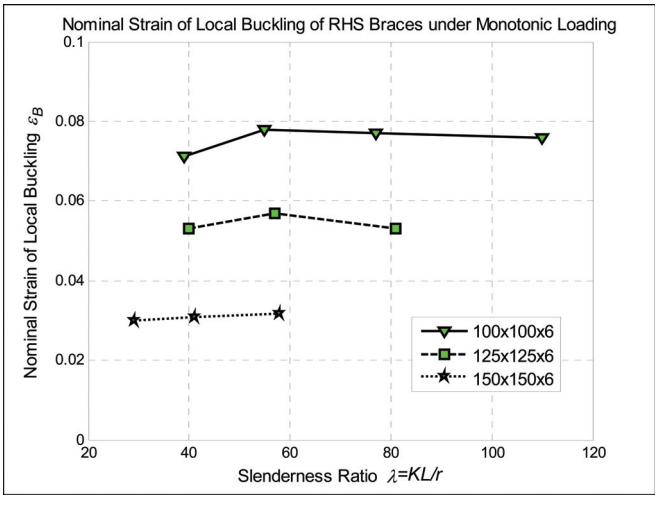

Fig. 20. Nominal strain of local buckling of tube braces with different slenderness ratios.

structures may cause considerable damage accumulation. How to determine damage accumulation of braces at the member level remains unclear. A strain-based damage criterion at the inner flanges of RHS braces is proposed later.

Major parameters influencing fracture life are brace slenderness ratio, section property, boundary condition, brace imperfections, material properties (such as Young's modulus, elongation rate, yielding strength, ultimate tensile strength), and width-thickness ratio. The first four factors and overall buckling have been reflected in the nominal strain of the inner flange. Material and geometrical information can be input in the modeling.

Fracture strain is a very important index of ductility. The true fracture strain, ε_f, is the true strain based on the original area, A_0, and the area after fracture, A_f (Ling, 1996), where

$$\varepsilon_f = \ln \frac{A_0}{A_f} \tag{2}$$

This parameter represents the maximum true strain that the material can withstand before fracture and is analogous to the ultimate uniaxial tensile strain ε_{cr} at the end of the engineering stress-strain curve. In structural engineering, ε_{cr} is equivalently taken as the fracture strain (Ling, 1996; Han et al., 2006). ε_{cr} can be determined by coupon tests of the ultimate strain at the necking location of a steel tensile specimen under monotonic uniaxial tensile loading. Generally, the fracture strain of structural steel varies from 0.05 for brittle steel to 0.70, or even greater, for ductile steel.

The damage/shear strain dependence for monotonic loading can be described by the power law (Lemaritre and Chaboche, 1975):

$$\omega = b\varepsilon^a \tag{3}$$

where ω is an index of damage accumulation; a, b are functions of stresses and temperature.

For undamaged material, $\omega = 0$. At fracture, when ε reaches ε_{cr}, $\omega = 1$, so $b = 1/\varepsilon_{cr}^a$. So for monotonic loading

$$\omega = \left(\frac{\varepsilon}{\varepsilon_{cr}}\right)^a \tag{4}$$

For non-monotonic loading

$$\omega = \sum_{i=1}^{N} \left(\frac{|\Delta\varepsilon_i|}{\varepsilon_{cr}}\right)^a \tag{5}$$

$$\Delta\varepsilon_i = \varepsilon_i - \varepsilon_{i-1} \tag{6}$$

where

ε_i = strain amplitude of cycle i

ε_{i-1} = strain amplitude of cycle i–1

Because local buckling brings large deformation and severe damage, local buckling should be detected first. We define $\Delta\varepsilon_{ic}$ as strain amplitude in compression cycles. Local buckling will happen for braces categorized in L mode or O-L mode if the local buckling index, BI, which evaluates initiation of local buckling, is equal to or greater than 1.0,

$$\text{BI} = \frac{|\Delta\varepsilon_{ic}|}{\phi_B \varepsilon_B} \tag{7}$$

where

ϕ_B = local buckling resistance factor for ε_B in order to consider plastic deformation accumulation due to previous cycles of non-monotonic loading before local buckling

ϕ_B can be derived as

$$\phi_B = 1 - \eta \sum_{i}^{L} \left(\frac{|\Delta\varepsilon_{ic}|}{\varepsilon_B}\right)^{\gamma_B} \tag{8}$$

where

L = number of loading cycles until local buckling occurs

η = parameter for computing the local buckling resistance factor

γ_B = parameter for computing the local buckling resistance factor

η and γ_B can be determined by regression analysis of test results of local buckling. It would be expected that ϕ_B is close to 1 for braces with large *b/t*, where local buckling is close to elastic buckling. For small *b/t* ratios, yielding will occur before buckling and inelastic buckling occurs. For monotonic loading, $\phi_B = 1$. The local buckling criterion $\phi_B \varepsilon_B$ is decreasing when a brace is under cyclic loading. Hence, it needs to be updated at each cycle.

The damage index, DI, which evaluates fracture life, is composed of two parts: one accounts for deformation before local buckling; the other is for damage accumulation after local buckling.

$$\text{DI} = \sum_{i=1}^{L-1} \left(\frac{|\Delta\varepsilon_i|}{\varepsilon_{cr}}\right)^{\alpha} + \sum_{i=L}^{N} \left(\frac{|\Delta\varepsilon_i|}{\varepsilon_{cr}}\right)^{\beta} \tag{9}$$

where

α = parameter for computing the damage index, which can be determined by regression analysis of experiment results

β = parameter for computing the damage index, which can be determined by regression analysis of experiment results

N = the number of loading cycles before fracture

For example, if the yield strength of a steel bar is 345 MPa (50 ksi), $|\Delta\sigma_i|$ = 220 MPa (31.9 ksi) [changes linearly between −110 MPa (−16 ksi) and 110 MPa (16 ksi)], $|\Delta\varepsilon_i| = |\Delta\sigma_i|/E$= 0.0011, ε_{cr} = 0.28, if α = 2 and no local buckling occurs, then the fracture cycles $N = (\varepsilon_{cr}/|\Delta\varepsilon_i|)^{\alpha}/2 = (0.28/0.0011)^2/2$ = 32,397.

A brace cannot fracture while the section fibers are fully in compression (Han et al., 2006). When the damage index, DI, of any fiber in the two beam elements of the BCB elements reaches 1.0, and the nominal stress of that fiber reaches the tensile yield stress, fracture will occur for a brace categorized in L mode or O-L mode.

In the subsequent discussion, the parameters in the preceding equations will be determined, and the method verified.

Application and Verification of the Modeling

The refined beam element model with the BCB elements has been completed and tested as follows. For verification, six specimens from two separate tests are considered, as shown in Table 1. Test 1 and test 2 have been described in this chapter; Tests 3 through 6 were completed by Lee and Goel (1987). Tests 1 through 3 are used to obtain values of the parameters η and γ_B, α and β in Equations 8 and 9 by the regression analysis on the buckling times, and the fracture times, respectively. These values are determined as η = 0.15, γ_B = 2.73, α = 2.73, and β = 1.47. The computed results of tests 4 through 6 are compared with the experimental results to justify these two parameters for regular building tube braces with *b/t* values from 15.7 to 26.3. The bracing length is 3250 mm (10 ft 8 in.).

For convenience, HSS5×5×3/16 and HSS4×4×1/4 in the Lee and Goel test are converted to 125×125×4.76 and 100×100×6.35, respectively. In Table 1 and Figures 21 through 26, load time does not mean the actual loading time. It represents one loading cycle per "2 seconds" in the load history description. In the table, the numbers in the brackets are the computed local buckling time or the computed fracture time.

Reversal load 3 is shown in Figure 2. Reversal load 1 and reversal load 2 were defined in the report by Lee and Goel (1987). The cyclic load histories are also shown in Figures 21 through 26. Figures 21a through 26a show when local buckling initiates, when fracture occurs, and how the damage index increases. Figures 21b through 26b show how the local buckling strain resistance factor decreases after a few cycles of the loads and the local buckling index approaches 1.0. Figures 21c through 26c show the nominal strain and the nominal stress (1 MPa = 0.145 ksi) at the inner flange in the two beam elements of BCB beside the cross section at the midspan. The difference between a fixed boundary condition and a semi-fixed one is that the fixed ones have the gusset plates stiffened to prevent hinging in the gusset plate and the semi-fixed ones do not.

Figures 21a, b and c show the results for a member with a low *b/t* ratio (13.6) and large fracture strain (0.32). Several large cycles of axial displacement are applied before local buckling occurs, and several more before fracture occurs. The axial deflection reaches 50 mm (1.97 in.) before fracture occurs. Note that ϕ_B becomes smaller with load cycles for this member with a small *b/t*. Figures 22a, b, and c show the results for a member with *b/t* = 17.8. For this case, the axial deflection reaches about 40 mm (1.57 in.), and the time to failure decreases because of the larger *b/t*. However, both of these specimens show excellent ductile behavior. Figure 23 series show the results for a member with *b/t* = 23.3 and fracture strain 0.22. For this case, local buckling occurs while $\phi_B \cong 10$. The ductility of the specimens in Tests 3 and 4 is not so good because of the larger *b/t* and lower fracture strain. Note that ϕ_B =1 until local buckling occurs in this member with large *b/t*. The same member size and loading pattern were used for the member response shown in Figure 24. The only difference is that the gusset plate is stiffened out of plane for the member shown in Figure 24 but not the one in Figure 23. The member in Figure 24 performed only slightly better than the one in Figure 23. In Figure 25a, the tested local buckling time occurs prior to the calculated local buckling time. The reason could be some large section imperfection or some deviation of material property. The Figures 25 and 26 series show the results for a member with *b/t* = 12.7 and fracture strain 0.14. Because of the low *b/t* value, several large cycles are required for local buckling to occur. The ductility, although reasonably good, is reduced because of the low value of fracture strain.

Figures 21a through 26a show that the portion of DI before local buckling is only about 5% to 20%. After local buckling, DI increases rapidly. It reveals that local buckling is the cause of brace fracture at the midspan.

The prediction of local buckling and fracture of braces is more than acceptable for analysis of building structures. Fracture predictions of the six brace specimens are very accurate and slightly conservative. Therefore, brace fracture modeling for steel braced frames is not only feasible but also applicable.

It should be noted that these computed results are consistently good even though the test loading sequence were different for the two testing programs. The tests by Han et al. (2006) used a symmetrical loading sequence with equal displacements in compression and tension, while the Lee and Goel (1987) tests used loadings where compressive displacements increased but the maximum tension ones were a small constant for each cycle. So, load 3 (Table 1) is potentially more damaging because of the large strain excursions applied in tension. Also, the specimens considered covered large ranges of width-thickness ratio and fracture strain.

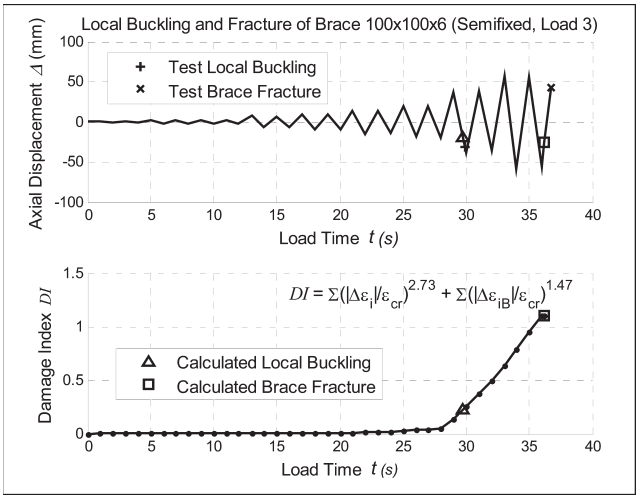

Fig. 21a. Local buckling and fracture of brace 100×100×6 semi-fixed under load 3.

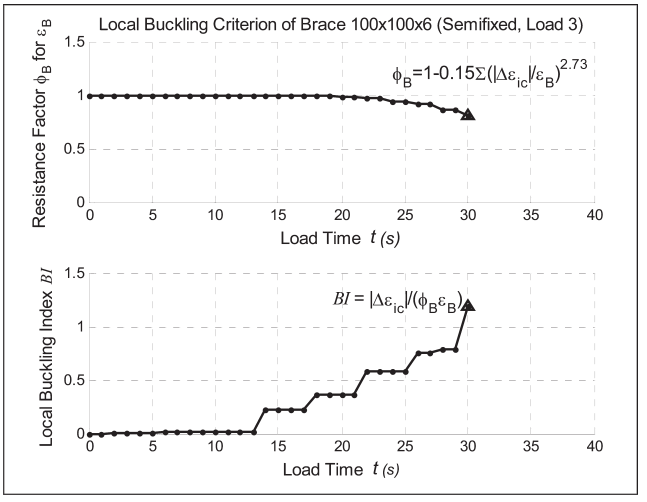

Fig. 21b. Local buckling index of brace 100×100×6 semi-fixed under load 3.

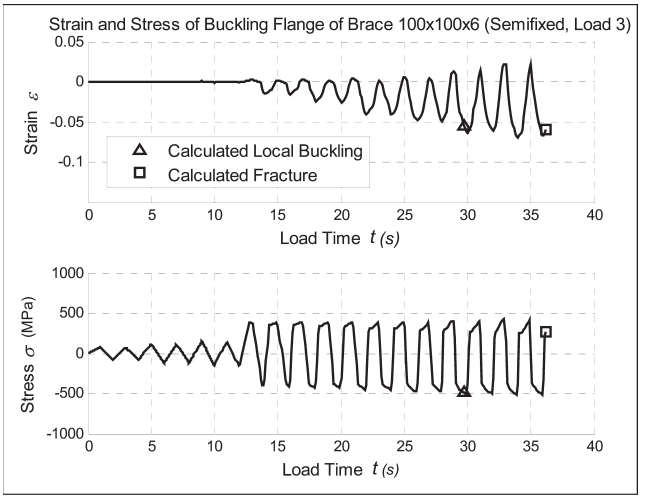

Fig. 21c. Nominal strain and stress of brace 100×100×6 semi-fixed under load 3.

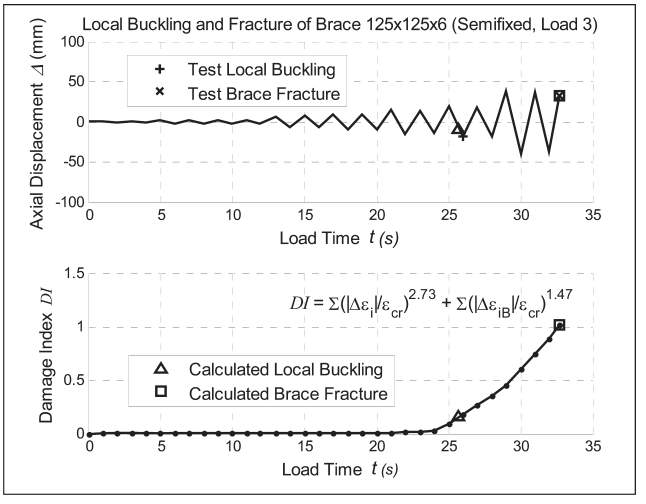

Fig. 22a. Local buckling and fracture of brace 125×125×6 semi-fixed under load 3.

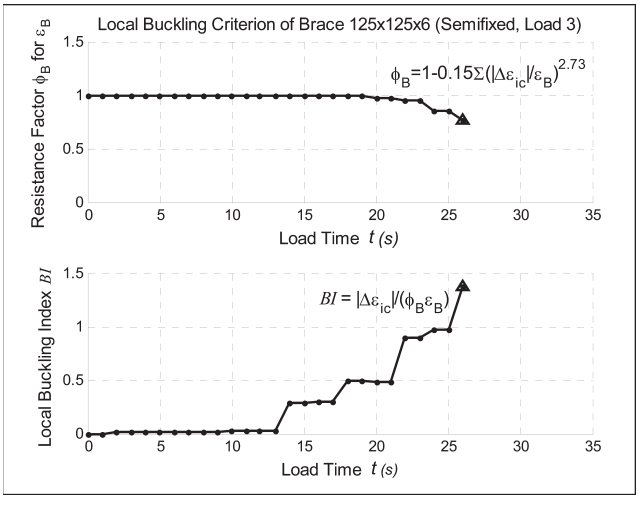

Fig. 22b. Local buckling index of brace 125×125×6 semi-fixed under load 3.

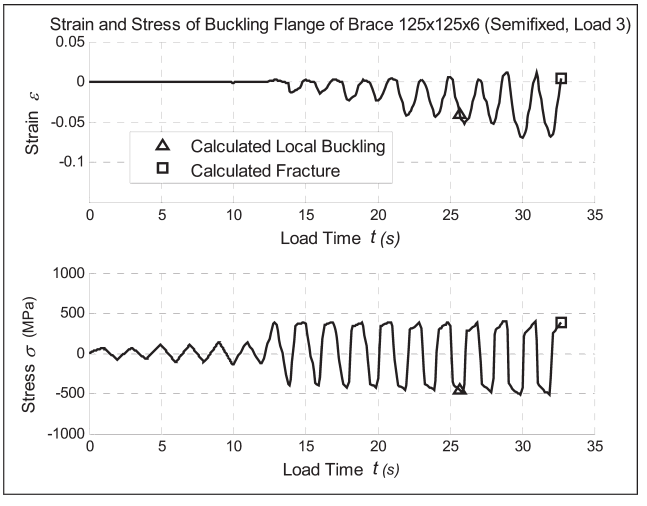

Fig. 22c. Nominal strain and stress of brace 125×125×6 semi-fixed under load 3.

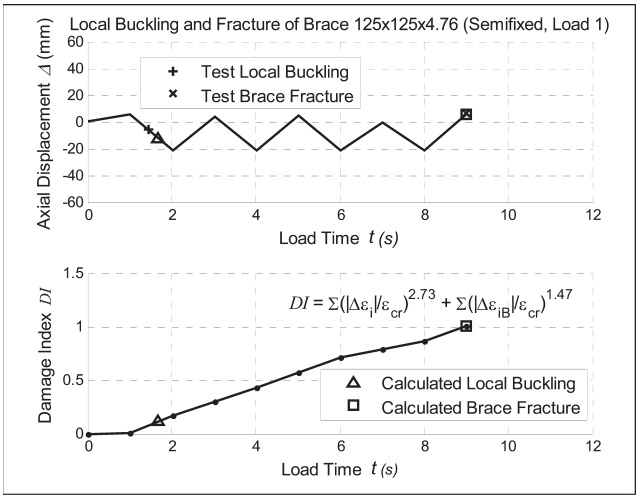

Fig. 23a. Local buckling and fracture of brace 125×125×4.76 semi-fixed under load 1.

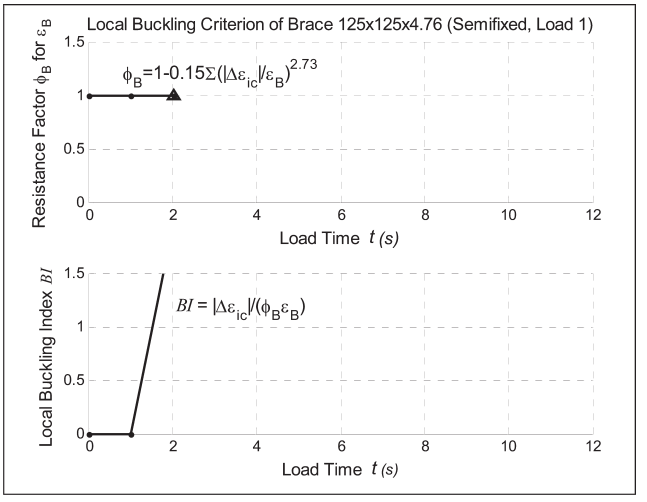

Fig. 23b. Local buckling index of brace 125×125×4.76 semi-fixed under load 1.

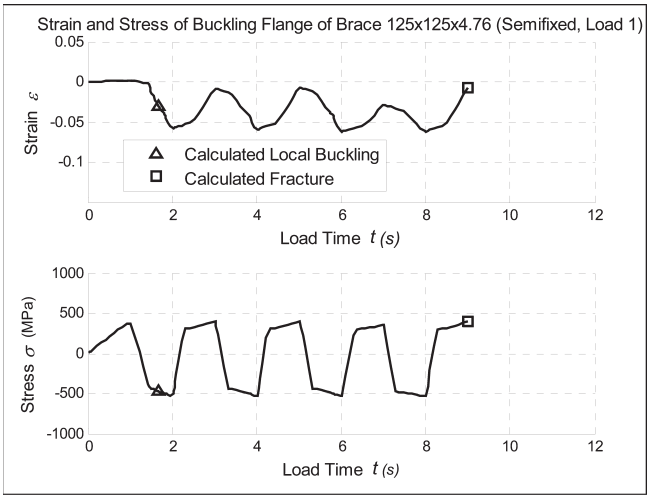

Fig. 23c. Nominal strain and stress of brace 125×125×4.76 semi-fixed under load 1.

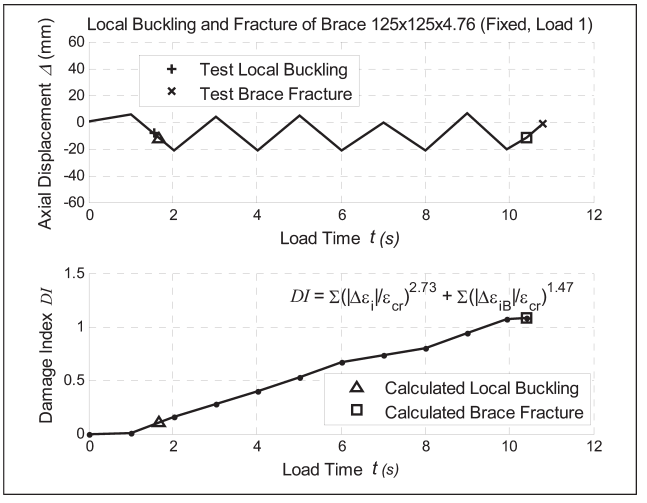

Fig. 24a. Local buckling and fracture of brace 125×125×4.76 fixed under load 1.

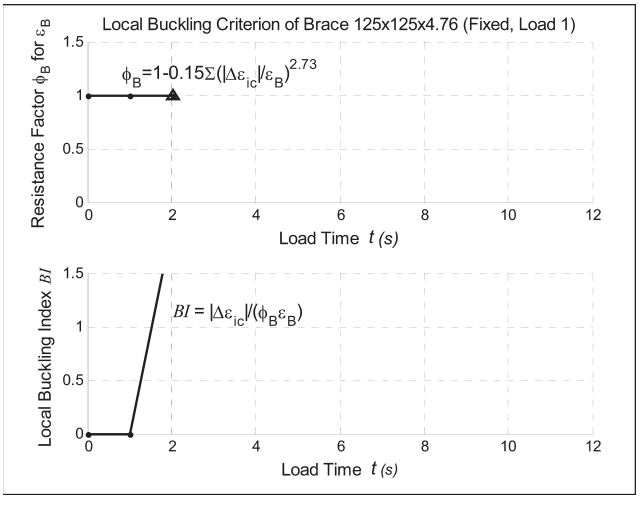

Fig. 24b. Local buckling index of brace 125×125×4.76 fixed under load 1.

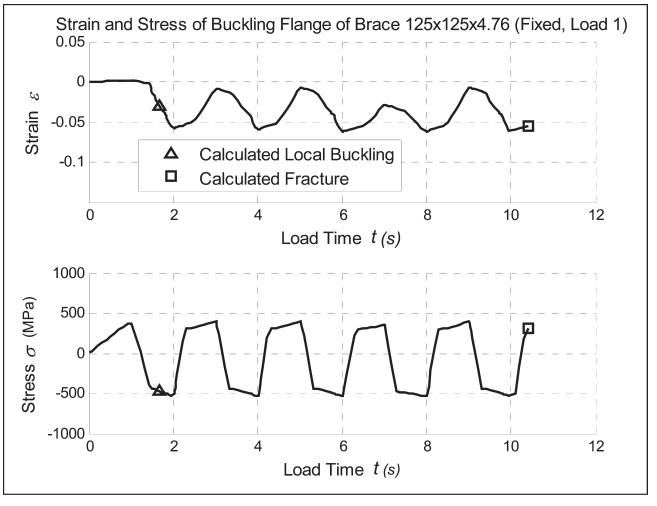

Fig. 24c. Nominal strain and stress of brace 125×125×4.76 fixed under load 1.

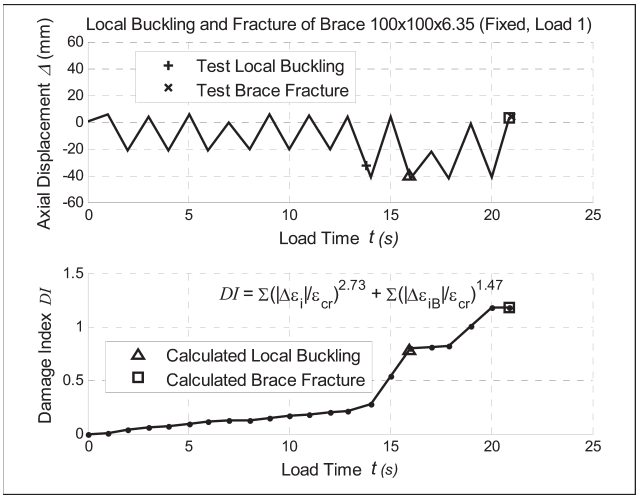

Fig. 25a. Local buckling and fracture of brace 100×100×6.35 fixed under load 1.

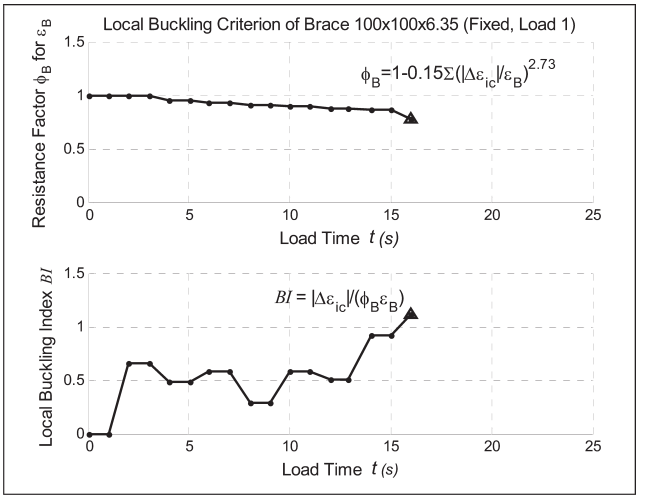

Fig. 25b. Local buckling criterion and index of brace 100×100×6.35 fixed under load 1.

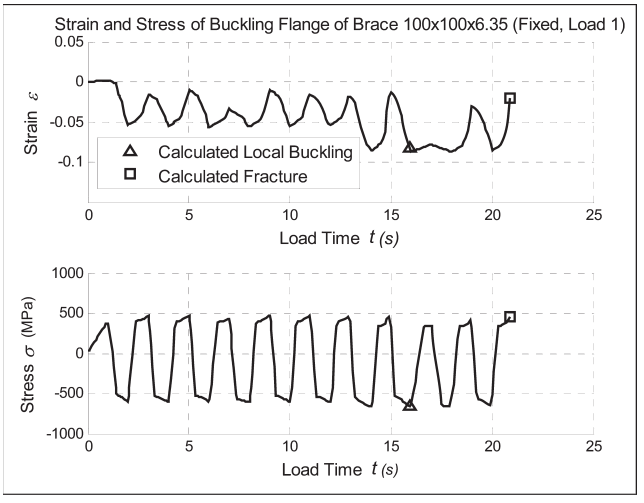

Fig. 25c. Nominal strain and stress of brace 100×100×6.35 semi-fixed under load 1.

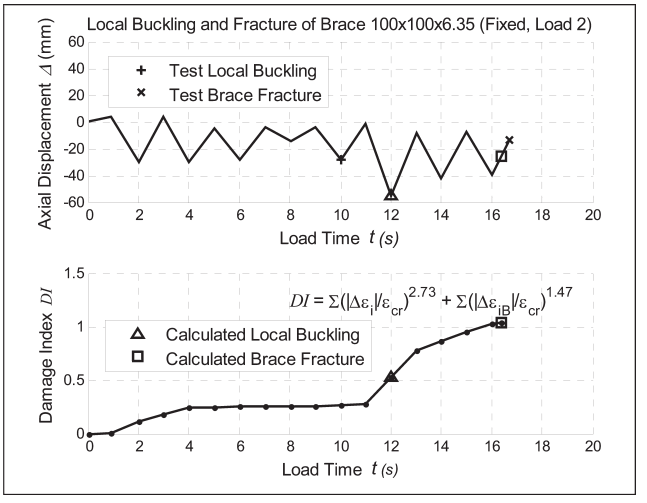

Fig. 26a. Local buckling and fracture of brace 100×100×6.35 fixed under load 2.

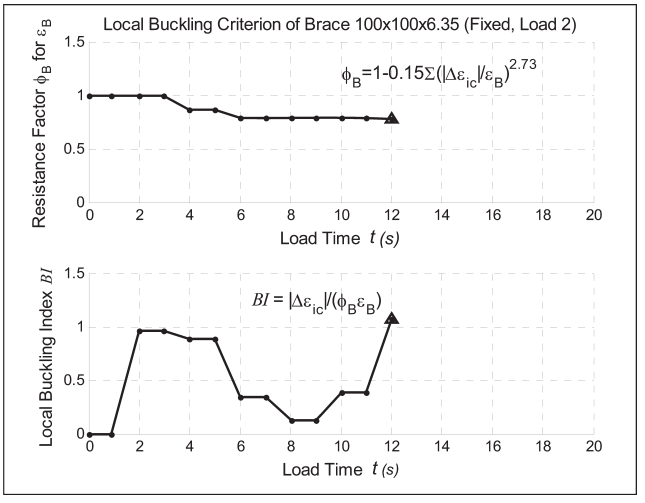

Fig. 26b. Local buckling criterion and index of brace 100×100×6.35 fixed under load 2.

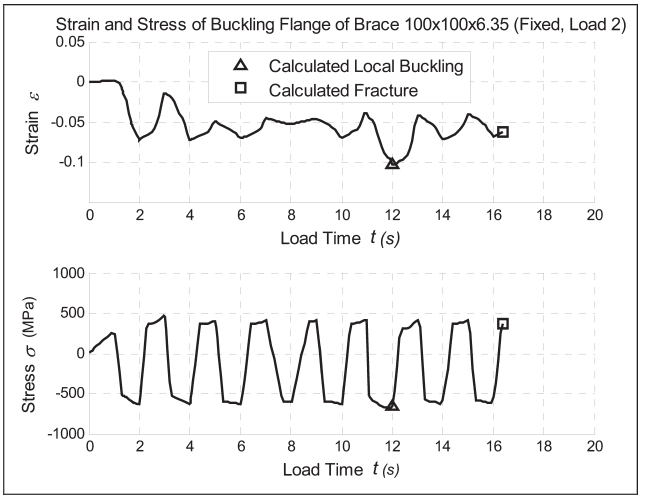

Fig. 26c. Nominal strain and stress of brace 100×100×6.35 fixed under load 2.

CONCLUSIONS

Nominal strain of RHS braces computed through using refined beam elements has been successfully applied to the prediction of local buckling and fracture of RHS braces. The brace tests and partial shell element model simulation also verified the prediction of local buckling by the nominal strain at the flanges. The damage index approach interprets damage accumulation by introducing nominal strain amplitude in a beam element. Comparison of prediction of brace local buckling and fracture using nominal strain and the test results shows good agreement. Thus, brace fracture in structural systems can be investigated efficiently and accurately by using the refined beam element model.

ACKNOWLEDGMENT

This research was supported by grant CMS 02-18703 from the National Science Foundation. This support is gratefully acknowledged.

REFERENCES

Abaqus (2004), "Abaqus Version 6.5 Documentation."

AISC (2005a), *Specification for Structural Steel Buildings*, American Institute of Steel Construction, Chicago, IL.

AISC (2005b), *Seismic Provisions for Structural Steel Buildings*, American Institute of Steel Construction, Chicago, IL.

AISC (2005c), *Steel Construction Manual*, 13th ed., American Institute of Steel Construction, Chicago, IL.

Ding, X. and Foutch, D.A. (2006), "Redundancy in Steel Braced Frames under Seismic Excitations," SRS. No. 640, Department of Civil and Environmental Engineering, University of Illinois at Urbana-Champaign, Urbana, IL, June.

Goel, S.C. and El-Tayem A.A. (1986), "Cyclic Load Behavior of Angle X-Bracing," *Journal of Structural Engineering*, Vol. 112, No. 11, pp. 342–361.

Gu, J.X. and Chan, S.L. (2004), "Second-Order Analysis and Design of Steel Structures Allowing for Member and Frame Imperfections," *International Journal for Numerical Methods in Engineering*, Vol. 62, No. 5, pp. 601–615.

Gugerli, H. and Goel, S.C. (1984), "Inelastic Cyclic Behavior of Steel Bracing Members," Report No. UMEE 82R1, Department of Civil Engineering, University of Michigan, Ann Arbor, MI.

Han, S-W, Wook, T-K and Foutch, D.A. (2006). "Experimental Study of HSS Braces under Cyclic Loads," SRS No. 641, Department of Civil and Environmental Engineering, University of Illinois at Urbana-Champaign, Urbana, IL.

Ikeda, K. and Mahin, S. A. (1986), "Cyclic Response of Steel Braces," *Journal of Structural Engineering*, Vol. 112, No. 5, pp. 342–361.

Jain, A.K., Goel, S.C. and Hanson, R.D. (1978), "Inelastic Response of Restrained Steel Tubes," *Journal of Structural Engineering,* Vol. 104, No. 6, pp. 897–910.

Kahn, L.F. and Hanson, R.D. (1976), "Inelastic Cycles of Axially Loaded Steel Members," *Journal of Structural Engineering*, Vol. 102, No. 5, pp. 947–959.

Lapovok, R., Smirnov, S. and Shveykin, V. (2000), "Damage Mechanics for Fracture Prediction of Metal Forming Tools," *International Journal of Fractures*, Vol. 103, No. 2, pp. 111–126.

Lee, S. and Goel, S.C. (1987), "Seismic Behavior of Hollow and Concrete-Filled Square Tubular Bracing Members," Research Report No. UMCE 87-11, University of Michigan, Ann Arbor, MI.

Liu, Z. (1987), "Investigation of Concrete-Filled Steel Tubes under Cyclic Bending and Buckling," PhD Thesis, University of Michigan, Ann Arbor, MI.

Popov, E.P. and Black, R.G. (1981), "Steel Struts under Cyclic Loadings," *Journal of Structural Engineering*, Vol. 107, No. 9, pp. 1857–1881.

Remennikov, A.M. and Walpole W.R. (1997), "Analytical Prediction of Seismic Behavior for Concentrically-Braced Steel Systems," *Earthquake Engineering and Structural Dynamics*, Vol. 26, No. 8, pp. 859–874.

Venson, A. and Voyiadjis, G. (2001), "Damage Quantification in Metal Matrix Composites," *Journal of Engineering Mechanics*, Vol. 127, No. 3, pp. 291–298.

Design Aid for Triangular Bracket Plates Using AISC Specifications

SHILAK SHAKYA and SRIRAMULU VINNAKOTA

A typical triangular bracket plate rigidly supported on the shorter sides and free on the longer side is shown in Figures 1a and 1b. Such triangular gusset plates are found in base plate to column connections (Figure 1c), stiffened seated connections (Figure 1d), and bracket to column connections. The behavior of such bracket plates under an applied load has been provided by Salmon (1962) and Tall (1964).

Bracket plates are normally designed using either the elastic strength method (Salmon, 1962) or the plastic strength method (Tall, 1964). The elastic method of design is based on the assumption that the centroid of applied load is at approximately 0.6 times the length of the loaded side of the bracket plate from the 90° corner (i.e., $s \approx 0.6b$ in Figure 1a). The plastic strength method assumes that the plastic strength develops on a section normal to the free edge and passing through the 90° corner at point *o* (Figure 1a). The relations in the elastic method do not include the variable distance, *s* (position of the load), while the plastic strength method does. The laboratory tests (Salmon, Beuttner and O'Sheridan, 1964) showed that yielding of the free edge occurs prior to buckling.

The method presented in this paper is an adoption of the method presented by Martin and Robinson (1982), developed in the United Kingdom, with the incorporation of relations for compressive stresses from the AISC *Specification for Structural Steel Buildings,* hereafter referred to as the AISC *Specification* (AISC, 2005a). This method assumes that failure of the plate occurs by flexural buckling of the plate. Therefore, both elastic and inelastic compressive strength relations for buckling given in the AISC *Specification* are included to arrive at the strength of the bracket plate.

Shilak Shakya is a structural engineer, Arnold and O'Sheridan, Brookfield, WI.

Sriramulu Vinnakota is professor of civil engineering, Marquette University, Milwaukee, WI.

The task of the designers of a bracket plate is to find the thickness, *t*, of the plate (Figure 1b) based on the known values of plate aspect ratio, *a*/*b*, position of load, *s*, design load (required strength, P_u or P_a), and steel properties (e.g., modulus of elasticity, *E*, and yield stress, F_y). The derivation of design relations is given in the next section.

DERIVATION OF DESIGN RELATIONS

The bracket plate, with an elemental strut of width *dz* parallel to the free edge and length l_z, is shown in Figure 2a. The end conditions for this strut are assumed to be fixed-fixed. The stress distribution across *B* is shown in Figure 2b. The effective slenderness ratio (Kl_z/r) for this strut in terms of plate geometry parameters can be written as

$$\frac{Kl_z}{r} = \sqrt{12}K\left(\frac{a}{b} + \frac{1}{a/b}\right)\frac{z}{t} \tag{1}$$

where

K = effective length factor
a = height of the supporting edge
b = length of the loaded edge
dz = width of the elemental strut
t = thickness of the elemental strut/bracket plate
l_z = unsupported length of the elemental strut at distance z from o

$$= \left(\frac{a}{b} + \frac{1}{a/b}\right)z \tag{2}$$

r = radius of gyration of the elemental strut

$$= \sqrt{\frac{I}{A}} = \sqrt{\frac{dz\,t^3}{12\,dz\,t}} = \frac{t}{\sqrt{12}} \tag{3}$$

The normal distance *B* from the inside corner to the free edge of the plate can be expressed in terms of plate geometry parameter as

$$B = \frac{a}{\sqrt{1+\left(\frac{a}{b}\right)^2}} \tag{4}$$

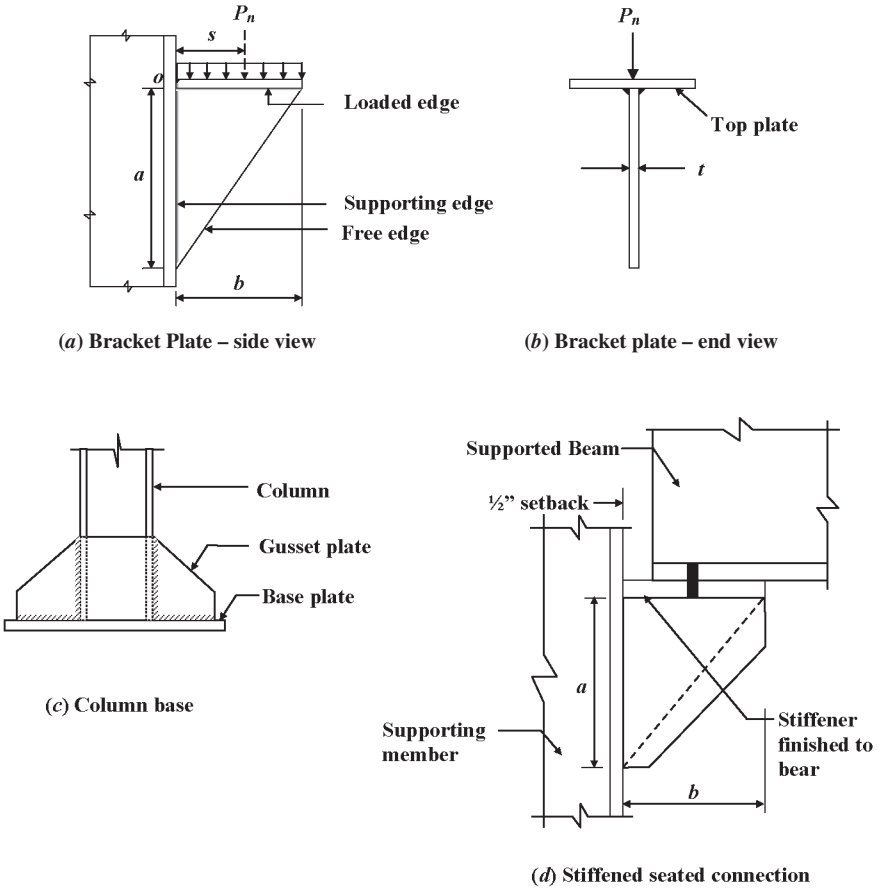

Fig. 1. Triangular bracket plates.

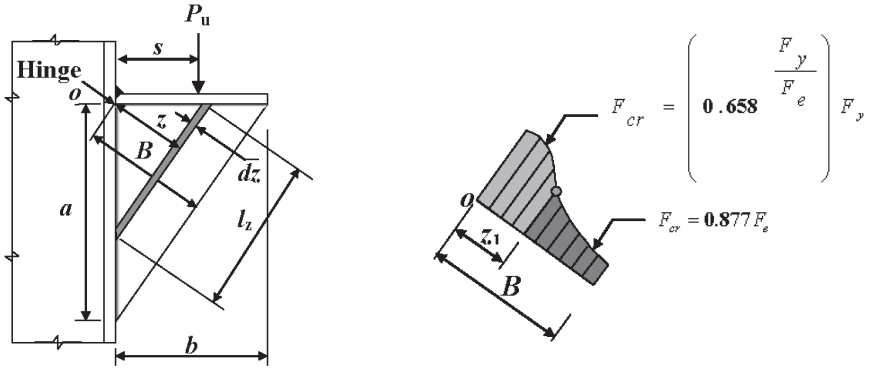

(a) Element strut (b) Stress distribution along *B*

Fig. 2. Triangular bracket plate with an elemental strut.

Table 1. Limiting Values of t^*/b							
F_y (ksi)	0.5	0.75	1.0	1.5	2.0	2.5	3.0
36	0.0188	0.0210	0.0238	0.0303	0.0376	0.0453	0.0532
50	0.0222	0.0248	0.0281	0.0358	0.0444	0.0534	0.0627

The expressions for the critical stress, F_{cr}, given in the AISC *Specification* (Equations E3-2 and E3-3) are

For $\frac{Kl_z}{r} \le 4.71\sqrt{\frac{E}{F_y}}$

$$F_{cr} = \left(0.658^{\frac{F_y}{F_e}}\right)F_y \tag{5}$$

For $\frac{Kl_z}{r} > 4.71\sqrt{\frac{E}{F_y}}$

$$F_{cr} = 0.877F_e \tag{6}$$

where

F_e = elastic critical buckling stress

$$= \frac{\pi^2 E}{\left(\frac{Kl_z}{r}\right)^2} \tag{7}$$

Substituting Equation 7 into Equations 5 and 6 and simplifying, we can rewrite Equations 5 and 6

For $\lambda_c \le 1.5$

$$F_{cr} = \left(0.658^{\lambda_c^2}\right)F_y \tag{8}$$

For $\lambda_c > 1.5$

$$F_{cr} = \left(\frac{0.877}{\lambda_c^2}\right)F_y \tag{9}$$

where

$$\lambda_c = \frac{Kl_z}{r\pi}\sqrt{\frac{F_y}{E}} \tag{10}$$

Using Equation 1, Equation 10 for the elemental strut at distance z from point o (see Figure 2a) can be expressed as

$$\lambda_{cz} = \alpha z \tag{11}$$

where

$$\alpha = \frac{2\sqrt{3}K}{\pi}\sqrt{\frac{F_y}{E}}\left(\frac{a}{b} + \frac{1}{a/b}\right)\frac{1}{t} \tag{12}$$

The experimental work (Martin, 1979; Martin and Robinson, 1982) showed that the stress in the strip at the 90° corner is at yield and the stress in the strip near the free edge depends on the slenderness ratio of the strip at the free edge. Therefore, it is necessary to determine the boundary of the two regions where inelastic buckling and elastic buckling control the critical compressive stress of the strip. The location of this boundary denoted by z_1 (measured from the inside 90° corner) can be determined from Equation 8 with the help of Equations 9 and 10 and is given here:

$$z_1 = \frac{3}{2\alpha} = \frac{\sqrt{3}}{4}\frac{\pi}{K}\sqrt{\frac{E}{F_y}}\left[\frac{a/b}{1+\left(a/b\right)^2}\right]t \tag{13}$$

This relation may be written in a dimensionless form by scaling with Equation 4 and simplifying. Thus, we have

$$\frac{z_1}{B} = \frac{\sqrt{3}}{4}\frac{\pi}{K}\sqrt{\frac{E}{F_y}}\left[\frac{t/b}{\sqrt{1+\left(a/b\right)^2}}\right] \tag{14}$$

Note that a value of $z_1/B > 1$ from Equation 14 indicates that all the strips fail by inelastic buckling. Substituting this condition into Equation 14 results

$$\frac{t^*}{b} = \frac{4}{\sqrt{3}}\frac{K}{p}\sqrt{\frac{F_y}{E}}\sqrt{1+\left(\frac{a}{b}\right)^2} \tag{15}$$

The limiting values of t^*/b for different values of a/b and F_y/E are presented in Table 1.

Note that if the actual value of t/b is less than the limiting value given in Table 1 for given a/b and F_y, the strength relation (see Equation 19) will have contributions of both inelastic and elastic buckling stresses.

The nominal compressive strength based on the limit state of flexural buckling for a compression member is given by

$$P_n = A_g F_{cr} \tag{16}$$

where

A_g = gross area of member

The relationships of the required strengths (P_u or P_a) to the nominal load, P_n, from the AISC *Specification* (AISC, 2005a) may be written as

$$P_u = \phi_c P_n \tag{17a}$$

$$P_a = \frac{P_n}{\Omega_c} \tag{17b}$$

where

ϕ_c = 0.90 for load and resistance factor design (LRFD)

Ω_c = 1.67 for allowable stress design (ASD)

The 90° corner of the plate is assumed to act as a hinge. The strut near the 90° corner could attain yield stress while the stresses in the farther struts depend on the slenderness ratio of the strut. See Figure 2b for the distribution of critical compressive stress. Equating sum of the moments of all elemental struts due to compressive forces about the hinge at point *o* to the external moment due to the externally applied load, we have

$$P_n\, s = \int_0^B F_{cr}\,(t\,dz)\; z \tag{18}$$

Restoring Equations 8 and 9 for F_{cr} and with the limits as shown in Figures 2b, Equation 18 can be expressed as

$$P_n\, s = tF_y \left[\int_0^{z_1} 0.658^{\lambda_{cz}^2} z\, dz + 0.877 \int_{z_1}^{B} \frac{z dz}{\lambda_{cz}^2} \right] \tag{19}$$

After integrating, simplifying and making Equation 19 dimensionless by scaling both sides with (b^3E), we obtain

$$\frac{P_n s}{b^3 E} = \frac{\pi^2}{12K^2} \frac{\left(a/b\right)^2}{\left[1+\left(a/b\right)^2\right]^2} \left(\frac{t}{b}\right)^3 \times \left[0.72877 + 0.877 \log_e \left(\frac{B}{z_1}\right) \right] \tag{20}$$

The details of integration are shown in Appendix A. Note that $\frac{B}{z_1} > 1$ in the preceding equation.

Making use of Equation 14 in Equation 20 yields

$$\frac{P_n s}{b^3 E} = \frac{\pi^2}{12K^2} \frac{\left(a/b\right)^2}{\left[1+\left(a/b\right)^2\right]^2} \left(\frac{t}{b}\right)^3 \times \left\{ 0.72877 + 0.877 \log_e \left[\frac{4}{\sqrt{3}} \frac{K}{\pi} \sqrt{\frac{F_y}{E}} \sqrt{1+\left(\frac{a}{b}\right)^2} \frac{1}{t/b} \right] \right\} \tag{21}$$

Knowing the applied load, the plate geometry, and the material properties, Equation 21 can be solved for *t*/*b* by trial and error or a simple computer program may be used to solve numerically.

When $\frac{B}{z_1} > 1$, the compressive stress is controlled by inelastic buckling in all strips and elastic buckling does not occur. For this case, Equation 18 after integration with the upper limit as *B* and simplification results in

$$\frac{P_n s}{b^3 E} = \frac{\pi^2}{12K^2} \frac{\left(a/b\right)^2}{\left[1+\left(a/b\right)^2\right]^2} \left(\frac{t}{b}\right)^3 \times \left[\frac{0.658^{\left(\frac{12K^2 F_y [1+(a/b)^2]}{\pi^2 E (t/b)^2} \right)} - 1}{2 \log_e 0.658} \right] \tag{22}$$

COMPARISON TO EXPERIMENTAL AND THEORETICAL RESULTS

Equations 21 and 22 are used to compute the nominal strengths, P_n, and are compared with the experimental and theoretical results, P_{expt}, (Salmon, Buettner and O'Sheridan, 1964; Martin, 1979; Martin and Robinson, 1982). This comparison is shown in Tables 2a, 2b and 2c in terms of $P_{expt.}/P_n$. Note that the value of effective length factor, *K*, is taken equal to 0.5 in these calculations for comparison with other theoretical results. Also, the values of yield stresses in Tables 2a, 2b, and 2c are the measured values. The comparison shows that the authors' developed relations predict nominal load closer to the experimental results than the other theoretical methods.

Table 2a. Comparison with Experimental Results of Salmon et al. (1964) (E = 29,000 ksi)									
Specimen No.	b in.	a in.	t in.	s in.	F_y ksi	$P_{expt.}$ kips	$P_{expt.}/P_n$		
							Salmon et al. (1964)	Martin (1979)	Authors
1	9.0	12.0	0.386	5.4	43.2	97.8	1.87	1.56	1.41
2	22.5	30.0	0.277	13.5	41.2	63.3	1.58	1.56	1.43
3	22.5	30.0	0.384	13.5	43.2	125.8	1.18	1.54	1.34
4	9.0	9.0	0.268	5.4	41.2	40.0	1.91	1.37	1.18
5	9.0	9.0	0.378	5.4	43.2	69.5	2.25	1.40	1.26
6	30.0	30.0	0.268	18.0	41.2	49.5	2.19	1.54	1.37
7	30.0	30.0	0.385	18.0	43.2	101.7	1.52	1.41	1.20
8	13.5	9.0	0.271	8.1	41.2	31.3	2.00	1.26	1.10
9	13.5	9.0	0.374	8.1	43.2	64.5	2.85	1.52	1.37
10	30.0	20.0	0.276	18.0	41.2	35.8	1.60	1.27	1.21
11	30.0	20.0	0.384	18.0	43.2	80.1	1.55	1.42	1.28
12	18.0	9.0	0.274	10.8	41.2	29.8	2.10	1.42	1.38
13	18.0	9.0	0.387	10.8	43.2	46.6	2.21	1.25	1.19
14	30.0	15.0	0.373	18.0	43.2	57.6	1.70	1.37	1.39
15	30.0	15.0	0.373	18.0	43.2	58.5	1.73	1.39	1.41

Table 2b. Comparison with Experimental Results of Martin (1979) (E = 29,877 ksi)									
Specimen No.	b in.	a in.	t in.	s in.	F_y ksi	$P_{expt.}$ kips	$P_{expt.}/P_n$		
							Salmon et al. (1964)	Martin (1979)	Authors
1	5.71	5.71	0.240	3.15	43.9	28.7	2.27	1.31	1.17
2	5.83	11.61	0.257	4.02	37.4	42.6	1.32	1.69	1.59
3	5.94	11.77	0.255	4.06	37.4	43.7	1.32	1.52	1.62
4	4.92	4.92	0.254	2.52	37.0	30.2	3.11	1.52	1.42
5	4.92	4.92	0.254	2.52	37.0	35.8	3.68	1.80	1.68
6	4.80	14.84	0.253	2.56	37.0	39.6	1.10	1.28	1.38
7	4.72	14.65	0.254	2.46	37.0	47.9	1.34	1.52	1.64

DESIGN AID TABLES

In design problems, the values of E, F_y, a, b, $\phi_c P_n$ (= required strength, P_u in LRFD) or P_n/Ω_c (= required strength, P_a in ASD), and s are known and the thickness, t, of the plate is to be determined. Therefore, design tables would become very helpful in the design process. Two design aids in tabular form, namely, Tables 3 and 4 are presented for steel with F_y = 36 ksi and 50 ksi, respectively. The plate aspect ratio, a/b, ranges from 0.50 to 3.00 and the dimensionless moment, $P_n\, s/b^3E$, varies from 0.25×10^{-6} to 50×10^{-6} in these tables. Knowing the design load, the design procedure is straightforward and the various steps are enumerated as follows:

1. Compute a/b, the nominal load, and $P_n\, s/b^3E$ from the known design information.

2. Determine t/b from Table 3 or 4, depending on the steel grade.

Table 2c. Comparison with Experimental Results of Martin and Robinson (1984) (E = 29,877 ksi)							
Specimen No.	b in.	a in.	t in.	s in.	F_y ksi	$P_{expt.}$ kips	$P_{expt.}/P_n$ Authors
1	3.94	3.94	0.157	1.97	54.8	14.7	1.00
2	7.87	7.87	0.157	3.94	54.8	19.8	0.99
3	7.87	7.87	0.157	3.94	54.8	21.3	1.07
4	11.81	11.81	0.157	5.91	54.8	17.7	0.93
5	15.75	15.75	0.157	7.88	54.8	15.0	0.87
6	15.75	15.75	0.157	7.88	54.8	15.6	0.90
7	19.69	19.69	0.157	9.85	54.8	17.5	1.11
8	19.69	19.69	0.157	9.85	54.8	18.0	1.14
9	7.87	1.97	0.157	3.94	54.8	4.9	1.66
10	7.87	3.94	0.157	3.94	54.8	12.3	1.28
11	7.87	3.94	0.157	3.94	54.8	13.0	1.36
12	7.87	5.91	0.157	3.94	54.8	19.0	1.19
13	7.87	7.87	0.157	3.94	54.8	19.5	0.98
14	7.87	7.87	0.157	3.94	54.8	20.7	1.04
15	7.87	9.84	0.157	3.94	54.8	24.1	1.12
16	7.87	9.84	0.157	3.94	54.8	27.0	1.26
17	7.87	11.81	0.157	3.94	54.8	24.6	1.15
18	7.87	11.81	0.157	3.94	54.8	27.3	1.28
19	7.87	15.75	0.157	3.94	54.8	24.6	1.30
20	7.87	15.75	0.157	3.94	54.8	25.0	1.32
21	7.87	19.69	0.157	3.94	54.8	26.4	1.65
22	7.87	19.69	0.157	3.94	54.8	27.0	1.69
23	7.87	23.62	0.157	3.94	54.8	23.4	1.76
24	7.87	23.62	0.157	3.94	54.8	26.4	1.98

EXAMPLES

For comparative purposes, the following two examples (Salmon and Johnson, 1990; Tall, 1974) are reworked.

Example 1

Determine the thickness required for a triangular bracket plate shown in Figure 3 to carry a factored load of 60 kips. Assume the load is located 15 in. from the face of support. Use the LRFD method with F_y = 36 ksi.

Solution

$a/b = 20/25 = 0.8$

$P_n = P_u/\phi_c = 60/0.9 = 66.7$ kips

$P_n\, s/b^3E = (66.7)(15)/[(25^3)(29{,}000)] = 2.208 \times 10^{-6}$

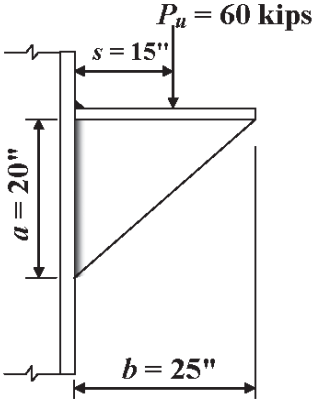

Fig. 3. Triangular bracket plate for Example 1.

Table 3. Nominal Strength of Triangular Bracket Plates Using AISC Column Strength Equations (F_y = 36 ksi, K = 0.65)							
$P_n s/b^3 E$ ($\times 10^{-6}$)	Values of t/b ($\times 10^{-3}$) for a/b equal to						
	0.50	0.75	1.00	1.50	2.00	2.50	3.00
0.25	8.06	6.78	6.41	6.54	7.06	7.69	8.35
0.50	10.93	9.07	8.52	8.65	9.31	10.12	10.98
0.75	13.16	10.79	10.09	10.20	10.95	11.89	12.89
1.00	15.11	12.24	11.40	11.47	12.30	13.35	14.46
2.00	22.12	16.89	15.46	15.36	16.36	17.69	19.12
4.00	36.37	24.67	21.60	20.89	22.03	23.68	25.50
6.00	51.37	32.47	27.14	25.36	26.47	28.30	30.37
8.00	66.81	40.50	32.71	29.44	30.35	32.28	34.52
10.00	82.47	48.75	38.38	33.43	33.96	35.90	38.26
12.00	98.27	57.16	44.17	37.43	37.44	39.29	41.72
14.00	114.10	65.69	50.06	41.46	40.90	42.56	45.01
16.00	130.10	74.30	56.03	45.54	44.36	45.78	48.18
18.00	146.10	82.98	62.08	49.66	47.83	48.99	51.28
20.00	162.10	91.70	68.19	53.83	51.32	52.19	54.36
22.00	178.10	100.50	74.34	58.05	54.84	55.41	57.43
24.00	194.10	109.20	80.53	62.30	58.39	58.64	60.50
26.00	210.20	118.10	86.76	66.60	61.97	61.88	63.57
28.00	226.20	126.90	93.01	70.92	65.57	65.15	66.66
30.00	242.30	135.70	99.28	75.28	69.21	68.43	69.76
32.00	258.30	144.60	105.60	79.66	72.87	71.74	72.87
34.00	274.40	153.50	111.90	84.06	76.55	75.06	75.99
36.00	290.50	162.30	118.20	88.49	80.25	78.41	79.14
38.00	306.60	171.20	124.50	92.93	83.98	81.77	82.29
40.00	322.70	180.10	130.90	97.39	87.73	85.16	85.47
42.00	338.70	189.00	137.20	101.90	91.49	88.56	88.66
44.00	354.80	197.90	143.60	106.30	95.27	91.98	91.86
46.00	370.90	206.80	150.00	110.80	99.06	95.41	95.08
48.00	387.00	215.70	156.30	115.40	102.90	98.86	98.32
50.00	403.10	224.60	162.70	119.90	106.70	102.30	101.60

Table 4. Nominal Strength of Triangular Bracket Plates Using AISC Column Strength Equations (F_y = 50 ksi, K = 0.65)							
$P_n s/b^3 E$ ($\times 10^{-6}$)	Values of t/b ($\times 10^{-3}$) for a/b equal to						
	0.50	0.75	1.00	1.50	2.00	2.50	3.00
0.25	7.76	6.57	6.22	6.37	6.89	7.51	8.17
0.50	10.42	8.73	8.24	8.40	9.05	9.86	10.71
0.75	12.44	10.33	9.72	9.87	10.63	11.56	12.55
1.00	14.15	11.67	10.94	11.08	11.91	12.95	14.05
2.00	19.74	15.81	14.66	14.71	15.75	17.07	18.48
4.00	29.74	22.03	20.00	19.75	21.00	22.67	24.47
6.00	40.02	27.58	24.35	23.66	25.00	26.90	28.97
8.00	50.66	33.14	28.37	27.05	28.40	30.46	32.75
10.00	61.56	38.79	32.35	30.16	31.46	33.64	36.09
12.00	72.65	44.55	36.35	33.12	34.30	36.54	39.13
14.00	83.85	50.42	40.39	36.01	36.98	39.26	41.95
16.00	95.14	56.37	44.49	38.88	39.56	41.85	44.62
18.00	106.50	62.39	48.63	41.76	42.09	44.33	47.16
20.00	117.90	68.48	52.82	44.64	44.58	46.74	49.61
22.00	129.30	74.61	57.05	47.54	47.07	49.10	51.98
24.00	140.80	80.79	61.33	50.46	49.56	51.43	54.30
26.00	152.30	87.00	65.64	53.40	52.05	53.74	56.57
28.00	163.70	93.23	69.98	56.36	54.54	56.05	58.81
30.00	175.30	99.49	74.35	59.34	57.05	58.36	61.04
32.00	186.80	105.80	78.75	62.34	59.56	60.67	63.25
34.00	198.30	112.10	83.16	65.37	62.09	62.98	65.46
36.00	209.80	118.40	87.60	68.41	64.63	65.29	67.67
38.00	221.40	124.70	92.05	71.46	67.18	67.62	69.88
40.00	232.90	131.00	96.52	74.54	69.74	69.95	72.10
42.00	244.50	137.40	101.00	77.63	72.32	72.28	74.31
44.00	256.00	143.70	105.50	80.74	74.91	74.63	76.53
46.00	267.60	150.10	110.00	83.85	77.51	76.98	78.75
48.00	279.20	156.50	114.50	86.99	80.12	79.34	80.98
50.00	290.70	162.80	119.00	90.13	82.75	81.72	83.22

From Table 3, with F_y = 36 ksi and using interpolation:

$t/b = 17.26 \times 10^{-3} \quad \Rightarrow t = 0.432$ in.

The thickness for the example problem by Salmon and Johnson (1990) is 0.58 in. Note the difference in the result could be due to not considering the effect of variable s in the design.

Example 2

Determine the thickness of the triangular plate in the stiffened beam seat as shown in Figure 4. Use the ASD method with F_y = 36 ksi.

Solution

Neglect the plate material below the dashed line.

$a/b = 10/6 = 1.667$
$P_n = \Omega_c P_a = (1.67)(34) = 56.8$ kips
$P_n s/b^3E = (56.8)(3.8)/[(6^3)(29{,}000)] = 34.46 \times 10^{-6}$

From Table 3 with $F_y = 36$ ksi and using interpolation:

$t/b = 81.38 \times 10^{-3} \quad \Rightarrow t = 0.49$ in.

The thickness for the example problem by Tall (1974) is 0.57 in. Note the difference in the result is due to not considering the effect of variable *s* in the design.

Note that the design work also requires checking the bracket plate system for all the limit states for bracket plates as per AISC *Specification* Equations J4-1 to J4-4. These equations are also reproduced here.

For tensile yielding:

$$R_n = F_y A_g \tag{23}$$

where
$\phi_c = 0.90$ (LFRD)
$\Omega_c = 1.67$ (ASD)

For tensile rupture:

$$R_n = F_u A_e \tag{24}$$

where
F_u = minimum specified tensile strength
ϕ_c = 0.75 (LFRD)
Ω_c = 2.00 (ASD)

For shear yielding:

$$R_n = 0.6 F_y A_g \tag{25}$$

where
ϕ_c = 1.00 (LFRD)
Ω_c = 1.50 (ASD)

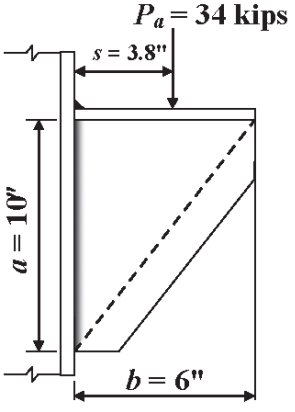

Fig. 4. Triangular bracket plate for Example 2.

For shear rupture:

$$R_n = 0.6 F_u A_{nv} \tag{26}$$

where
A_{nv} = net area subject to shear
ϕ_c = 0.75 (LFRD)
Ω_c = 2.00 (ASD)

CONCLUSIONS

Based on the comparison of results based on the authors' developed relations with the results of design methods by (Salmon et al., 1964; Martin, 1979; Martin and Robinson, 1982) and the experimental results, the following conclusions can be made:

- The relations developed based on column strength equations from the AISC *Specification* are accurate and conservative.
- The developed relations can also be used to size the stiffener plate in a stiffened seated connection as shown in Figure 1d with $s = 0.8b$ [Refer to Figure 10-10b (AISC, 2005b)].
- The limiting value for plate thickness, t^*, is established (see Equation 15 and Table 1) to avoid elastic buckling failure.
- The equations developed are applicable to both ASD and LRFD design approaches.
- The authors developed relations comparable to other theoretical relations in that they include most of the design parameters.

NOMENCLATURE

A_e = net effective area of the plate member
A_g = gross area of the plate member
A_{nv} = net area subject to shear
a = height of bracket
b = length of the loaded side of plate
B = normal distance from hinge (corner) to free edge of plate
dz = width of the elemental strut
E = modulus of elasticity
F_{cr} = critical compressive stress
F_e = elastic critical buckling stress
F_u = minimum tensile stress of steel

F_y = minimum yield stress of steel

I = second moment of area of steel section

K = effective length factor

l_z = length of strut at z distance from o

P_a, P_u = service and factored load

P_n, R_n = nominal design strength

r = radius of gyration

s = position of load

t = thickness of bracket plate

ϕ_c = resistance factor (load and resistance factor design)

Ω_c = safety factor (allowable stress design)

APPENDIX A

Substituting Equation 11 for λ_{cz} into Equation 19, we get

$$P_n s = tF_y \left[\int_0^{z_1} 0.658^{(\alpha z)^2} z\, dz + 0.877 \int_{z_1}^{B} \frac{z dz}{(\alpha z)^2} \right] \quad \text{(A-1)}$$

Integrating Equation A-1, we have

$$P_n s = tF_y \left[\frac{\left[0.658^{\alpha^2 z^2} \right]_0^{z_1}}{2\alpha^2 \log_e 0.658} + \frac{0.877 \left[\log_e z \right]_{z_1}^{B}}{\alpha^2} \right] \quad \text{(A-2)}$$

Substituting for α and z_1 using Equations 12 and 13, scaling both sides by b^3E, and simplifying, Equation A-2 will reduce to Equation 20.

REFERENCES

AISC (2005a), *Specification for Structural Steel Buildings*, American Institute of Steel Construction, Chicago, IL.

AISC (2005b), *Steel Construction Manual*, 13th ed., American Institute of Steel Construction, Chicago, IL.

Martin, L.H. (1979), "Methods for the Limit State Design of Triangular Steel Gusset Plates," *Building and Environment*, Vol. 14, pp. 147–155.

Martin, L.H. and Robinson, S. (1982), "Experiments to Investigate Parameters Associated with the Failure of Triangular Steel Gusset Plates," *Joints in Structural Steelwork, the design and performance of Semi-Rigid and Rigid Joints in Steel and Composite Structures and Their Influence on Structural Behavior*, John Wiley and Sons, New York, NY, pp. 1.74–1.91.

Salmon, C.G. (1962), "Analysis of Triangular Bracket-Type Plates," *Journal of the Engineering Mechanics Division*, ASCE, Vol. 88, EM6, pp. 41–87.

Salmon, C.G., Buettner, D.R. and O'Sheridan, T.C. (1964), "Laboratory Investigation of Unstiffened Triangular Bracket Plates," *Journal of the Structural Division,* ASCE, Vol. 90, No. ST2, pp. 257–278.

Salmon, C.G. and Johnson, J.E. (1990), *Steel Structures Design and Behavior*, Harper & Row Publishers, 3rd ed., New York, NY, pp. 878–883.

Tall, L. (1964), *Structural Steel Design*, The Ronald Press Company, 1st ed., New York, NY pp. 550–555.

Tall, L. (1974), *Structural Steel Design*, The Ronald Press Company, 2nd ed., New York, NY pp. 586–591.

Effects of Slab Post-Tensioning on Supporting Steel Beams in Steel Framed Parking Deck Structures

BHAVNA SHARMA and KENT A. HARRIES

AISC Design Guide 18, *Steel-Framed Open-Deck Parking Structures* (Churches, Troop and Angelof, 2003), discusses the use of cast-in-place post-tensioned concrete slabs in steel-framed parking structures. In Section 3.3.2.1 of Design Guide 18, the authors reflect on the manner in which the post-tensioning force is resisted by and affects the supporting beam: in a noncomposite or composite manner. They conclude that the post-tensioning force is carried almost entirely in a composite manner (minus effects of shrinkage and elastic shortening). This conclusion is based on results of unpublished research and is corroborated by earlier design guidance provided by Bakota (1988). The objective of this field study is to quantitatively assess the effect that slab post-tensioning forces have on their supporting steel members.

CURRENT PRACTICE

Cast-in-place post-tensioned concrete slabs on steel girders are an attractive alternative for parking structures. The use of post-tensioned (PT) slabs permits somewhat longer spans to be achieved than for non-PT slabs but primarily enhances the durability of the slab system, affecting superior crack control and improved negative moment region behavior. Investigation of the effects of the post-tensioning stress on the composite behavior of the beams has been explored but not published. Current practice, as promulgated in AISC Design Guide 18 (Churches et al., 2003) assumes that the composite beams experience a small amount of compressive stress from the post-tensioning of the slab. Design Guide 18 notes that unpublished testing by Mulach Steel Corporation demonstrated a "stress increase of 3% in the composite beams under dead load conditions." Discussion of these tests with Churches (2007) indicated that this increase is the net additional tensile stress in the tension flange of the beam associated with the combination of PT-induced flexure (tension) and PT-induced axial (compression) forces.

Bakota (1988) explores the design of a post-tensioned parking deck and analyzes the effects of post-tension stresses on the composite beam. The author notes various design criteria for a post-tensioned deck and that an effective post-tension stress of 100 psi in the transverse shrinkage and temperature direction reduces the effects of the post-tensioning parallel to the beam. Bakota presents equations to determine the long-term stresses and deflections. He concludes that the post-tension forces in the deck create long-term beam and slab stresses due to differential volume changes.

Steel-framed parking structures, in general, were introduced in the literature in the 1970s (Sontag, 1970; AISC, 1974). Frequent references and case studies appear in the literature through today: in North America, typically appearing in *Modern Steel Construction*; in Europe, in *Acier-Stahl-Steel*; and elsewhere including a number of references in the South African Journal, *Steel Construction*. In addition to Design Guide 18, AISC promulgates *Innovative Solution in Steel: Open Deck Parking Structures* (Troup and Cross, 2003). Available references in the literature primarily address precast concrete decks on steel frames (Simon, 2001; Englot and Davidson, 2001; Flynn and Astaneh-Asl, 2001). A review of available literature revealed no additional publications relating specifically to cast-in-place post-tensioned concrete decks on steel frames.

TEST STRUCTURE

To investigate the effects of post-tensioning the concrete deck on the steel structure, a candidate test structure was selected, instrumented and monitored through its construction and initial service (Sharma and Harries, 2007). All reported testing-related activities were carried out between November 10, 2006, and January 12, 2007. The test structure is a single-story steel parking structure having a post-tensioned composite concrete deck. The structure, shown in Figure 1, is a single-story steel frame over a slab on-grade. Parking is provided on both levels, although there is no connecting ramp. Separate entrances are provided for the grade and deck parking.

As shown in Figure 2, the structure has 11 bays (10 measuring 20 ft and the first measuring 15 ft) in the north-south (N-S) direction and two bays in the east-west (E-W)

Bhavna Sharma is a Ph.D. and IGERT Fellow candidate at the University of Pittsburgh, Pittsburgh, PA.

Kent A. Harries is an assistant professor, University of Pittsburgh, Pittsburgh, PA.

direction: bay 1-2, measuring 45 ft 2 in., and bay 2-3, measuring 35 ft 2 in. There is a 10-ft cantilever beyond column line 3. All columns are W12×65 and the beams spanning bay 1-2 are W24×76 at beams C and D and W24×68 at beam B. Where beams frame into girders, a simple full-depth double-angle shear connection is provided. Beams that frame into columns (all strong axis for the beams considered in this study) are provided with angles at both top and bottom flanges, resulting in a partially-restrained connection. The beams considered in this study span bay 1-2 at column lines B, C and D and are referred to as beams B, C and D, respectively, as indicated in Figure 2. The span of the structure considered is approximately 45 ft and is not necessarily representative of a typical steel-framed parking structure, which often span approximately 60 ft. Nonetheless, all elements are proportional and thus the conclusions drawn based on the 45-ft span are believed to be representative.

The cast-in-place concrete deck is a 6-in. post-tensioned concrete slab. Reinforcing details of the deck are shown in Figure 3. Single, double and triple strands are arranged as shown in Figure 2b. All strands have their anchorages centered in the 6-in. deck depth. The concrete stress due to initial post tensioning is 330 psi in the N-S direction and 168 psi in the E-W direction. Mild steel is arranged primarily

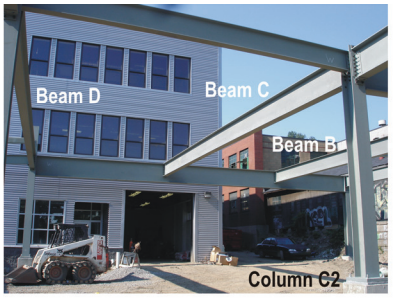

(a) Beams B, C and D during erection.

(b) Deck prior to concrete placement.

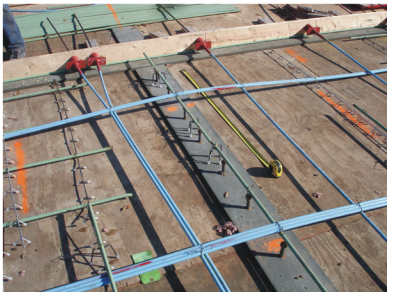

(c) Beam B at girder 2.

(d) Concrete placement.

(e) Pulling PT strand near beam A.

(f) Completed structure looking North; beams B, C and D in far background.

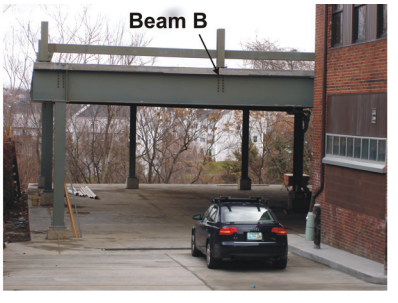

(g) Completed structure looking East showing beams A and B.

Fig. 1. Test structure.

for crack control as indicated in Figure 3. Additionally, $\frac{5}{8} \times 3$ in. shear studs are provided along all beams in bay 1-2 at a spacing of 10 in. as shown in Figure 1c.

Materials

All structural steel members considered in this study are ASTM A992 Grade 50. No material tests were conducted on this steel. The specified concrete compressive strength was 5,000 psi. Both the University of Pittsburgh team and the contractor placed test cylinders. The 28-day concrete compressive strength was determined to be 5,100 psi and the 5-day strength (at the time of pulling the PT strand) was 3,450 psi. All post-tensioning strands used in the deck were ½-in., 270-ksi, seven-wire prestressing strands (A_{ps} = 0.153 in.^{2}). The strand was enclosed in a greased plastic sheath. All mild reinforcement in the deck is #5 epoxy-coated reinforcing bar having a nominal yield strength of f_y = 60 ksi. No material tests were conducted on any of the steel reinforcement. The mild steel was provided only for crack control and is not sufficient to affect the deck structural behavior.

Instrumentation

Electrical resistance strain gauges were installed on beams B, C and D. As shown in Figure 4, gauges were located at five sections along beams B and D and at three sections along beam C. At each section, three gauges were provided as shown in Figure 4b: one on the bottom of the top flange,

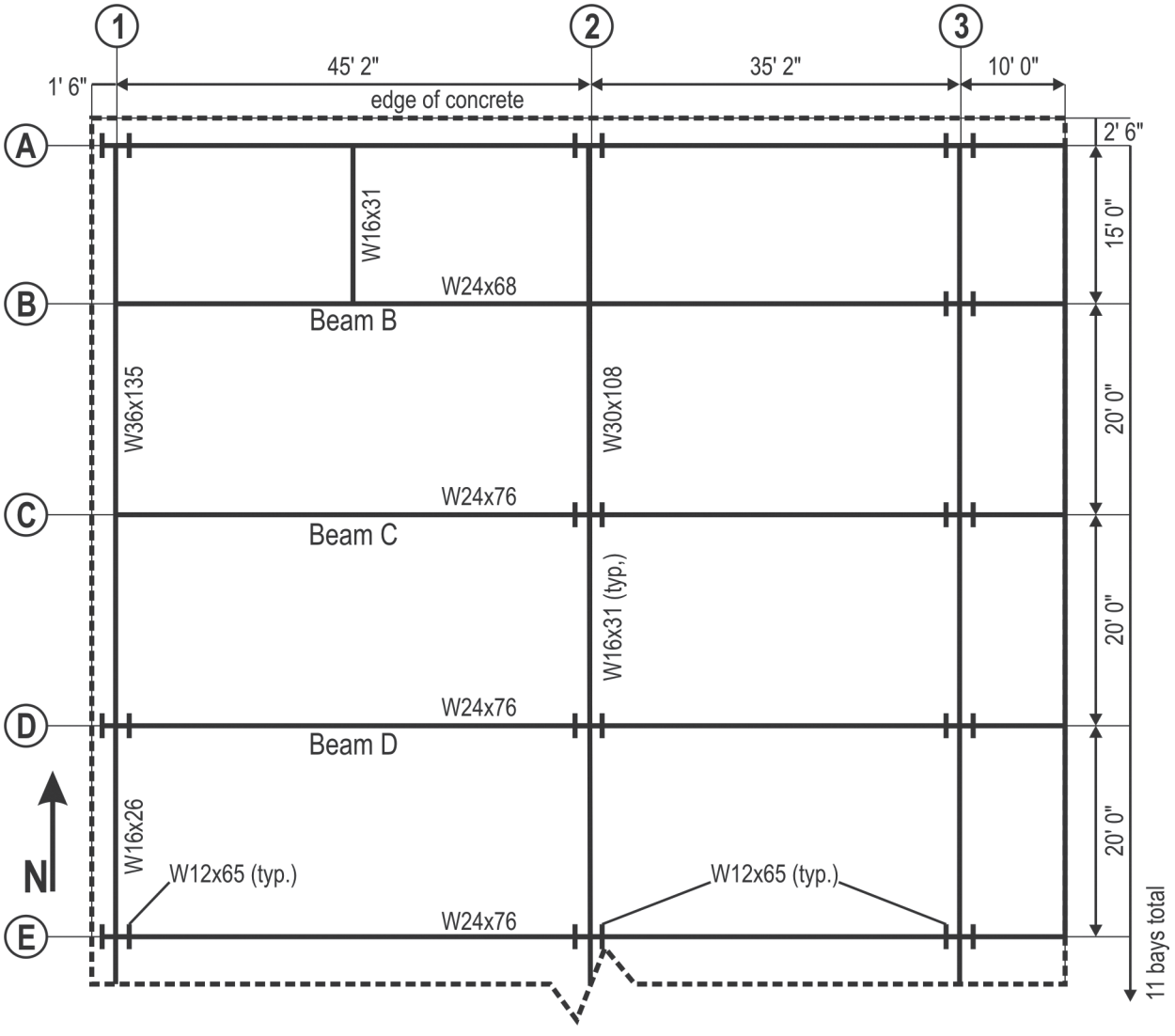

Fig. 2. Test structure steel plan.

one on the top of the bottom flange, and one at the midheight of the web. Gauges are designated by their beam designation and the number 1 through 15, as shown in Figure 4a (e.g., gage D8 is the web midheight gage at midspan of beam D). All gauges were oriented longitudinally to capture flexure-induced strains. The flange gauges were located 1.5 in. from the face of the web so as to avoid both the k-region fillet and the lapping of the deck form (Figure 4b). Strain measurements were taken at various construction milestones and corrected for temperature in accordance with the manufacturer's provided gauge data. All reported data were acquired at ambient temperatures ranging from 38 °F to 52 °F; thus temperature effects were relatively insignificant. "Zero" readings were taken with the bare steel beams supporting only their own self weight and all subsequent data were reported relative to this value. As seen in Figure 4c, form shores were subsequently installed without consideration of the gauges. Where shores bear on the gauges directly, the gauge was damaged and the data not considered in the study.

The fundamental data collected in this work are the longitudinal strains observed at each of the 39 strain gauges. Construction milestones included placement of the concrete, the post-tensioning operation, removal of the shores, and the resulting transfer of the full dead load of the structure to the beam. The milestones are taken as being representative of the stages of the structure's construction and initial operation.

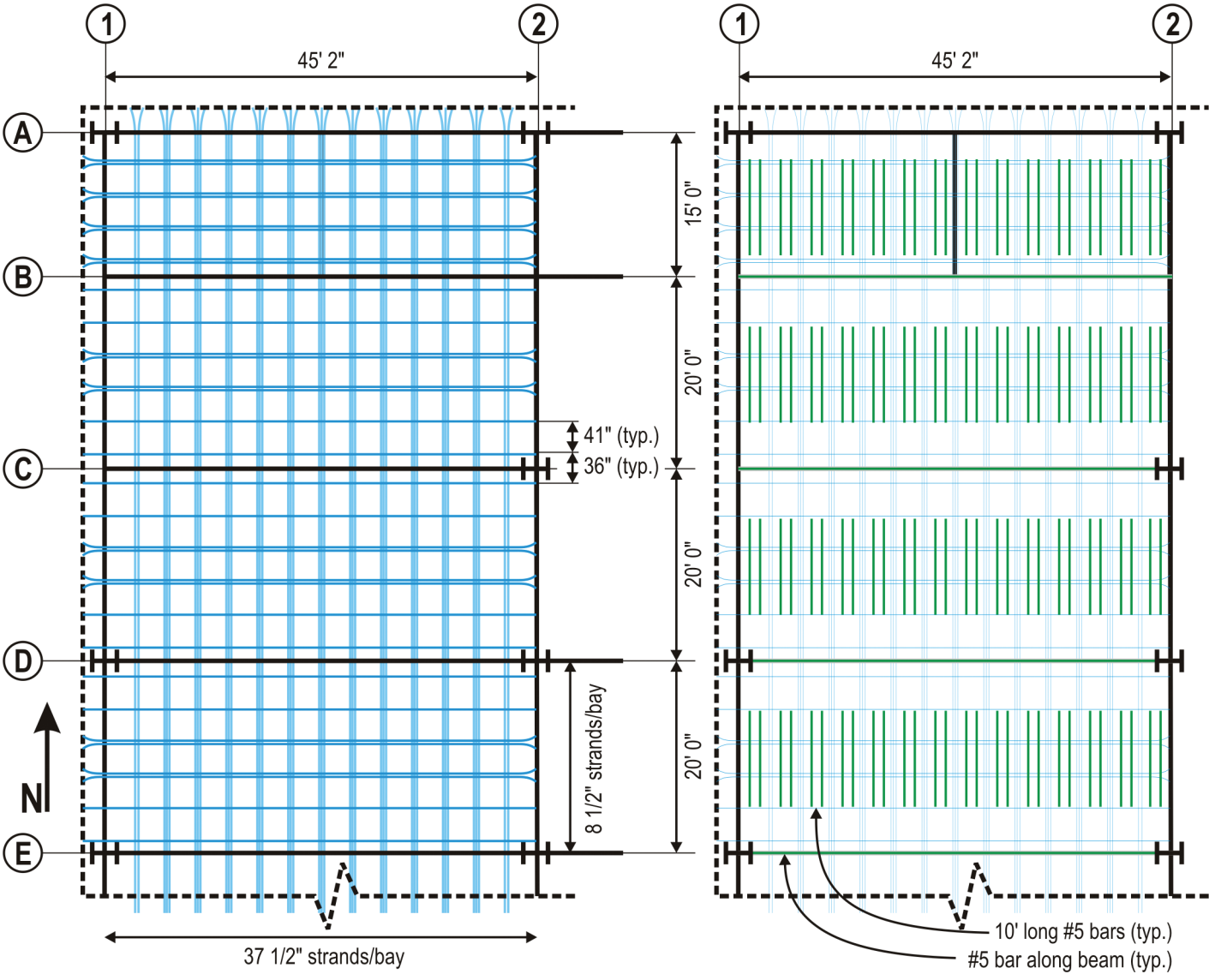

Fig. 3. Test structure slab reinforcement.

All data are provided *relative to the zero readings,* and thus the strains reported do not include the strains associated with the dead load of the beam itself (including some minor construction loads associated with the formwork). Based on a simple span, the maximum stress and strain (in other words, that at midspan) associated with the beam dead load, at the location of the gauges (inside face of flanges), are 1,195 psi and 41 microstrain, respectively. Based on a fixed-fixed span, these values fall to 398 psi and 14 microstrain, respectively. These values have not been added to the data shown because the exact support conditions are uncertain and may vary subtly from beam to beam (Figure 2). The reader is reminded that the top and bottom gage locations are on the insides of the flanges and therefore do not represent the absolute maximum value of strain observed in the steel section.

POST-TENSIONING OPERATION

Post-tensioning of the bay 1-2 slab was conducted when the concrete was five days old. The bay 2-3 slab had not been placed at this time. Concrete strength at the time was 3,450 psi. Tensioning of the secondary strands (i.e., parallel to the beam) began at beam line A and progressed southward along the deck (Figure 2). The ½-in. unbonded strands were pulled from their end along girder line 2 (Figure 1e) with their anchorage 45 ft away at girder line 1. Each strand was pulled to a stress of 216 ksi (0.80 f_{pu}), resulting in an initial strand force of 33,000 lb. Friction and seating losses (ACI, 2005) result in an initial prestress in the tendons following lock-off of approximately 198 ksi (0.73 f_{pu} = 30,200 lb). Long-term losses associated with concrete creep and shrinkage (Aalami, 2004) amount to an additional loss of approximately 9 ksi (0.03 f_{pu}), resulting in a final long-term effective prestress of approximately 189 ksi (0.70 f_{pu}), in the E-W direction. The resulting compressive stress in the concrete in the E-W direction is 160 psi.

Following post-tensioning in the E-W direction, the N-S primary strands were pulled. Based on a stress in the tendon of 0.70 f_{pu}, the resulting concrete stress in the N-S direction following lock-off is approximately 330 psi. In reality, this value is considerably lower due to the length of tendons (approximately 220 ft) and the wobble introduced by the changing slope of the deck and draping of the strand in the N-S direction. Control of the stressing operation was through a

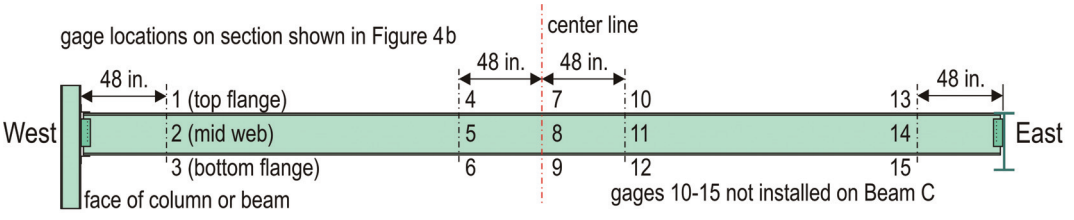

(a) Electrical resistance strain gauge layout along beams B, C and D.

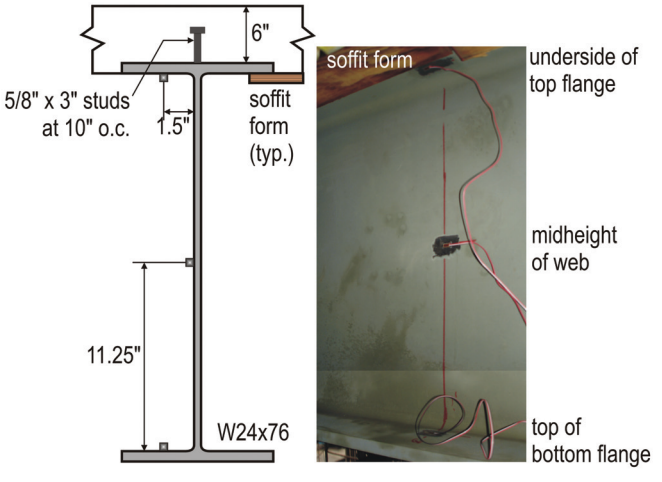

(b) Gauge installation at section.

(c) Gage installation showing form shore installed on top of gauge at this location.

Fig. 4. Instrumentation layout.

pressure-limiting pump operating the stressing jack. Strand elongation—expected to be 3.125 in. in the E-W direction—was also verified at each strand. No moist or accelerated curing techniques were used, which resulted in greater shrinkage losses than are typically expected.

Continuous monitoring of gauges 4, 5 and 6 on beam B and gauges 7, 8 and 9 on beam D was carried out throughout the post-tensioning operation. Gauge readings were recorded at a rate of 1 Hz throughout the operation. Strain-time histories for all six gauges are shown in Figure 5, which shows *relative* strains through the post-tensioning operation. All gauge data was zeroed at 12:50 P.M.—just prior to the initiation of the post-tensioning operation at beam A.

The post-tensioning of the strands immediately above beams B and D occurred at approximately 12:59 P.M. and 1:18 P.M., respectively. In each case approximately one-half of the eventual strain had been developed at these times. It is additionally clear from Figure 5 that only the strands tributary to a girder affect the strain in that girder. It is noted that the "initial condition" of beam D strains in Figure 5 is essentially the same as those of beam B. Little effect from the stressing of beam B (or beam C, between these girders) is apparent in the behavior of beam D. Additionally, despite the observations of Bakota (1988), little effect on the observed beam strains were observed following pulling of the perpendicular (N-S) strands.

LIVE LOAD TESTS

An initial live load test to simply assess the composite behavior of the deck, under full dead load (and to determine the need for a more substantial live load test) was conducted on beam D. In this test, a four-door sedan having specified front and rear GAVW of 1,960 lb and 1,942 lb, respectively, was positioned over the center of Beam D. From the live load strain distribution obtained, the location of the beam neutral axis was determined and the resulting applied moment found. Based on ACI-prescribed design assumptions (composite behavior with an effective slab width, b_{eff} = 105 in.), the maximum observed live load moment is 195,800 lb-in.—this may be interpreted as a lower-bound value. Based on AISC-prescribed design assumptions, the entire tributary slab width is effective (b_{eff} = 240 in.) and the maximum observed live load moment is 212,250 lb-in.—this may be interpreted as an upper-bound value.

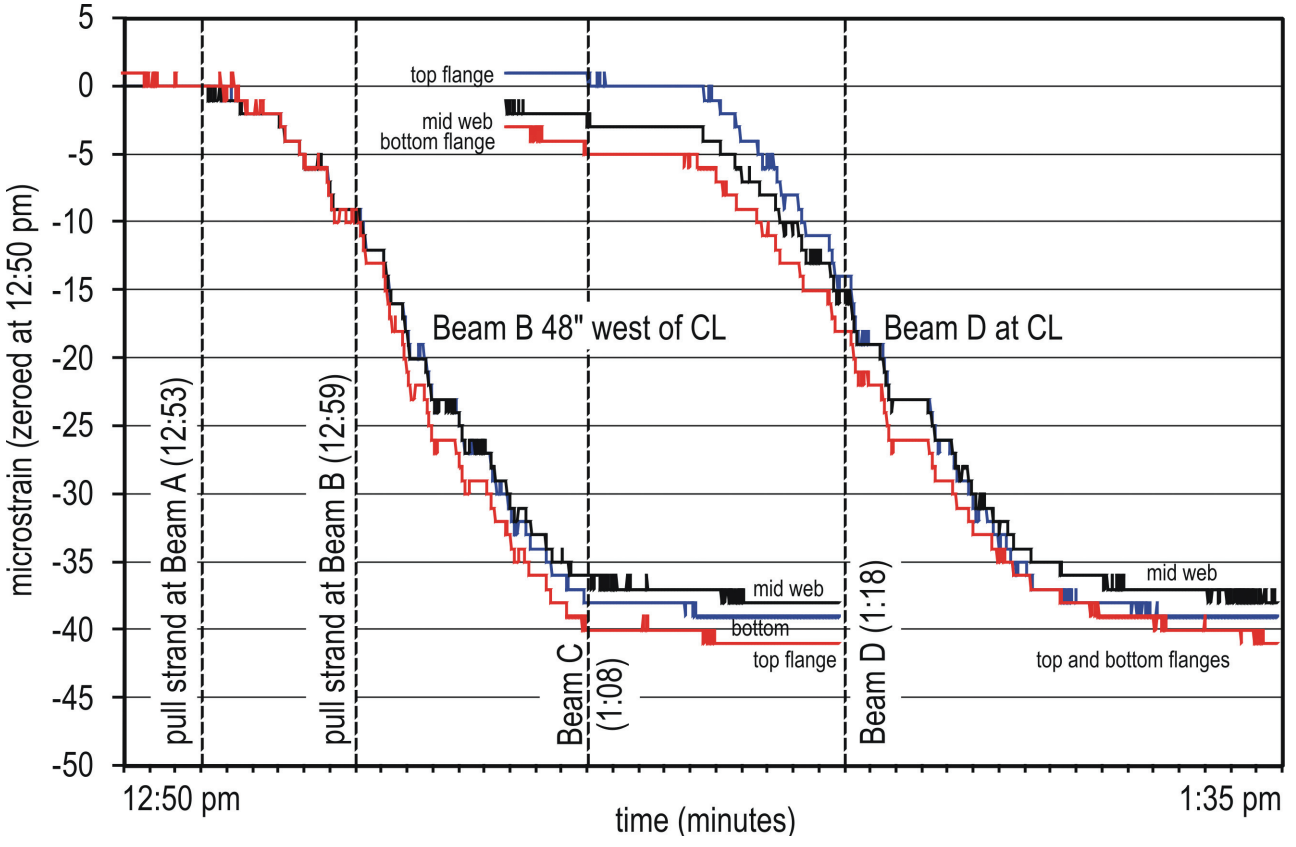

Fig. 5. Strain-time history during post-tensioning operation.

Table 1. Results of Two-Vehicle Live Load Test				
	Assumption	Beam at Midspan (gage 9)		
		B	C	D
Observed tension flange strain (microstrain)		173[a]	42	44
Apparent neutral axis depth[b], y (in.)		[a]	7.0	3.0
Apparent moment (lb-in.)	b_{eff} = 105 in.[c]	[a]	324,000	289,000
Apparent moment (lb-in.)	b_{eff} = 240 in.[d]	[a]	351,800	313,700
Applied moment (lb-in.)	Simply supported	815,500		
Applied moment (lb-in.)	Fixed supports	335,200		

[a] Beam B strain is believed to be an incorrect reading.
[b] Measured from top of 6-in. slab on W24 section.
[c] ACI 318 recommended effective width (see Table 2).
[d] Effective width taken as beam spacing (see Table 2).

The theoretical live load moment resulting from the single vehicle bending case applied is 458,484 lb-in. for a simple span and 203,290 lb-in. for a span having fixed supports. Based on the observed strain behavior, beam D is clearly behaving as a composite member having ends largely restrained from rotation. This result is considered reasonable based on the relatively low stress level applied and the presence of full-depth web angles and partially restrained top and bottom flange angle connections at both ends of beam D.

A second live load test was conducted on all beams. In this test, two vehicles with specified front and rear GAVW of 1,960 lb and 1,942 lb, and 1,714 lb and 1,402 lb, respectively, were positioned over the center of each beam in sequence. The strains resulting only from the application of the live load are given in Table 1. From the live load strain distribution obtained, the location of the beam neutral axis was determined and the resulting applied moment determined. Based on the observed strain behavior and neutral axis locations reported in Table 1, all beams are clearly behaving as composite members having ends largely restrained from rotation.

BEHAVIOR OF STRUCTURAL SYSTEM

Effective Width of Slab

For a steel beam having a composite concrete deck, it is necessary to determine the effective width, b_{eff}, of the flange contributing to the composite beam behavior. For the post-tensioned structure considered, different values of b_{eff} are appropriate for use at different stages of the construction process.

Effective Width While Formwork Is in Place ($b_{eff,\ form}$)

Between the time that the concrete deck hardens and begins acting compositely with the underlying beams and the time at which the formwork support is removed, a limited portion of the deck slab is able to act in a composite manner with the beam. The formwork supporting the majority of the slab is stiffer in resisting gravity loads than the beam, therefore only that portion of the slab tributary to the beam will affect the load carrying capacity of the beam. In this work, this effective width, $b_{eff,\ form}$, is taken as 36 in. based on the observed spacing of the formwork in the vicinity of the beams.

Code-Prescribed Effective Width

Only following the removal of the formwork or shores does the beam begin to act in its "designed-for" composite manner. Table 2 gives the code-prescribed values of effective width for both the current AISC and ACI standards. The values given are for beams B, C and D having a 6-in.-deep slab. For design, the value for b_{eff} would be taken as 135 in. (AISC) or 105 in. (ACI). However, design is based on an ultimate load case, in which case some level of slab degradation and cracking is expected. For the dead load and relatively low service load cases considered in this work, the effective width is more appropriately taken as the area tributary to each beam (i.e., b_{eff} = 240 in.). Nonetheless, the selection of effective width has only a marginal effect on the maximum stresses in the steel beam. Considering the range of effective width reported in Table 2, the maximum tensile stress is reduced by only 7% as b_{eff} ranges from 105 in. to 240 in.

Table 2. Effective Width Recommendations		
Parameter	**AISC 2005 Section I3.1a**	**ACI 318-05 Section 8.10.2**
¼ beam span	b_{eff} = 135 in.	b_{eff} = 135 in.
Beam spacing	b_{eff} = 240 in.	n.a.
Clear distance to next web	n.a.	b_{eff} = 240 in.
16 times slab thickness plus beam width	n.a.	b_{eff}f = 105 in.
n.a. = not applicable in cited code document		

Table 3. Transformed Section Properties				
Parameter	**Section Behavior**			
	Bare Steel	**Composite at PT Stressing**	**Composite at 28 days**	
Concrete strength, f'_c (psi)	-	3,000	5,000 psi	
Modular ratioa, $n = E_s/E_C$	-	9.3	7.2	
Effective width of slab, b_{eff} (in.)	-	36	135	240
Moment of inertia, I (in.^{4})	2,100	4,651	6,282	6,614
Neutral axis depth (from top of slab), y (in.)	12	10.3	5.5	4.5
Elastic section modulus, top of steel, S_t (in.^{3})	–176	–1,073	12,105	4,424
Elastic section modulus, bottom of steel, S_b (in.^{3})	176	238	257	260
Elastic section modulus, top gage location, S_t* (in.^{3})	–187	–1,272	5,240	3,041
Elastic section modulus, top gage location, S_b* (in.^{3})	187	246	265	268
[a] Ec = 57,000 $\sqrt{f'_c}$; Es = 29,000 ksi				

Table 4. Predicted and Observed Behavior at Midspan of Beam D						
Load Case	**Assumed Behavior**	**S_b*[a]**	**Moment**	**Bottom Flange Strain**		**Predicted / Observed**
				Predicted	**Observed**	
		in.^{3}	**lb-in.**	**με**	**με**	
Steel self-weight	Noncomposite	187	223,257	41	-	-
Concrete with shores in place[b]	Noncomposite	187	881,616	163	163	1.00
Full concrete dead load[b]	Noncomposite	187	4,612,319	851	ntc	-
Full concrete dead load[b]	Composite b_{eff} = 240 in.	268	4,612,319	593	570	0.96
Single-vehicle live load[c]	Simple support	268	458,484	59	ntc	-
	Fixed supports	268	203,290	26	25	0.96
Two-vehicle live load[c]	Simple support	268	815,500	105	ntc	-
	Fixed supports	268	335,200	43	44	1.02

[a] Elastic section modulus at gage location (see Table 3).
[b] Excludes self weight of steel as this effect is "zeroed" out of observed strains.
[c] Strains due to live load only.
ntc = not the case in test structure—shown for comparison with subsequent table entry.

Predicted Section Behavior

Table 3 provides a summary of composite section properties calculated using different parameters for beams C and D (W24×76 steel section) corresponding to three phases in the structure's construction: bare steel behavior, behavior at post-tensioning, and eventual design behavior (using both the design value of b_{eff} and the beam spacing). An important aspect of behavior shown in this table is the upward migration of the neutral axis location as a greater effective width, b_{eff}, is engaged, and as the concrete strength and modulus increases.

Predicted Behavior of Beam D

Based on the composite section properties presented in Table 3, the expected strain behavior at the midspan of beam D is presented in Table 4. The bottom flange at midspan is chosen for comparison because simple and fixed end moments may be directly compared and the degree of fixity established; and tension flange strains are greater and thus error and noise are proportionally reduced. The length of the beam is taken as 44 ft 2 in.

The predicted behaviors for dead load applications presented in Table 4 are based on *simply supported end conditions* and thus represent upper-bound values. To obtain values for fixed-fixed end conditions for the beam midspan, the tabulated values of midspan moment may be multiplied by 0.33; representing a lower-bound value. The values reported for the live load applications, on the other hand, are presented for both simple and fixed support conditions. In all cases the strains are determined at the gage locations (in other words, using values of S_t* and S_b* from Table 3, as indicated) and E = 29,000 ksi.

In the cases shown in Table 4, the effect of steel dead load is calculated to result in a strain of 41 microstrain. Because data are zeroed based on this value, all subsequent data are reported *relative* to this value; thus it is necessary to add 41 microstrain to all reported values to obtain the actual steel strain. Similarly, the reported live load strains are only those resulting from the application of live load; the dead load strains must be similarly added to these to obtain the actual strain.

The exceptional agreement between predictions based on fundamental assumptions and observed strain data shown in Table 4 illustrates the following aspects of the beam behavior:

1. The assumption of an approximately 36-in. tributary width of fresh concrete being carried by the beam is reasonable ("concrete with shores in place," in Table 4).
2. Dead load is carried primarily in simple bending ("full concrete dead load").
3. The beam behaves as a dominantly fixed ended beam in resisting the relatively small live loads used ("vehicle live load").

The apparent discrepancy between observations 2 and 3 results from the fact that the top and bottom flange angles used where beams frame into columns were not actually tightened at the time of placing the concrete or later removing the forms. It is not clear when and/or if these angles were tightened; however, the presence of the composite slab appeared to stiffen the support conditions by providing a degree of continuity between the beam and supporting girder. This effect, and the low live loads used, should be expected to result in a beam "made continuous for live load" regardless of the presence of flange angles. The observed behavior supports this observation.

A final comment on Table 4 is warranted. The post-tensioning force is introduced after the placement of the concrete and thus should affect all subsequent milestones. However, as will be shown in the following section, the resulting compression strains from the PT forces on the bottom flange of the steel beam are largely "decompressed" (undone) by the PT-induced flexure introduced upon the removal of the shores. As will be shown, this is partially an artifact of the force levels and geometry of the structure considered.

Post-Tension-Induced Stresses

The following discussion is presented in the order in which the post-tensioning operation is carried out and assumes the general scenario whereby the concrete is placed, the post-tensioning is pulled, and then the forms are released.

Post-Tensioning Operation

During the initial post-tensioning operation, the slab remains shored. Axial stresses in the deck system are self-equilibrated resulting in internal stresses associated with the axial force (in other words, the P_i/A component). Flexure-induced stresses associated with the eccentricity of the PT tendons (in other words, the $P_i e/S$ component), however, are largely resisted by the stiff formwork system (recall that the formwork is considerably stiffer than the beam in resisting vertically oriented forces). Thus, only the axial stresses are carried in the beam at the time of post-tensioning. Based on these assumptions, the expected axial strain in the beam and slab due to post-tensioning is 47 microstrain. As reported in Figure 5, the observed axial strain is on the order of 40 microstrain. Factors affecting both the predicted and observed values include (a) the expected variability in concrete properties at an early age and (b) the assumption of 100% composite behavior being developed in carrying axial load. Generally, one would expect the measured steel strains to be lower than the concrete strains. In this light, and based on previous experience, the observations and predictions correlate remarkably well.

Analysis of Post-Tensioning Operation

The assumption promulgated earlier that the post-tensioning operation results in only axial stresses provided the slab remains shored is, admittedly, an idealization. A rigorous analysis of the problem may be made by considering the shored system as a beam on elastic foundations subject to an eccentric axial force producing moments at each end. The elastic foundation, representing the shores, is assigned a stiffness in terms of a unit stress to cause a unit deflection (psi/in., for instance). This stiffness is effectively the axial stiffness of the shoring system resisting vertically applied loads. In general, this stiffness will be relatively large because it effects the vertical deflection of the forms when placing the concrete deck. The shore stiffness has no effect on the axial component of the PT force. The effect of the induced moment is determined based on the behavior of a beam on elastic foundations. Such an analysis is shown schematically in Figure 6.

The midspan moment, M, and vertical deflection, y, due to the PT-induced moment, M_0, may be found to be (Young and Budynas, 2002):

$$M = M_0 \frac{-\cosh \beta\ell \cos \beta\ell}{1 + \sinh^2 \beta\ell - \sin^2 \beta\ell} \tag{1}$$

$$y = \frac{M_0}{2EI\beta^2} \frac{-\sinh \beta\ell \sin \beta\ell}{1 + \sinh^2 \beta\ell - \sin^2 \beta\ell} \tag{2}$$

where

$$\beta = \left(\frac{b_o k_o}{4EI} \right)^{\frac{1}{4}} \tag{3}$$

ℓ = half span of the shored beam
b_o = width of the shored beam
k_o = stiffness of the supporting shores

For the post-tensioned structure considered, the stresses due to the PT-induced moment are negligible provided the shores remain engaged. The midspan moment, $M = 0.014M_0 = -5{,}454$ lb-in., resulting in an extreme tension flange stress of 21 psi and corresponding strain of less than 1 με. Clearly a variety of assumptions can be made in this calculation; the effective stiffness of the beam, I, the actual applied moment, M_0, and the vertical stiffness of the shores, k_0, being the most significant. For the beam geometry considered, however, the extreme tension flange stress calculated based on a wide range of such assumptions did not exceed 10% of the stress due to the axial component of the PT force.

Release of Formwork

Upon the release of the formwork, the PT-induced flexural stresses resulting from the eccentric application of the PT force are transferred from the formwork shores to the beam. At this stage, the concrete has aged further, resulting in a

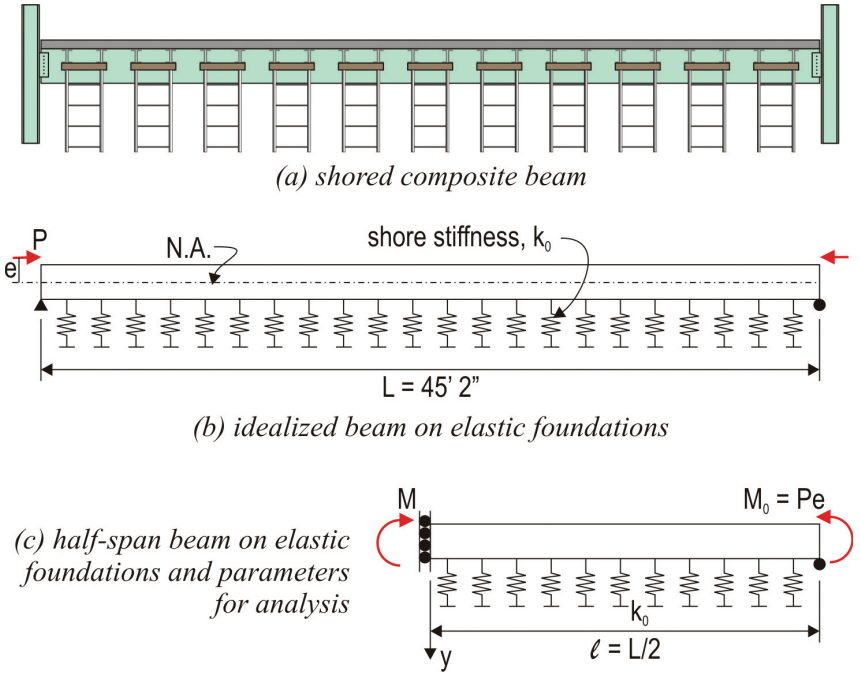

Fig. 6. Schematic representation of shore-supported beam as a beam on elastic foundations.

higher strength and stiffness, which then results in the composite neutral axis migrating upward as the concrete continues to age. If it assumed that the effective width of the slab is 240 in. and the concrete strength has attained a strength of 4,000 psi at the time of formwork release, the additional strain transferred to the bottom flange of the steel beam (at the gage locations) is 50 microstrain. This tensile strain "undoes" the PT-induced axial compressive strain predicted using consistent assumptions to be 47 microstrain.

For the beam and slab geometry considered, the PT-induced flexural strains are approximately 10% of those associated with the transfer of full dead load to the beams (as the forms are released) as shown in Table 4. Additionally, for the geometry considered, the bottom flange strain associated with PT-induced axial force (P_i) and that associated with PT-induced flexure forces (P_ie/S_b) virtually cancel each other. The top flange axial-induced strains are reduced marginally since the neutral axis (in this case) has migrated into the slab.

SUMMARY OF PROCEDURE FOR ASSESSING PT-INDUCED STRESSES

Post-tensioning (PT) forces are introduced to the steel beam-concrete deck system, typically within a week of placing the concrete deck. The concrete deck may be shored (formwork still in place) or unshored when the tensioning operation takes place. The forces resulting from tensioning are resisted by the structural system active at the time of stressing the tendons. If the shores remain in place, the structural system resisting PT-induced forces constitutes the slab, beam and shores. Additionally, the slab-beam composite beam will behave in a composite manner in resisting PT forces to the extent its design permits. That is, where shear studs are provided, the beam will behave in a composite manner with the slab; if studs are not provided, the system will resist forces in a noncomposite manner.

Typically, the unbonded PT tendons will be located at the mid-depth of the slab and will be pulled and anchored in such a manner as to result in concentrated forces being located at the anchorage and pulling ends of the tendon as illustrated in Figure 7. These forces draw the slab into compression and result in an end moment being introduced into the beam. This moment is calculated as the product of the PT force and its lever arm to the neutral axis of the section at the time of tensioning. Thus, the resulting stress in the section is calculated as the sum of the axial and flexural components of the applied PT load, P_i:

$$\sigma_{PT} = P_i/A + (P_ie/S) \quad (4)$$

PT Pulled While Slab Is Shored

If the post-tensioning is pulled while the slab remains shored (Figure 7a), only the PT-induced axial force is transferred to the composite steel beam. The flexural component is primarily resisted by the shores. Thus:

$$\sigma_{PT,\ axial} = P_i/A_{gtr} \quad (5)$$

where

A_{gtr} = gross transformed area of the tributary slab and steel beam composite section determined using the concrete modulus at the time of PT tensioning

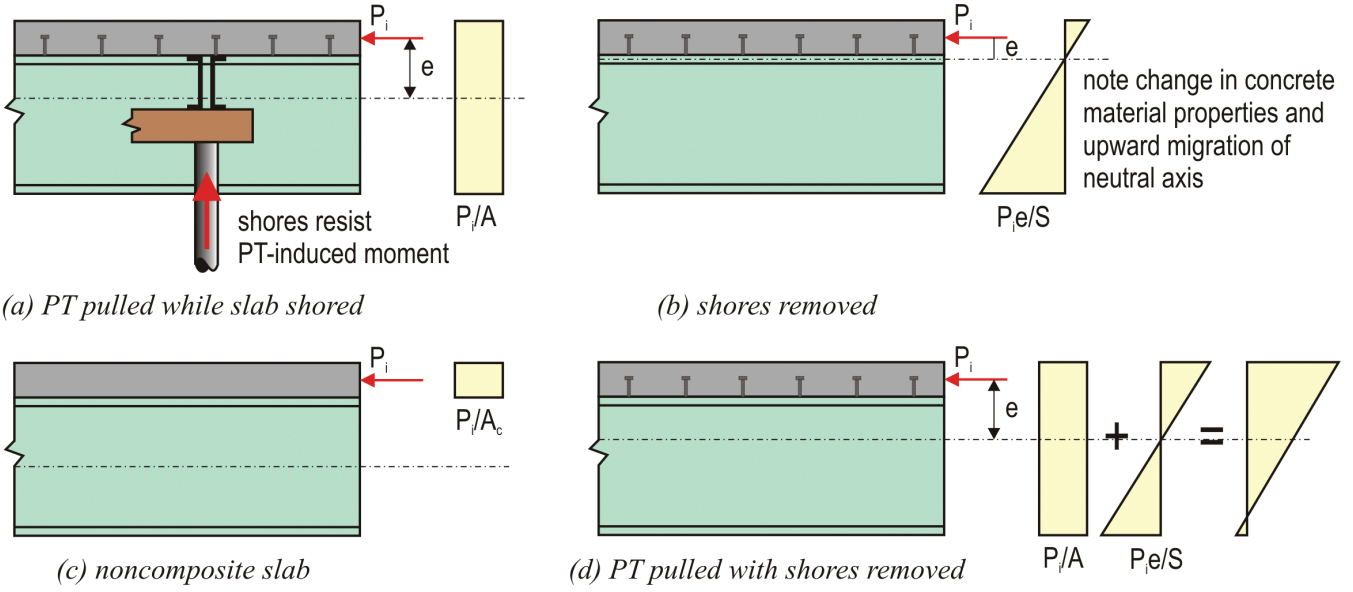

Fig. 7. Effects of post-tensioning forces on members.

Thus a uniform compressive force is applied through the entire composite section (Figure 7a). If the slab is not composite with the beam, this compression is carried only by the slab (Figure 7c). The stiffness of the shoring system may vary; thus a small degree of the PT-induced flexure may be resisted by the beam while the shores are in place. For any reasonable case, however, the extreme tension flange stress due to PT-induced flexure will not exceed 10% of the stress due to the axial component of the PT force while the shores remain engaged.

Once the shores are released (Figure 7b), the PT-induced flexural stresses are transferred to the beam:

$$\sigma_{PT,\,flex} = (P_i e/S) \quad (6)$$

where

e = eccentricity from the tendon centroid to the composite neutral axis

S = appropriate section modulus for the location of interest in the composite section

Both e and S are determined using the concrete modulus at the time of shore release. If the slab is not composite, flexure is only induced in the slab and only if there is an eccentricity in the strands with respect to the slab alone. For most post-tensioned deck applications, the eccentricity will be zero (strand at mid-depth of the slab) and thus no PT-induced flexural stress exists (Figure 7c).

Between the time of PT tensioning (Equation 5) and shore removal (Equation 6), the concrete will age; the modulus will increase resulting in the neutral axis of the composite section migrating upward, reducing the eccentricity, e, in Equation 6.

The net effect of removing the shores after the post-tensioning operation is that the concrete slab compression is increased and the PT-induced axial compression in the tension flange is reduced. Generally, the compression flange is largely unaffected due to its proximity to the neutral axis of the composite beam.

PT Pulled While Slab Is Unshored

This case occurs when the slab forms are supported entirely by the steel beam resulting in an unshored condition throughout the erection process. In this case all PT-induced stresses are carried by the composite beam immediately upon tensioning the strands. In this case, stresses are determined from Equation 4 with all parameters, A, e and S, calculated at the time of PT tensioning (Figure 7d).

Under no circumstances is it possible for the PT-induced flexure to be carried by the noncomposite steel section (Figure 8).

SUMMARY AND CONCLUSIONS

An experimental program of monitoring the during- and post-construction behavior of a steel-framed open parking deck having a cast-in-place post-tensioned concrete slab is presented. Monitoring was carried out following steel erection and ended following completion of the structure. Data were acquired at a variety of stages throughout the construction process. Additionally, two live load tests were conducted. The objective of this field study was to quantitatively assess the effect that slab post-tensioning forces have on their supporting steel members. The following conclusions were drawn:

1. The structure carried its self-weight dead load in a manner consistent with its simply supported design.

2. The relatively small magnitude live loads applied were carried in a fully composite manner with the effective width equal to the beam-to-beam spacing.

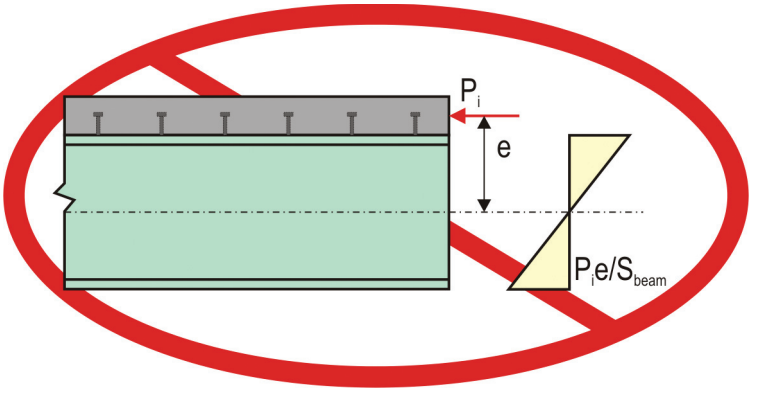

Fig. 8. Under no circumstances can post-tensioning forces be resisted by the steel section alone.

3. While the form shores are in place, the steel beams carry only concrete deck loads tributary to the beam relative to the shores.

4. If shores are in place during the post-tensioning operation, only PT-induced axial stresses are effectively transferred to the supporting steel beams. These stresses may be calculated based on an equivalent transformed gross section analysis.

5. The shores are sufficiently stiff to resist flexural stresses induced by the post-tensioning operation. Once the forms are released, PT-induced flexural stresses are transferred to the supporting steel beam. These stresses should be assessed using a transformed sections analysis and material properties at the time of the form shore release.

6. For the beam and slab geometry considered, the PT-induced flexural strains were approximately 10% of those associated with the transfer of full dead load to the beams (as the forms are released). Additionally, for the geometry considered, the bottom flange strain associated with PT-induced axial force and that associated with flexural forces virtually cancel each other. Resulting in negligible additional stress in the bottom flange of the beam as a result f the two-directional slab post-tensioning. The top flange axial strains are reduced marginally because the neutral axis (in this case) has migrated into the slab.

ACKNOWLEDGMENTS

This study was carried out with support from the American Institute of Steel Construction (AISC). Charles Churches Sr. of Churches Engineering, Washington PA, is the engineer of record for the project. His support and the information he provided is gratefully acknowledged. Eric Campbell of Ionadi Construction, Pittsburgh, PA, was the site supervisor; his assistance was invaluable to the study. The building is owned by Real Estate Enterprises, Pittsburgh, PA; Kai Olander is acknowledged for providing access to the site and test structure. The findings of this work do not necessarily reflect the opinions of those acknowledged here.

REFERENCES

Aalami, B.O. (2004), "Prestressing Losses and Elongation Calculations," *ADAPT, T9-04*, September 2004 (revised October 2004), 16 pp.

ACI (2005), *Building Code Requirements for Structural Concrete*, ACI 318, Farmington Hills, MI.

AISC (2005), *Steel Construction Manual*, 13th ed., American Institute of Steel Construction, Chicago, IL.

Bakota, J.F. (1988), "Parking Structure with a Post-tensioned Deck," *Engineering Journal*, AISC, Third Quarter, pp. 119–125.

Churches, C.H. (2007), personal discussion/correspondence, March.

Churches C.H., Troup, E.W.J. and Angeloff, C. (2003), "Steel-Framed Open-Deck Parking Structures," *Steel Design Guide No. 18*, American Institute of Steel Construction, 113 pp.

Englot, J.M. and Davidson, R.I. (2001), "Steel Framed Parking Garages Take Off at JFK and Newark International Airports," *Modern Steel Construction*, Vol. 44, No. 4, April, 6 pp.

Flynn, L.J. and Astaneh-Asl, A. (2001), "Notes on Design of Steel Parking Structures—Includes Seismic Effects," *Steel Tips*, Structural Steel Education Council.

AISC (1974), "[A] New Structural System for Parking Decks," *Modern Steel Construction*, Vol. 14, No. 2.

Sharma, B. and Harries, K.A. (2007), *Effects of Post-Tensioning on Supporting Beams,* report to AISC, University of Pittsburgh Civil and Environmental Engineering Report No. CE/ST 36, 42 pp.

Simon, A.H. (2001), "Unique Steel Framed Solution to Parking," *Modern Steel Construction*, Vol. 44, No. 4, April, 3 pp.

Sontag, H. (1970), "Steel Multi-Storey Garages," *Acier-Stahl-Steel*, Vol. 35, No. 11, pp 480–490.

Troup, E. and Cross, J. (2003), *Innovative Solutions in Steel: Open-Deck Parking Structures*, American Institute of Steel Construction, Inc., 29 pp.

Young, C.S. and Budynas, R.G. (2002), *Roark's Formulas for Stress and Strain*, 7th ed., McGraw-Hill.

Current Steel Structures Research

REIDAR BJORHOVDE

Seismic strength and performance of steel structures and structural elements continue to be the focus of a very large number of studies all over the world, but probably nowhere as vigorously as in the United States. Apart from the fact that extensive areas in the U.S. now can be seismically active and are treated as such by the International Building Code, this is in part caused by the close relationship between design specifications (= standards) and building codes. Thus, all of the major U.S. materials-based design codes are now incorporated into the building code by reference. Further, the relationships between these groups and organizations such as the Building Seismic Safety Council (BSSC) and various efforts under the auspices of the National Science Foundation emphasize the state-of-the-art character of current code developments in the United States.

Similar efforts are under way in Europe, under the umbrella of the European Union (EU) and its code commission CEN and various funding groups. The standardization work in Europe is greatly complicated by the fact that the EU now has 27 members, but several additional countries are also active participants in these programs. It would not be unreasonable to assume that these efforts would have limited probability of success, but such is not the case at all. So-called National Annexes to the various Eurocodes are prepared by each country before the standards can be put to practical use, but numerous research projects feed relevant information to the individual specification committees. The years 2009 to 2010 are when all national codes are supposed to be ready for implementation, and the design profession is working diligently to ensure that the change-over from old standards can take place with a minimum of technical problems.

Research and development groups in Australia, Chile, China, Japan, Korea, New Zealand, and Taiwan are equally and aggressively seeking improvements to their national design standards for seismic effects. There are many similarities between the practices in these countries and code activities elsewhere, mostly because seismic effects are fundamentally the same. Some differences exist because of differing construction techniques and engineering preferences. It is therefore critical to be able to draw upon the expertise in all locales. At the same time it must be recognized that local approaches may make the application of solutions from other areas difficult, whether it is because of traditions in any form or it is simply impractical to bring in novel construction forms or otherwise expensive solutions.

The research efforts discussed in this paper examine the behavior and strength of braced frames under seismic conditions, emphasizing the advantages of this very common structural system but also the needs for unique performance criteria. Similarly, the energy absorption characteristics of various types of PR connections may offer significant advantages for seismic response, as examined in another project. Using the so-called direct strength method for slender hot-rolled members is being studied by an American researcher who developed the concept for cold-formed steel structures. A major Chinese investigation of structural performance under fire conditions has real applications everywhere, in particular because of its assessment of the efficiency of certain fireproofing techniques and the removal of part of the protection. Composite structures continue to play a major economic role for buildings, and a novel system using precast hollow-core slabs is being studied in England. Finally, stainless steel continues to attract attention for several applications, and Spanish researchers aim to provide practical criteria for plate girders of such materials, as well as novel requirements for hybrid girders.

References are provided throughout the paper, whenever such are available in the public domain. However, much of the work is still in progress, and reports or publications have not yet been prepared for public dissemination.

STRUCTURAL BEHAVIOR AND STRENGTH UNDER SEISMIC LOADS

Special Concentrically Braced Frames (SCBF): This project has been conducted at the University of Washington in Seattle, with Professor Charles W. Roeder as the director. Funded by the NEES-SG program of the National Science Foundation, the project also functions with numerous subcontracts to other institutions in the U.S. as well as in Japan and Taiwan.

Braced frames have been used extensively for steel structures in nonseismic regions, and they offer significant advantages insofar as analysis techniques and economies of

Reidar Bjorhovde is the Research Editor of the AISC *Engineering Journal*.

construction are concerned. Under the designation special concentric braced frames, they are now frequently used in seismically active areas because of their inherent lateral stiffness and strength. The increased use of SCBFs is tied to the performance problems that have been experienced with moment resisting frames. However, unique aspects of the braced frames require more information about their inelastic post-buckling behavior; in particular, the response of the gusset plates and the bracing members.

The researchers at the University of Washington have conducted extensive analytical and experimental investigations of various SCBF gusset plate connections. The analyses are based on inelastic, cyclic deformation evaluations. The 23 large-scale single-story frame specimens that have been tested so far include diagonal braces, beams, columns and gusset plates, as shown in Figure 1.

The tests have been run to reach the full deformation capacity of the frame. Extensive and severe yielding and post-buckling displacements have been found in the brace as well as the gusset plate and the framing members, as shown in Figure 2. Considering that connection design variations have been implemented for each test to examine the impact on the performance of the frame, it is clear that the gusset plate design has a very significant impact on the frame. The study has led to proposals for improved design procedures for the gusset plate and other connection elements.

In addition to the single-story single-bay SCBF tests that have been performed at the University of Washington, two full-scale two-story frame tests have been conducted at the research laboratory of the National Center for Research on Earthquake Engineering (NCREE) at the National University of Taiwan. Professor K.-C. Tsai is the director of NCREE. Figure 3 shows one of the test frames, noting that the test specimen is the structure enclosed within the blue color frame. The blue frame provides the lateral support for the test structure, which has a two-story X-brace system along with a composite floor slab. The tests were conducted under inelastic cyclic displacements until two or more of the braces failed. In addition to the overall system performance, these tests also provided information on the effect of the multi-story bracing configuration as well as the design and performance requirements for the midspan gusset plates.

Fig. 1. Single-story SCBF test specimen (photo courtesy of Charles W. Roeder).

Fig. 2. Post-buckling deformations in the SCBF test frame brace and gusset plate (photo courtesy of Charles W. Roeder).

Fig. 3. Two-story SCBF with a two-story X-brace configuration (photo courtesy of Charles W. Roeder).

Additional SCBF research work will be conducted by the participants at the University of California at Berkeley and the University of Minnesota. These sub-projects will examine the influence of different bracing systems, composite slabs, and the three-dimensional response of the frames. It is anticipated that the research work will continue for an additional three years, offering significant changes and improvements in the design methods for braced frames.

Energy Dissipation Characteristics of Semi-Rigid Connections: This project was conducted some time ago at the University of Oklahoma in Norman, OK, with Professor Anant Kukreti as the director.

Based on the data from 48 full-scale cyclic tests, the project has provided energy dissipation data and characteristics for a range of practical PR (semi-rigid) connections (Abolmaali, Kukreti, Motahari and Ghassemich, 2008). The following types of connections were included in the study:

- Bolted-bolted double web angle connections
- Welded-bolted double web angle connections (welded to beam web)
- Top and seat angle connections
- Flush end-plate connections
- Extended unstiffened end-plate connections

All of the connections used slip-critical bolts. The test assembly columns were W14×159 shapes in 50 ksi yield stress steel; the beam sizes varied, depending on the individual types of connections.

In particular, using an appropriate cyclic testing protocol, the total energy absorption of the connections was determined on the basis of the hysteresis loops. Rather than looking at the maximum rotation or story drift capacity of the connections, focusing on the complete energy absorption distills the connection performance into the most important performance measures. This is what has been recommended by Nakashima, Suita, Morisako and Maruoka (1998) and Bjorhovde, Goland and Benac (2000). The procedure is now utilized in Japanese seismic performance assessment criteria.

The data have been assembled in connection performance tables, which can be useful for designers considering frames with PR connections. Other studies have shown that such frames offer potential advantages for seismic construction (Astaneh, Nader and Malik, 1989), although overall building drifts may be relatively high.

LOCAL STABILITY OF STRUCTURAL MEMBERS

Cross-Sectional Stability of Hot-Rolled Shapes: This is an ongoing study by Professor Benjamin Schafer at Johns Hopkins University in Baltimore, MD. It is performed as part of his responsibilities under the AISC Faculty Fellow program.

Cross-sectional stability or resistance to local buckling of many forms is an essential feature of analysis and design of cold-formed steel members. These types of elements have very high width-to-thickness ratios and various forms of edge support conditions, and local buckling checks are extensive and fairly complicated. The American Iron and Steel Institute (AISI) issues the *North American Specification for the Design of Cold-Formed Steel Structural Members* (AISI, 2007), and this standard and its predecessors give the authoritative criteria for all forms of local buckling.

Known primarily for his work on the strength and stability of cold-formed steel structures, Professor Schafer developed the direct strength method (DSM) for such elements, making the checks for local buckling significantly more robust and all-encompassing (Schafer, 2006). He is now working to provide a similar approach for slender (noncompact) hot-rolled members, which will take into account the post-buckling reserve strength. This appears to offer economies for the use of slender members, and also to provide designer-friendly criteria for highly complex problems. Finally, in addition to developing improved local buckling design criteria and methods for the AISC *Specification for Structural Steel Buildings* (AISC, 2005), he has also developed tutorials for DSM and how the method can be used for hot-rolled steel.

STEEL STRUCTURES UNDER FIRE CONDITIONS

Behavior and Strength of Steel Columns with Partial Damage of the Fire Retardant Coating: This project is a major effort of the Chinese National Natural Science Foundation, taking place at Tongji University in Shanghai, China. The director is Professor G.-Q. Li.

At this stage of the research work, two full-scale tests of wide-flange steel columns have been completed. Coated with 20-mm (¾-in.)-thick fireproofing material, the fireproofing was purposely removed from each end of the columns, to assess the performance of such damaged members under laboratory fire conditions. The 140-mm (4½-in.) deep H-shape column specimens were 2.7 m (9 ft) long; the fireproofing was removed from 190 mm (72 in.) of each end of one of the specimens, and from 380 mm (15 in.) from each end of the other specimen (see Figure 5). The columns had flush end-plates at the ends; they were loaded to 55% of their axial capacity while the temperature in the furnace was set to follow the criteria of the ISO 834 code. Figure 4 shows the test setup with the furnace; Figure 5 gives the dimensional data for the column specimens.

As expected, the tests showed that the fire resistance of the damaged columns was reduced, and the reduction was significantly larger for the member with the largest amount

of fireproofing removal. Further details of the tests are not yet available, but it is noted that the column failure was initiated by the local buckling that took place at the unprotected column ends. Examples are shown in Figure 6.

COMPOSITE CONSTRUCTION

Composite Beams with Precast Hollowcore Slabs: This research project is conducted at the University of Leeds in England, with Dr. Dennis Lam as the director.

The study was undertaken on the premise that the use of precast slabs could offer reduced construction time, cost of concrete materials, etc. The hollowcore slab also offers reduced weight and the advantage of readily available conduits for cables and similar.

At this time the research work focuses on the use of simple beam-to-column connections with the hollowcore slabs, and a number of tests and analyses have been carried out for the system. The correlation between finite element evaluations and the physical tests is good; detailed moment capacity and rotation characteristics are being assembled for eventual use toward the development of design criteria. Figure 7 shows an example of one of the finite element models.

PLATE GIRDER RESEARCH IN SPAIN

The steel structures research activities in Spain have expanded significantly over the past few years, for several reasons. The country is benefiting from an active economic climate, and a large number of companies in the national and international market are aggressively looking for novel applications

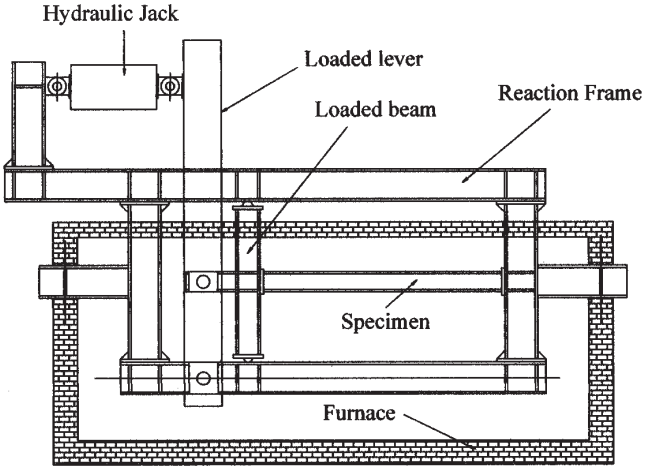

Fig. 4. Test setup for columns with damaged fireproofing (figure courtesy of G.-Q. Li).

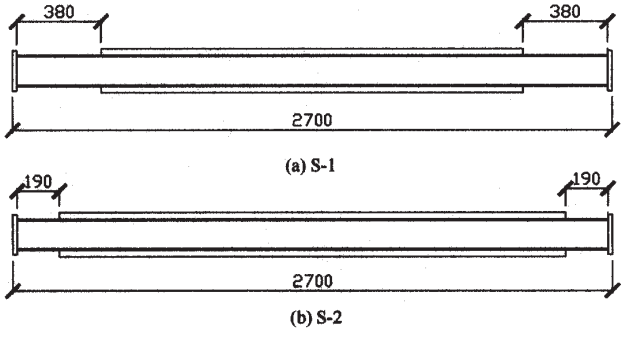

Fig. 5. Column specimens with damaged fireproofing (figure courtesy of G.-Q. Li).

(a) End A

(b) End B

Fig. 6. Local buckling within unprotected column ends (photo courtesy of G.-Q. Li).

of structural materials and systems. This applies to buildings as well as bridges, and is greatly assisted by prominent architects and engineers such as Calatrava and Moneo, and university researchers such as Professors Eduardo Bayo (University of Navarra) and Enrique Mirambell (Polytechnic University of Catalonia). The projects described in the following are but two examples of current research work.

Hybrid Steel Plate Girders: This research project is funded by the Spanish "National Agency," with Professor Mirambell as the director.

Based on the concept of more efficient use of materials of different strengths in the various elements of the cross section, hybrid girders have been studied in the U.S. and other countries with a view toward increased construction economies. Some of the problems of hybrid girders are those of the higher slenderness of high strength webs, for example, as well as the different limit states that may govern the ultimate strength of the tension flange. Fatigue is, of course, always a consideration for girders that are to be used in bridges and crane structures.

The current study at the Polytechnic University of Catalonia focuses on two main subject areas, namely, shear buckling and the response of the girder to concentrated loads. Based on extensive parametric evaluations, the results are now being translated into design requirements (Chacón, Mirambell and Real, 2006). It is clear that current approaches tend to be conservative for girders with stocky panels. Further, initial imperfections must be taken into account, and such is being done within the criteria that have been developed.

Design of Stainless Steel Plate Girders for Shear: Stainless steel offers certain aesthetic advantages for structural applications, although the use of such materials in construction is still very limited, primarily because of cost. Nevertheless, under some environmental and exposure conditions the use of stainless steel may be economically feasible. The plate girder project described here is being conducted at the Polytechnic University of Catalonia, with Professor Mirambell as the director. It is financially supported by the Spanish ministries of Education and Culture, and Science and Technology.

The primary aims of the project are (1) to communicate with engineers and architects and enhance the fundamental understanding of stainless steel properties and behavior, with special emphasis on the nonlinear response; (2) to detail the primary limit states of stainless girders, but especially those associated with shear response and stability; and (3) to develop an efficient and practical design approach for such girders subjected to shear.

Three experimental groups of tests have been done, and 27 girders have now been physically tested, with the first and second groups focusing on the general behavior while subjected to shear loading. The first group used girders with low-to-medium web slenderness; the second group had members with slender webs. The third group aimed at determining the effect of longitudinal stiffening of the girders. Finite element analysis has added to the fundamental understanding of the behavior of these girders, and the correlation between tests and theory is generally very good. Figure 8 compares the ABAQUS finite element model at shear buckling with the physical specimen—the data are very good. A new shear design procedure has now been developed, including the effects of transverse and longitudinal stiffeners, end posts, and actual boundary conditions (Estrada, Real and Mirambell, 2007a, 2007b).

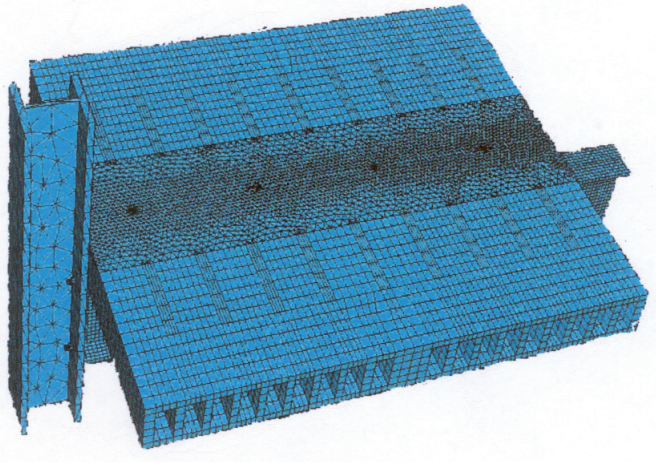

Fig. 7. Composite connection with hollowcore slab (figure courtesy of Dennis Lam).

ACKNOWLEDGMENTS

Special thanks are due the following members of the International Structural Steel Research Advisors (ISSRA) who provided input to this paper:

Eduardo Bayo, University of Navarra, Pamplona, Spain

S.-L. Chan, Hong Kong Polytechnic University, Hong Kong, China

Michael Gilmor, CISC, Toronto, Ontario, Canada

Jean-Pierre Jaspart, University of Liège, Liège, Belgium

G.-Q. Li, Tongji University, Shanghai, China

Additional assistance has been provided by Charles W. Roeder, University of Washington, Seattle, WA; Dennis Lam, University of Leeds, Leeds, England; Ali Abolmaali, University of Texas at Arlington, Arlington, TX; and Benjamin W. Schafer, Johns Hopkins University, Baltimore, MD.

REFERENCES

Abolmaali, A., Kukreti, A., Motahari, A. and Ghassemich, M. (2008), "Energy Dissipation Characteristics of Semi-Rigid Connections," in review for possible publication in the *Journal of Constructional Steel Research.*

AISC (2005), *Specification for Structural Steel Buildings,* American Institute of Steel Construction, Chicago, IL.

AISI (2007), *North American Specification for the Design of Cold-Formed Steel Structural Members*, American Iron and Steel Institute, Washington, DC.

Astaneh, A., Nader, M.N. and Malik, L. (1989), "Cyclic Behavior of Double Web Angle Connections," *Journal of Structural Engineering*, ASCE, Vol. 115, No. 5, May, pp. 1101–1118.

Bjorhovde, R., Goland, L.J. and Benac, D.J. (2000), "Performance of Steel in High-Demand Full-Scale Connection Tests," *Proceedings*, North American Steel Construction Conference, Las Vegas, NV.

Chacón, R., Mirambell, E. and Real, E. (2006), "Resistance of Transversely Stiffened Hybrid Steel Girders under Concentrated Loads," *Stability and Ductility of Steel Structures*, D. Camotim, N. Silvestre and P. B. Dinis, Editors, IST Press, Lisbon, Portugal.

Estrada, I., Real, E. and Mirambell, E. (2007a), "General Behaviour and Effect of Rigid and Non-Rigid End Posts in Stainless Steel Plate Girders Loaded in Shear. Part I: Experimental Study," *Journal of Constructional Steel Research*, Vol. 63, pp. 970–984.

Estrada, I., Real, E. and Mirambell, E. (2007b), "General Behaviour and Effect of Rigid and Non-Rigid End Posts in Stainless Steel Plate Girders Loaded in Shear. Part II: Extended Numerical Study and Design Proposal," *Journal of Constructional Steel Research*, Vol. 63, pp. 985–996.

Nakashima, M., Suita, K., Morisako, K. and Maruoka, Y. (1998), "Tests of Welded Beam-Column Assemblies. I: Global Behavior," *Journal of Structural Engineering*, ASCE, Vol. 124, No. 11, November, pp. 1236–1244.

Schafer, B.W. (2006), *Direct Strength Method (DSM) Design Guide*, Design Guide CF06-1, American Iron and Steel Institute, Washington, DC.

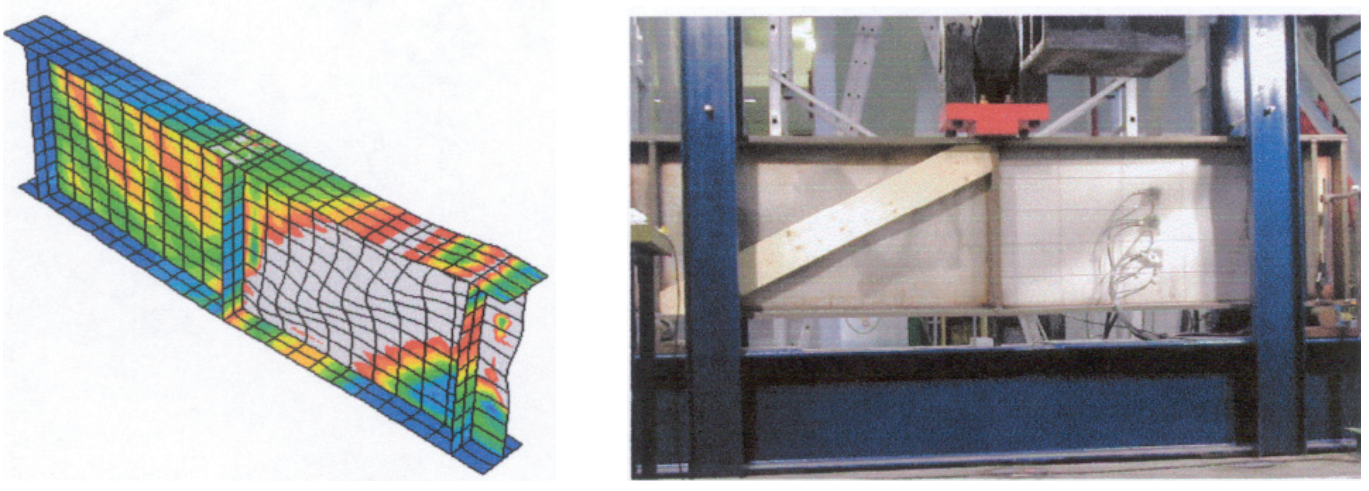

Fig. 8. Finite element model and test specimen of stainless steel plate girder (photos courtesy of E. Bayo and E. Mirambell).

Suggested Reading from Other Publishers

The following abstracts summarize papers published by others on the subject of steel design and construction that may be of interest to *Engineering Journal* readers.

From the March 2008 (Vol. 134, No. 3) issue of *Journal of Structural Engineering* published by the American Society of Civil Engineers:

Shear Diaphragm Bracing of Beams.
I: Stiffness and Strength Behavior
Todd A. Helwig and Joseph A. Yura

Light gage metal decking is commonly used in the building and bridge industries for concrete formwork. In addition to supporting the concrete, the metal forms also improve the lateral-torsional buckling capacity of the beam or girder they are fastened to as they behave as a shear diaphragm and restrain the warping deformation of the top flange. However, the stability bracing requirements for shear diaphragms are not well established. This is the first part of a two-part paper on diaphragm bracing of beams. The first part of the paper focuses on behavior whereas the second part focuses on general design requirements. The diaphragms in the study were connected along two edges to the top flanges of adjacent girders. The parameters that were investigated include the diaphragm stiffness, load type, and load position. The type of loading has a significant effect on the stability bracing behavior of the shear diaphragm. Other factors that have an effect on the bracing behavior include the web slenderness and the presence of intermediate discrete braces. The results presented in the first part of the paper create the foundation for a diaphragm bracing design methodology that is developed and presented in the second part of the paper.

Shear Diaphragm Bracing of Beams.
II: Design Requirements
Todd A. Helwig and Joseph A. Yura

Light gage metal decking is commonly used in the building and bridge industries for concrete formwork. In addition to supporting the wet concrete, the metal forms also improve the lateral-torsional buckling capacity of the beams or girders they are fastened to since they behave as a shear diaphragm and restrain the warping deformation of the top flange. The design requirements for shear diaphragm bracing are not well established. This is the second part of a two-part paper. The first part of the paper focused on the general stability bracing behavior for shear diaphragms connected to the top flanges of adjacent beams or girders. This part of the paper outlines the design requirements for shear diaphragm bracing and focuses on both the stiffness and strength requirements for beam stability. Design expressions are presented for the stiffness and strength requirements as well as a model that can be used to estimate the forces in the fasteners that connect the diaphragms to the top flanges of the beams. An example is presented at the end of the paper demonstrating the use of the design expressions.

Testing of Full-Scale, Two-Story Steel Plate Shear Wall with Reduced Beam Section Connections and Composite Floors
Bing Qu, Michel Bruneau, Chih-Han Lin and Keh-Chyuan Tsai

A two-phase experimental program was generated on a full-scale, two-story steel plate shear wall with reduced beam section connections and composite floors to experimentally address the replaceability of infill panels following an earthquake and the seismic behavior of the intermediate beam. In Phase I, the specimen was pseudodynamically tested, subjected to three ground motions of progressively decreasing intensity. The buckled panels were replaced by new panels prior to submitting the specimen to a subsequent pseudodynamic test and cyclic test to failure in Phase II. It is shown that the repaired specimen can survive and dissipate significant amounts of hysteretic energy in a subsequent earthquake without severe damage to the boundary frame or overall strength degradation. It is also found that the specimen had exceptional redundancy and exhibited stable force-displacement behavior up to the story drifts of 5.2% and 5.0% at the first and second story, respectively. Experimental results from pseudodynamic and cyclic tests are compared with seismic performance predictions obtained from a dual strip model using tension-only strips and from a monotonic pushover analysis using a three-dimensional finite-element model, respectively, and good agreement is observed.

Cast Steel Connectors for Circular Hollow Section Braces under Inelastic Cyclic Loading
Juan-Carlos de Oliveira, Jeffry A. Packer and Constantin Christupoulus

Although concentrically braced frames are an efficient means of providing lateral support in steel structures, many such frames designed to resist seismic loading and featuring hollow structural section braces have performed poorly in recent earthquakes—primarily due to unexpected connection failures. To address this issue, the use of a cast steel connector that fits between a tubular brace and a gusset plate is presented as an alternative to the reinforced, fabricated connections that are commonly used in seismic load resisting braced frames. The resulting connector was shaped using solid modeling software, verified by finite-element analysis, and finally cast to ASTM A958 standards. Laboratory results from static and cyclic testing of concentrically loaded brace-connector assemblies showed that the use of a cast steel connector is a viable means of connecting to tubular brace members for seismic (or even static) applications. Further, as the connector was crafted to fit a range of tubular members and can be mass produced, the proposed solution is an economical alternative to conventional tube-to-gusset connections under seismic loading.

From the May 2008 (Vol. 134, No. 5) issue of *Journal of Structural Engineering* published by the American Society of Civil Engineers:

Tubular Links for Eccentrically Braced Frames. I: Finite Element Parametric Study
Jeffrey W. Berman and Michel Bruneau

This paper describes the development and results of a finite element parametric study of eccentrically braced frame links having hollow rectangular cross sections (i.e., tubular links). The parametric study involves more than 200 combinations of geometries and properties and is divided into two parts. Part A considers a wide range of compactness ratios and link lengths to determine appropriate compactness ratio limits such that links with tubular cross sections can achieve desired rotation levels prior to significant strength degradation from local buckling. Part B of the study involves models developed with flange compactness ratios, web compactness ratios, and stiffener spacings near the proposed design limits from Part A, and also examines links having webs and flanges with different yield stresses (i.e., hybrid links). Results of the parametric study are also used to investigate the adequacy of a method for approximating link overstrength. A companion paper describes the experimental verification of the proposed design requirements.

Tubular Links for Eccentrically Braced Frames. II: Experimental Verification
Jeffrey W. Berman and Michel Bruneau

This paper describes the results of an experimental study to verify proposed design requirements for eccentrically braced frame links with hollow rectangular (i.e., tubular) cross sections. Twelve primary link specimens and two supplementary links that have different end connections are tested. Three cross sections and four normalized link lengths are considered. Two of the cross sections have web and flange compactness ratios near the proposed limits while the third cross section has compactness ratios significantly less than the proposed limits. Shear, intermediate, and flexural link lengths are tested, including some at the critical transition length from shear-to-intermediate link behavior. Results indicated that tubular links satisfying the proposed compactness and stiffener requirements can achieve the target plastic rotations for wide-flange links when subjected to the loading protocol specified in the 2005 AISC *Seismic Provisions*. The predominant failure mode is fracture of the link flange near the connection to the end plates used for testing. A method for calculating the ultimate link shear, proposed by others for wide-flange links, is also investigated and modified to agree with the results of the tubular link tests.

Behavior of Steel Beam-to-Column Joints at Elevated Temperature: Experimental Investigation
Z.H. Qian, K.H. Tan and I.W. Burgess

Although beam-to-column joints are a critical part of steel and composite framed structures, very few tests have been conducted under fire conditions. Of the tests conducted, only a limited range of joint types has been studied. The main reason for this is the high cost associated with elevated-temperature tests. This paper presents the results of an experimental investigation of typical steel extended end-plate beam-to-column joints at elevated temperatures. Six beam-to-column joints were tested. These included three tests conducted at 400, 550, and 700 °C, and another three tests on specimens at 700 °C with different axial compression forces applied to the beams to simulate restraint effects. Moment-rotation-temperature characteristics are summarized in order to investigate the degradation of this type of steel joint at elevated temperatures.

From the June 2008 (Vol. 134, No. 6) issue of *Journal of Structural Engineering* published by the American Society of Civil Engineers:

Analytical Performance Simulation of Special Concentrically Braced Frames
Jung-Han Yoo, Charles W. Roeder, and Dawn E. Lehman

The properties of special concentrically braced frames (SCBFs) enable them to be designed to meet performance-based seismic design (PBSD) criteria. SCBFs have large stiffness and strength to meet serviceability performance states. Life-safety and collapse-prevention PBSD limit states are controlled by inelastic postbuckling and tensile yield deformation of the brace. In SCBF construction, the braces are connected to the frame using gusset plates. Inelastic deformation of the brace places severe inelastic demands on gusset-plate connections. To improve the understanding and design of the seismic performance of SCBF connections, a coordinated analytical and experimental research study was undertaken. This paper describes the analytical component and includes a brief description of the experimental results, which were used in the development and validation of the model. The validated model was used to evaluate the inelastic performance of structural elements and to determine the frame ductility and concentration of plastic strains at potential locations of member or weld tearing or fracture. Detailed comparisons between experimental observations and computed results show that the analyses provided good correlation to actual behavior. The results were used to develop a methodology to predict tearing or cracking of key elements in the frame.

Improved Seismic Performance of Gusset Plate Connections
Dawn E. Lehman, Charles W. Roeder, David Herman, Shawn Johnson, and Brandon Kotulka

Current design practices use a strength-based design approach to design gusset plate connections in special concentrically braced frames (SCBFs), in which the expected tensile and compressive capacities of the brace are used to design the gusset plate and the weld used to connect the brace to the frame. To achieve brace end rotation, the gusset plate is sized using a linear offset rule, and large, uneconomical gusset plate connections may result. A research program was undertaken to improve the economy and performance of gusset plate connections. A new approach is proposed in which the gusset plate design is based on a balanced design approach in which the yield mechanisms of the brace are balanced with the yield mechanisms of the connection and the failure modes of the system to achieve a target yielding hierarchy and suppress unwanted failure modes. Full-scale one-story, one-bay frames were designed and tested to investigate the seismic performance of current and proposed design methods. In the test program, variations in balance factors between the brace, gusset plate, and weld were considered to study the proposed method, to evaluate possible yield mechanisms and failure modes, and to obtain the desired yielding hierarchy. Comparison of the observed and measured performance of each specimen is made and specific design expressions to improve the seismic engineering of SCBF systems are proposed.

GUIDE FOR AUTHORS

SCOPE: The ENGINEERING JOURNAL is dedicated to the improvement and advancement of steel construction. Its pages are open to all who wish to report on new developments or techniques in steel design, research, the design and/or construction of new projects, steel fabrication methods, or new products of significance to the uses of steel in construction. Only original papers should be submitted.

GENERAL: Papers intended for publication must be submitted by mail to the Editor, Cynthia J. Duncan, ENGINEERING JOURNAL, AMERICAN INSTITUTE OF STEEL CONSTRUCTION, One East Wacker Drive, Suite 700, Chicago, IL, 60601-1802.

The articles published in the *Engineering Journal* undergo peer review before publication for (1) originality of contribution; (2) technical value to the steel construction community; (3) proper credit to others working in the same area; (4) prior publication of the material; and (5) justification of the conclusion based on the report.

All papers within the scope outlined above will be reviewed by engineers selected from among AISC, industry, design firms, and universities. The standard review process includes outside review by an average of three reviewers, who are experts in their respective technical area, and volunteers in the program. The maximum number of papers sent to a single reviewer is three per year, with a frequency of not more than one per quarter. Papers not accepted will be returned to the author. Published papers become the property of the American Institute of Steel Construction, Inc. and are protected by appropriate copyrights. No proofs will be sent to authors. Each author receives three copies of the issue in which his contribution appears.

MANUSCRIPT PREPARATION: Manuscripts must be provided on PC-formatted media, such as a CD-ROM, in Microsoft Word format. A laser-quality proof must accompany your submittal. Fonts and spacing must be suitable for easy reading and reproduction (for the peer-review process). Do not embed photographs, diagrams, illustrations, charts or graphs within the electronic manuscript files. Only equations may be embedded within the flow of the text. Specific requirements for electronic graphics are outlined below. *Engineering Journal* reserves the right not to publish a submittal if suitable graphics cannot be provided by the author.

Title and By-Line: Exact name, title and affiliation of the author or authors are required to appear on the first page of the manuscript.

Body Text: Please restrict font usage to Times, Helvetica, Times New Roman, Arial, and Symbol (for Greek and mathematical characters.)

Headings: All headings should be typed flush left, using upper and lower case, with two line spaces above.

Tables: Each table should appear on its own page. Footnotes to tables should appear below the table, identified by superscripted lower case letters (a, b, c, etc.).

Equations: Whenever possible, equations should be set using Microsoft Equation Editor or MathType (www.mathtype.com). Please set equations using Times New Roman, Times, and/or Symbol fonts.

Captions: Captions should be typed, double-spaced, and located at the end of the electronic manuscript. All photos and graphics must be clearly marked to indicate their corresponding caption.

References: Should be noted clearly in the text and listed, double-spaced, on a separate page in the following sample format.

In text: (Doe, 1992)

In Reference List:

Doe, J.H. (1992), "Structural Steel," *Engineering Journal*, AISC, Vol. 100, No. 1, 1st Quarter, pp. 2–10.

Footnotes: Footnotes should be noted clearly in the text with a superscript asterisk, and should appear at the bottom of the text page, in the following style:

*For a detailed discussion, see...

Graphics (other than photographs): Provide a clear $8\frac{1}{2}$ in. × 11 in. laser-quality proof of each graphic element. Graphics should reproduce cleanly in black-and-white format. Graphics may be submitted and reproduced in color at the Editor's discretion. Please restrict font usage to Helvetica, Arial or Symbol, in sizes suitable for at least 50% reduction (12 pt. minimum). Line weights must be suitable for 50% reduction. When possible, provide each graphic element in a separate electronic file. TIF or EPS file formats are preferred, with a minimum resolution of 300 dots per inch.

Photographs: Provide either original photographs or high-quality electronic files and laser-quality proofs. Electronic photographs may be submitted as grayscale TIF or JPG images, one photograph per file. Photographs may be submitted and reproduced in color at the Editor's discretion. Minimum image resolution is 300 dots per inch. Photographs should be a minimum of 4 in. wide, so the minimum image width is 1200 pixels. Detailed photographs may require resolutions up to 1200 dots per inch. Photos embedded in word-processing documents are not acceptable.

There's always a solution in steel.

ENGINEERING JOURNAL
American Institute of Steel Construction
One East Wacker Drive, Suite 700
Chicago, IL 60601